ABSTRACT

Title of Dissertation:	THREE-DIMENSIONAL BIOPATTERNING TECHNOLOGY AND APPLICATION FOR ENZYME-BASED BIOELECTRONICS
	Sangwook Chu, Doctor of Philosophy, 2018
Dissertation directed by:	Professor Reza Ghodssi, Department of Electrical and Computer Engineering

Integration of biomaterials with 3-D micro/nano devices and systems offers exciting opportunities for developing miniature bioelectronics with enhanced performances and advanced modes of operation. However, the limited wetting property of such small scale 3-D structures (Cassie-Baxter wetting) presents a potential challenge in these developments considering most biological materials require storage in buffered aqueous solutions due to their inherently narrow stability window. In this thesis research, an electrowetting-assisted 3-D biomanufacturing technology has been developed enabling highly selective and programmable biomolecular assembly on 3-D device components. The successful integration of microscale 3-D device structures created via conventional microfabrication techniques with a nanoscale molecular assembly of Tobacco mosaic virus (TMV), enabled hierarchical and modular material

assembly approaches for creating highly functional and scalable enzyme-integrated microsystems components.

The potential limitation in 3-D bio-device integration associated with the surface wettability has been investigated by adapting Si-based micropillar arrays (μPAs) as model 3-D device structures, and a cysteine-modified TMV (TMV1cys), as the biomolecular assembler which can functionalize onto electrode surfaces via a self-assembly. The comparative studies using μPAs of varying pillar densities have provided clear experimental evidence that the surface coverage of TMV1cys self-assembly on the μPA is strongly correlated with structural density, indicating the structural hydrophobicity as a key limiting factor for 3-D bio-device integration.

The 3-D electro-bioprinting (3D-EBP) technology developed in this work leverages the hydrophobic surface wettability by adapting a capacitive wettability-control technique, known as electrowetting. The biological sample liquid was selectively introduced into the microcavities using a custom-integrated bioprinting system, allowing for patterning of the TMV1cys self-assembly on the μPA substrates without the limitations of the structural density. The functional integrity of the TMV1cys post 3D-EBP allowed conjugations of additional biological molecules within the 3-D substrates. Particularly in this work, immobilization of glucose oxidase (GOx) has been achieved via a hierarchical on-chip immobilization method incorporating 3D-EBP. Combined with the enhanced and scalable enzymatic reaction density on-chip and the electrochemical conversion strategies, the innovative 3D biomanufacturing technology opens up new possibilities for next-generation enzyme-based bioelectronics.

THREE-DIMENSIONAL BIOPATTERNING TECHNOLOGY AND APPLICATION FOR ENZYME-BASED BIOELECTRONICS

by

Sangwook Chu

Dissertation submitted to the Faculty of the Graduate School of the
University of Maryland, College Park, in partial fulfillment
of the requirements for the degree of
Doctor of Philosophy
2018

Advisory Committee:
Professor Reza Ghodssi, Chair
Professor Pamela Abshire
Professor James N. Culver
Professor Yu Chen
Professor Ryan D. Sochol

Dedication

This is dedicated to

my dear wife Hanna

my parents Hong and Myunghee

and my brother Sanghyun

for their unconditional love and support.

Acknowledgements

I would like to thank my advisor Professor Reza Ghodssi for his unremitting support, guidance, and encouragements throughout the course of this work. I also would like to thank my dissertation committee, Professor James N Culver, Professor Pamela Abshire, Professor Yu Chen, and Professor Ryan D. Sochol, for their constructive feedback and supports leading to the completion of this work.

Special thanks should be dedicated to my mentors and collaborators who were essential in completing the journey of my PhD research. Dr. Konstantinos Gerasopoulos for being the best unforgettable mentor guiding me at the early stage of my PhD research career. Dr. Faheng Zang for being a great senior colleague with many inspiring discussions and implementations. Professor James N. Culver for providing invaluable insights and guidance to the field of plant viruses and biochemistry. Mr. Adam D. Brown for being always prompt and supportive in helping me learn basic biology and prepare virus samples. Also, the staff members at the Maryland Nanocenter, Mr. Thomas Loughran, Mr. John Abraham, Mr. Jonathan Hummel, and Mr. Mark Lecates, for their professional supports for working in the FabLab for device fabrication and imaging.

Last but not least, huge thanks to all members of the MEMS Sensors and Actuators Laboratory for the genuine camaraderie developed through the exciting research discussions and critical feedback. And to the funding agencies, U.S. Department of Energy [Award Number: DESC00011600] and the U.S. Army Research Laboratory's Army Research Office [Award Number: W911NF1710137], for their generous support throughout the work.

Table of Contents

List of Tables

List of Figures

Chapter 1: Introduction

The convergence between biochemistry and micro/nano manufacturing technologies has brought today's revolutionary advancements in the development of miniaturized devices and systems equipped with biochemical functions from integrated biomaterials (e.g. nucleic acids, antibodies, viruses, etc.).[1–5] The extreme precision and high production yields, established through industrial production of integrated-circuits (IC) and micro-electro-mechanical systems (MEMS), are the primary attractive facets for many scientists and engineers seeking affordable, efficient, and reliable platforms to study and implement the unprecedented power of biotechnology for research and "real-life" applications (heath diagnostics, drug monitoring, environmental monitoring, nanoelectronics fabrication, etc.).

Among the range of bioelectronics under development, enzyme-integrated devices have received significant attentions due to their highly selective catalytic functions, participating in a range of metabolic, signaling, and energy transfer reactions.[6–10] The prime example of enzyme implementations in bioelectronics is the development of glucose sensors which have received wide public recognitions for their significant clinical role in helping diabetes patients.[10] Recent efforts in this area have largely focused on reducing the burden of patients from frequent blood draws. The progressive efforts have developed implantable or patch-type devices allowing continuous monitoring of blood glucose levels, and eliminating unfavorable finger pricks.[11,12] In addition, other approaches have shown the potential to derive blood glucose levels from other body-fluids (saliva, sweat, tears, etc.) as a non-invasive

monitoring solution.[13–15]

Enzymatic biofuel cells (EBCs) are another intriguing example of enzyme-based bioelectronics. EBCs have received increasing attentions from a broad spectrum of researchers due to their exciting potentials for sustainable energy harvesting from biofuels (e.g. glucose, ethanol, cholesterol, etc.), and further opportunities to autonomously operate implanted devices with fuel sourced from body fluids.[16] In the efforts to improve EBC's energy harvesting performance, researchers have focused on study and implementation of efficient electron transfer mechanisms from enzymes to electrodes, developing stable and high density immobilization strategies, synthesis of new cofactors and enzymes, and the use of enzyme cascade reactions for efficient consumption of biofuels. More recently, as EBC technology has made significant progress in performance to operate low power electronics (e.g. LEDs), there have been demonstrations of prototype developments for on-demand implantable or wearable device applications.[14,17] In addition to the major progresses in the enzyme-based bioelectronics, there is growing interest utilizing enzymatic cascade reactions for realizing biomimetic systems, synthesis of new materials, or even for creating bio-computing systems by programming the catalytic reaction ratios in the stream of reaction sequences.[8,9,18]

The essential elements needed for realizing advanced devices and systems is the ability to control enzyme immobilization density allowing for enhanced and scalable reactions on targeted substrate. The main objective of this research is to develop a highly scalable and controllable biomanufacturing technology by taking an

hierarchical material assembly approach utilizing a nanoscale biomolecular assembler with tunable microscale device components.

1.1. Background and Motivation

While there are different ways to contribute to the development of enzyme-based bioelectronics, the core motivation of this thesis research has been to develop biofabrication technologies to obtain scalable enzyme immobilization to allow enahaned and controlled biocatalytic reactions on chip for advanced enzyme-based bioelectronics and platforms. The general idea is to integrate three-dimensional (3-D) microdevice components with nanostructured biological receptors to create hierarchical receptor elements for enzyme immobilization. The advantages of the 3-D device component and nanostructured bionanoreceptors - Tobacco mosaic viruses (TMVs) and their virus-like-particles (TMV-VLPs) - utilized in this research will be briefly discussed below to emphasize the motivation of this work.

Three-Dimensional Transducers for Microsystem

Building upon the numerous techniques established for surface immobilization of biological molecules, many researchers have demonstrated integration of biological materials with three-dimensional transducers in an effort to achieve enhanced bioelectronics performance at a miniaturized system scale.[19–23] Three-dimensional structures at micro- and nano- scales offer a number of beneficial properties compared to their two-dimensional counterparts, allowing an extensive range of applications including micro energy storage/harvesting device,[24–26] micro/nano actuators,[27,28] micro thermal management devices,[29,30] water-repellent surfaces,[31,32] optical modulators,[33–35] 3D VLSIs,[36] etc. The primary attractive feature is the high physical interfaces between

system components and materials within the restricted areal budget, which can directly translate into large enhancements in performance. Moreover, the precise control over arrangement of the structures through microfabrication or emerging 3-D printing technologies further boosts the utility of three-dimensional components with increased surface-to-volume ratio, functional uniformity, scalability, and tunability.[37]

One of the interesting characteristics present in such small scale 3-D structures is their limited wetting property known as structural hydrophobicity.[32,38–40] When micro- or nano- scale structural components are densely arranged, the wetting of 3-D cavities with liquids is limited by surface tension at the solid-liquid, liquid-air, and solid-air interfaces (details will be discussed in Chapter 2). Considering most biological materials are stored in buffered aqueous solutions due to the narrow biological stability windows, the structural hydrophobicity can be a significant limiting factor when attempting to introduce biological materials into the 3-D cavities for device functionalization. Thus, it is crucial to characterize the effect of structural hydrophobicity on biofunctionalization. Also, identification of an enabling principle for complete and uniform immobilization over the 3-D device structure will have strong potential to direct invention of novel biofabrication processes and to have a significant impact on the performance of a wide range of bioelectronics.

Viruses and Virus-Like-Particles as High-Density Biological Receptors

Viruses are small infectious agents which naturally store and transport genes to the living host cells of other organisms. The pathogenicity of viruses depends on their interactions with the host, and they can be specified into three different categories by the type of host where they undergo pathogenic replication (plant viruses,

bacteriophages (bacterial viruses), animal viruses).[41] Hence, viruses are one of the major pathogenic agents which are detected and analyzed for the production of vaccines and drugs for prevention and treatment of the associated-diseases.

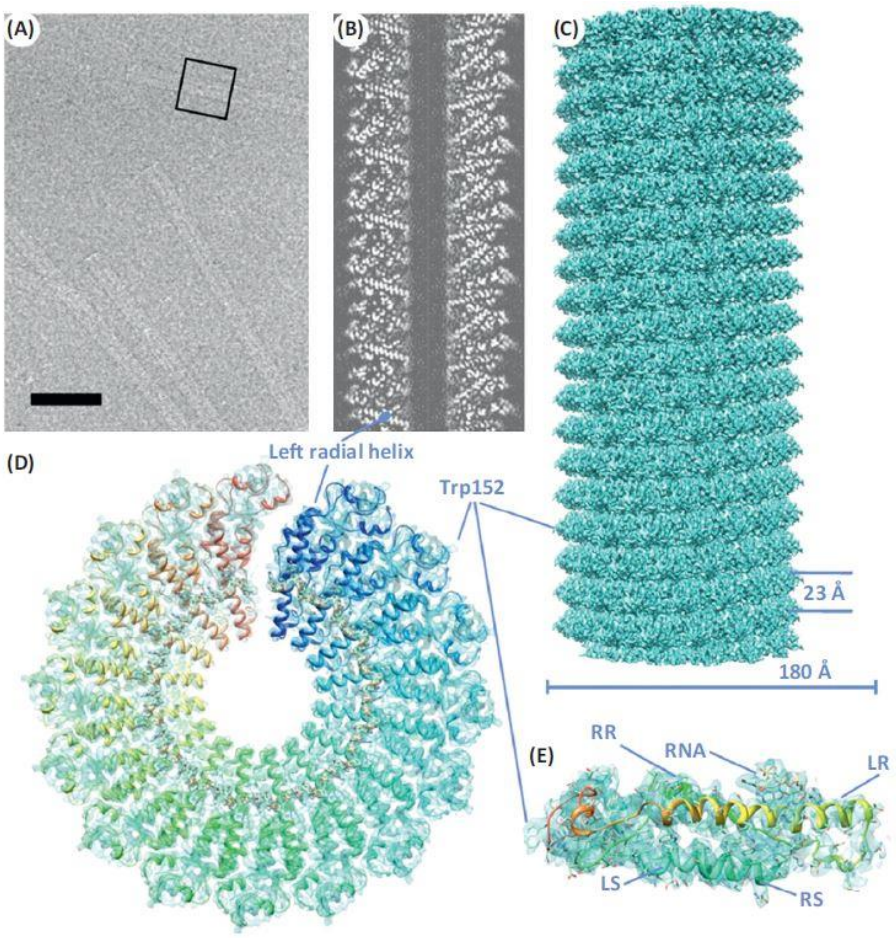

Figure 1-1. Structural features of TMV reconstructed using cryo-electron micrograph (EM). (a) a micrograph of TMV embedded in vitreous ice (scale bar: 60 nm). (b) Central slice from the final 3D reconstructed map. (c) Overview of the helical density map. (d) Single turn of 16 CPs with bound RNA. (e) Ribbon diagram of one CP and its three bound RNA bases superimposed with the cryo-EM density map. LR, RR, LS, RS: left radial, right radial, left slewed and right slewed α-helices, respectively.[42]

Over the past decade, advancements in genetic engineering and biosynthesis technologies have changed the point of view towards these "unfriendly" biological molecules directing many researchers to consider some type of viruses, that are proven to be non-infectious to humans (plant viruses and bacteriophages), as functional

nanomaterials which benefit from their self-assembled nanostructures, molecular storage functions, and high density residues arrayed along the coat protein (CP) surfaces.[41,43–45] Also, the profound understanding of the viral CP assembly mechanisms and the ability to produce identical CPs from genetically synthesized cells enabled the construction of gene-free viruses which recreate the original biological functions (structure, surface chemistries) of model viruses except for their replication/pathogenic capabilities − known as virus-like-particles (VLPs).[46–49] As a result, those efforts have successfully demonstrated the use of viruses as templates for the synthesis and assembly of nanomaterials,[41] as vehicles for targeted drug and gene delivery,[47,50–52] and as probes for sensing and imaging.[53–55]

Among the various types of viruses under development as "smart" materials for bio- and nano-technology applications, the derivatives of *Tobacco mosaic viruses* (TMVs) have received significant attention for creating highly functional micro/nano device components, largely due to their high-aspect-ratio geometry and densely arranged surface receptors (Figure 1-1). The physics of the TMV, such as its primary cylindrical structures, coat protein assembly mechanism around its RNA, and biochemical properties are understood into great depth,[56–58] and this is driving the momentum of recent knowledge-based exploitation towards development of TMV-integrated micro/nano devices.

In this work, genetically engineered TMV particles will be utilized as nanoscale templates for high-density immobilization of enzymes onto device surfaces. The exceptional binding properties with device substrates and ultra-high density of available chemical conjugation sites on the nanoscale surfaces offer an excellent

opportunity to create highly functional bioelectronics. Furthermore, integrating TMV-enzyme conjugates with microscale devices will allow the creation of robust TMV-enzyme "forests" directing extremely high reaction densities for high performance bio-integrated devices.

1.2. Thesis Contributions

1.2.1. Understanding the Limitations in Biomaterials Integration with Three-Dimensional Microstructures

For the success of this research, it is critical to understand the anticipated impact of the wetting property of the 3-D device substrates on biomaterial integration. Initial efforts thus have focused on finding the dependence of 3-D geometrical features on the surface functionalization of the genetically engineered TMV (TMV1cys). Comparative studies using Si-based micropillar arrays (μPAs) displaying different structural densities have revealed that the functionalization of TMV1cys on μPA surfaces displaying high density pillar arrangement is limited, particularly on the surfaces deep within the microcavities, failing to provide uniform surface functionality for reproducible device performance. Through a careful analysis of surface morphology and functionalization profile within the microcavities of different pillar densities, a limited wetting property present in such 3-D micro/nano structured surfaces has been identified as the key limiting factor for biomaterial integration with high surface area micro/nanodevices. The hierarchical material assembly approach for realizing high performance and scalable device performance, the electrodes assembled via combination of TMV1cys and the μPAs of lower pillar densities have been characterized in a NiO-based electrochemical charge storage system, demonstrating a

significant enhancement in both power and energy performances. This has expanded the versatility of TMV1cys as a high-surface-area nanotemplate for assembling a variety of energy storage materials and the combined results have indicated that an enabling method to overcome the limitation from the wetting property will allow biomaterial-based manufacturing methods for creating fully scalable micro/nano device components.

1.2.2. Novel Technology Integration for Achieving 3D Biofabrication

The fundamental understandings behind the limitation for the 3-D device-biomaterial integration, the surface wettability of the μPAs has been characterized using droplets of TMV1cys solution, and the results combined with the theoretical derivation based on the *Cassie-Baxter* equation indicated that wetting property is a controllable factor by the μPA geometries. An innovative 3-D biofabrication technology, 3D electro-bioprinting (3D-EBP), uses electrowetting principle to address this limitation. 3D-EBP leverages the limited wetting property of the μPA for selective injection and patterning of the TMV1cys into the microcavities, allowing for uniform functionalization of the biological molecules on 3-D surfaces. The characterizations of the structural and chemical features of TMV1cys post 3D-EBP strongly confirm that this biofabrication technique is compatible with the biomacromolecule with no significant loss of functional integrity. The proof-of-concept demonstrations of an automated and programmable 3D-EBP process via a simple system integration with a commercial bioprinter further emphasizes the significance of the technology generating excellent opportunities for advancing on-demand 3-D bio-integrated devices and systems.

1.2.3. Demonstration of Scalable Micro/Nano/Bio-Integrated Materials for Bio-Sensing and Energy Harvesting

The ability to manufacture scalable 3-D biointegrated device components has been demonstrated via enzyme-based bioelectronics system. Initial efforts have developed an on-chip bioconjugation strategy for immobilizing glucose oxidase (GOx) onto the biological scaffold, TMV1cys. Relying on the robust self-assembly of TMV1cys on metal surfaces (e.g. Au), the on-chip chemical bioconjugation method has allowed for a high-density immobilization of GOx on TMV1cys via a heterobifunctional crosslinker (CL). The 3D-EBP has been successfully applied to perform the bioconjugation process on μPA electrodes towards demonstration of scalable enzymatic activities on chip. The close correspondence of the enzymatic activities (measured via colorimetric assays) with the surface area enhancement factors (derived based on the μPA geometry) strongly supports the successful incorporation of the developed biofabrication technology enabling high controllability over the biocatalytic activity on chip. Electrochemical characterizations demonstrated both biosensing and bioenergy harvesting capabilities with the TMV-assembled GOx electrodes. Particularly, a significantly higher redox current density was achieved compared to a recently published work, which strongly implies that the on-chip bioconjugation strategy was efficient for high density enzyme immobilization via TMV1cys. Combined with the enhanced and scalable enzymatic activity on chip with incorporation of the 3D-EBP, the developed methods provide a robust and readily employable strategy for advancing the scope of enzyme-based bioelectronics and platforms.

1.3. Literature Review

In this section, previous research and development associated with the theme of this thesis research will be reviewed.

1.3.1. Advances in Biofabrication Technologies

The core motivation behind the advances in biofabrication technologies is the desire to achieve controllability and scalability over the construction of interfaces between biorecognition elements and microelectronics/MEMS devices.[4] These efforts have been focused on determining effective tools for robust immobilization and definitive patterning of the biomaterials on the device surfaces. The strategies developed for the immobilization can be specified into three categories – physisorption, chemisorption, and bioaffinity interactions – as described in Figure 1-2.[59]

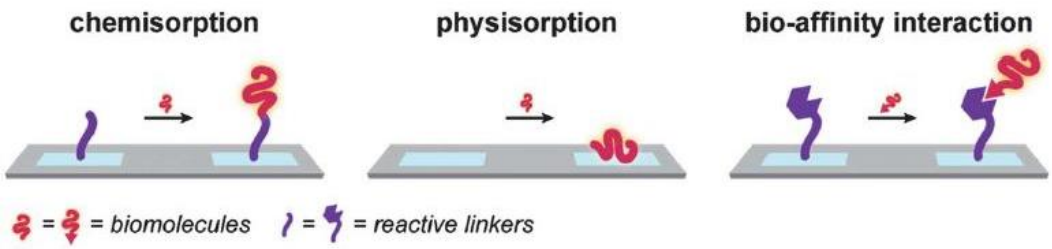

Figure 1-2. Schematics of biomolecule immobilization strategies [59].

Physisorption-based immobilization is a more primitive and simplistic method which utilizes direct loading of biological materials onto devices via physical interactions such as electrostatic, van der Waals, or entropically favorable interaction forces between the biorecognition elements and the solid surfaces. These approaches were favored in early generations of bio-integrated device research where the major objective relied on understanding the morphology and biological activities of

biorecognition elements when immobilized/attached onto microelectronics' material surfaces (e.g. silicon, silicon dioxide, glass, and metals).[60,61] As biofabrication techniques advanced, chemisorption-based methods were developed as a more stable means for immobilization utilizing covalent bonding as a bridging mechanism at the bio/device interface. One of the most impactful findings in chemisorption-based immobilization technology was the self-assembly of bifunctional crosslinker molecules containing silane or thiol onto silica or metal surfaces.[62,63] For example, crosslinkers terminated with silane or thiol groups at one side of their functional ends would form covalent bonds with glass or gold substrates, respectively (Figure 1-3). The crosslinker molecules form a densely packed monolayers on their respective substrates – widely known as a self-assembled monolayer (SAM) – providing a more sound means of immobilization compared to physisorption-based approaches, with enhanced uniformity and robustness. The other end of the crosslinkers have a variable pendant group which functions either as a biorecognition element itself, or as a means for binding proteins of interest, linking functional biomaterials with solid surfaces. For the latter case, high-affinity complementary components (e.g. lectin-glycoproteins, avidin-biotin, protein A/G-IgG antibodies, and DNA hybridizations) or covalent binding motifs available from amino acid functional groups (e.g. amine, carboxyl, hydroxyl, cysteine, etc.) have been widely utilized owing to their strong and selective linkage.[59,64–66] These synthesized or natural molecular linking mechanisms have provided useful resources for determining proper synthesis strategies for equipping a variety of biomaterials with device interfacing capability.

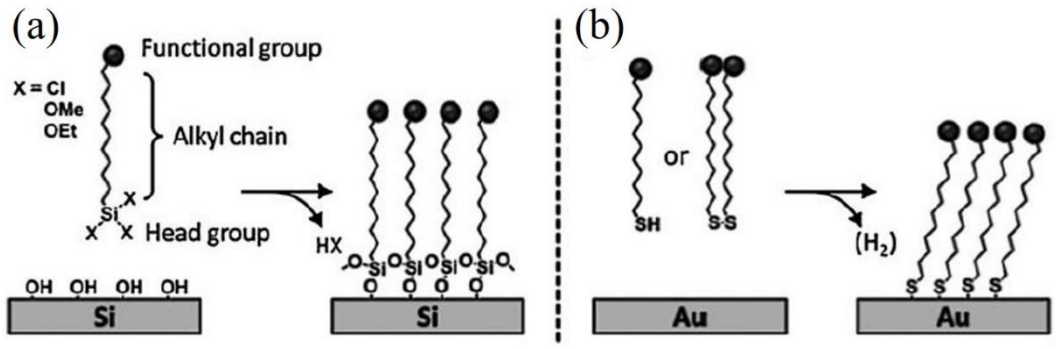

Figure 1-3. Formation of functional (a) silane/SiO_2 and (b) thiol/Au self-assembled monolayers.[67]

Beyond the large pool of immobilization techniques, advancements in biofabrication technology have focused on developing processes for pattering of biomaterials on solid surfaces to enable enhanced production yield, uniformity, scalability, efficient use of valuable biological materials, and high-throughput bio/chemical analysis.[68,69]

Various approaches have been introduced over the past twenty-five years, and Table 1-1 summarizes some of the major enabling technologies allowing remarkable advancements in the fabrication of bio-integrated devices. Before reviewing some of the representative works below, it needs to be emphasized that the major focus of the advancements in these technologies was to achieve high resolution patterning capability for creation of densely packed bio-arrays towards high-throughput biochemical analysis. Attributed to the main focus, none of the previous works have demonstrated patterning biomolecules on three-dimensional device substrates (e.g. 3D Bio-printing mainly have focused on for construction of 3-D cellular matrix for artificial tissues or organ regenerations, and thus not much of efforts was driven towards integration of biomaterials with 3D electronics[70,71]).

Table 1-1. Summary of nano- and micro-scale biofabrication/patterning processes.

Reference	Biofabrication Technologies	Enabling Mother Technologies	Minimum Feature Size	Dimensionality
[72–74]	UV lithographic biopatterning	- UV lithography - E-beam lithography - Focus-ion beam - Lift-off patterning	~ 1 um	2-D
[75,76]	E-beam lithographic biopatterning		~ 10 nm	
[77]	Focused-ion beam lithographic biopatterning		~ 80 nm	
[78,79]	Nanoimprint lithographic biopatterning		~ 75 nm	
[80,81]	Micro-contact printing	- Soft-lithography	~ 150 nm	
[82,83]	Nano-contact printing	- E-beam lithography	~40 nm	
[3,84]	Dip-pen nanolithography	- Atomic force microscopy, - Scanning probe microscopy	~25 nm	
[85,86]	Nanoshaving		~15 nm	
[87,88]	Nanografting		~100 nm	
[70,71]	3D/4D bioprinting	- Inkjet printing - Stereo-lithography - Computer-aided-designs (CAD)	~10 μm	3-D

Initial efforts included the use of conventional MEMS patterning technologies – photolithography or E-beam lithography – to either directly or in-directly pattern biomaterials on device substrates. These lithography-based technologies have the primary advantage of seamless integration with standard microfabrication processes. Also, the wide resolution range from the nanometer to micrometer regimes – which are fundamentally determined by the working wavelength range – is very attractive for the wide range of potential biochip applications. However, some of the harsh environmental conditions and chemicals (e.g. high vacuum, bio-incompatible photoresists, etchants, sterilizing optical range, etc.) required in the lithography-based processes narrow the range of potential biomaterials and applications. Moving forward,

the development of biofabrication technologies have avoided process operation within such harsh environmental conditions and thus prefer room temperature, non-dry/wet environment, etc.

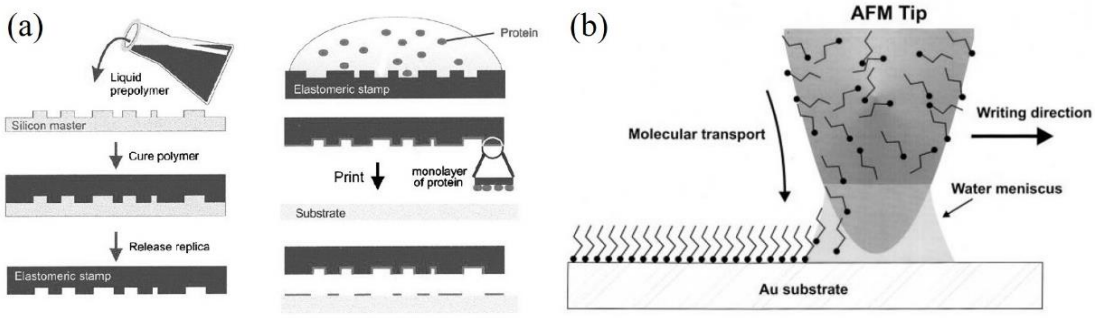

Figure 1-4. Schematic of (a) micro-contact printing[80] and (b) dip-pen nanolithography processes.[84]

In 1993, Kumar et al. first introduced a "bio-friendly" and widely applicable method enabling micro patterning of protein immobilization sites by combining soft-lithography (structuring polydimethylsiloxane (PDMS) via simple molding process) and SAMs.[89] This technology have benchmarked the scheme of traditional ink stamps (Figure 1-4a). In their very first work, one of the SAM molecules, alkanethiols, were first located on the surface of PDMS gratings through wet and dry processes and simply were stamped onto gold surfaces for the formation of patterned SAMs through a thiol-gold binding mechanism. This technology was named "Micro-Contact Printing (μCP)". Due to the extreme simplicity and high reproducibility the technology has been widely applied for patterning various types of biological materials from proteins to cells on solid surfaces by pre-patterning SAMs with different functional groups.[80,90–93] Compared to lithographical patterning approaches, the μCP has significant advantages for many researchers and industries because the process is low-cost, has no diffraction-

based limitations, and has minimal components which may degrade biological integrity. The process resolution remains in the sub 100 nm range due to the low elastic modulus of PDMS (mechanical weakness) and low molecular weight of SAM molecules (diffusion limited).[83] Potential improvements in the process resolution have been demonstrated in recent reports.[94]

In efforts to further shrink down the minimum feature sizes and minimize the potential loss of biological function during physical contact, atomic force microscopy (AFM) has been demonstrated as an effective fabrication tool for nanoscale patterning of biological molecules (Figure 1-4b).[68] Traditionally, AFM has been widely employed for nanoscopic characterization of biological molecules on solid surfaces due to its operational compatibility within bio-friendly environmental conditions (atmospheric pressure, measurement in wet conditions, etc.). Aside from their use for nanoscale topographical imaging, the high resolution probing/scanning capability was very attractive for many researchers leading to the emergence of many different AFM-based methods – Scanning Probe Lithography – to write nanoscale patterns of biomolecules (e.g. nanografting,[87] nanoshaving,[85] dip-pen lithography[3]).

A prominent example of scanning probe lithography methods, dip-pen nanolithography (DPN) was developed by Mirkin and co-workers.[3,84] The technique utilizes a water meniscus as a bridge between the "inked" AFM tip and the solid substrate to transport and deposit molecules at precisely defined locations. This process has been shown to be benign to biomolecules. While there is wide flexibility in the diversity of "inks" and substrates that can be used with this technique, and despite its high fidelity, achieving sub-50 nm patterns, DPN suffers from slow write speeds and

the need for careful control over humidity.[59] However, recent advancements in parallel tip arrays and polymer pen lithography are improving the speed to generate patterns.[95,96]

In summary, biofabrication technologies have rapidly evolved over the past two decades based on biochemistry principles, processing methodologies learned from the micro/nano fabrication industry, and instrumental science/engineering. The diversity of biofabrication technologies have led to greater understanding of biomolecular activities through on-chip characterizations, and is enabling rapid advancement of the high-density, multiplexed bioarrays necessary for biosensing and diagnostic applications.

1.3.2. TMV for Nanomaterial Synthesis and Device Fabrication

As briefly discussed in the motivation section, TMVs and their virus-like-particle derivatives (TMV-VLPs) have received significant attention for the development of bioelectronics due to the aforementioned beneficial characteristics (e.g. multivalent and high density receptors, high structural stability, nanoscale high surface area structures) compared to other types of biological molecules (antibodies, enzymes, DNA, etc.). In this section, recent developments utilizing TMV particles for microelectronics, energy storage devices, and biochemical sensing applications will be reviewed.

TMV as structural template for nanoscale inorganic material synthesis

Fabrication of nanostructured semiconductors, metals, and polymers have been one of the main-stream efforts across disciplines due to the unique properties which are

beneficial for a wide range of applications including energy storage, biochemical sensing, thermal management, hydrophobic surface coatings, etc.[32,97–99] In particular, the high surface-to-area feature is an essential property for the development of advanced miniature devices. Some of the most common processes used involve vapor-liquid-solid reactions through the combination of catalytic particles on a substrate and chemical vapor deposition or epitaxial methods.[100–103] Other less expensive techniques such as hydrothermal synthesis,[104] thermal evaporation,[105] sol–gel processes,[106] and electrodeposition[107] have also been reported. Although all of these techniques have demonstrated significant progress in the field, they often have to balance control over structural properties, variability of yield, and alignment of structures with cost of synthesis, equipment performance, and process compatibility with remaining processing steps. The advancement in biotechnology allowing modification of biological molecules through genetic engineering and chemical conjugation have offered an alternative tool for synthesis of nanomaterials; using nature-derived self-assembling biomolecules as a template for nanoscale materials and devices.[108] In this regard, the high-aspect-ratio cylindrical geometry and hollow 3-D structures of TMVs (length: 300nm, inner diameter: 4 nm, outer diameter 18 nm) offer a unique structural template for creating advanced bio-integrated materials and devices.

Early efforts include the formation of bioinorganic nanotubular composites/nanowires consisting of a TMV central core and external coatings of silica, iron oxides, or lead and cadmium sulfides.[109] These work involved mineralization of wild-type TMVs suspended in buffer solutions with heavy metal composites or silica nanoparticles (Figure 1-6a,b). The work reported in 1999 by Mann and co-workers

achieved the formation of CdS, Pd, SiO_2, and Fe_2O_3 by introducing the appropriate precursors into buffer solutions with suspended TMVs conditioned at mineralization pH. The exceptional stability of TMV was crucial for the demonstration of nanowires with different materials. For heavy metal composites (CdS, Pd, and Fe_2O_3) the specific metal-ion binding properties of the exposed surface amino acids (glutamate and aspartate surface groups) of TMVs are counted on for the formation of surface composite materials. The formation of silica composites on TMV surfaces is largely attributed to electrostatic interactions during TEOS based sol-gel reactions. The anionic silicate species formed by hydrolysis of TEOS experience strong interactions with positively charged TMV surfaces (large number of arginine and lysine surface groups) at acidic pH (pH 2.5) and induce silica nanowire formation from the TMV particle template.

In 2003, Kern and co-workers introduced use of the electroless metallization, one of the heavily used standard metal coating processes in the IC industry.[110] The process is a solution based process which works at environmental condition (room temperature, atmospheric pressure) and neutral pH. It is a two-step process; surface activation with Pd or Pt ions followed by surface metallization with Ni, Co, etc. In their work, they have genetically modified the outer-surface exposed amino acids of the TMV coat proteins (replaced Ser-155 with Gly-155) to reduce affinity towards metal ions, and was able to demonstrate spatially selective formation of metal wires only inside the inner channel of the TMV structure forming ~3 nm nanowire with maximum length of 600 nm (Figure 1-6c,d). The longer length of the metal nanowire (without gap) compared to a single TMV rod implied that the TMVs aggregate linearly with an

uninterrupted central channel. The very exciting point of this work is that the conductive nanowires can be built surrounded by proteins and the shape of the inorganic materials can be controlled via genetic modification. These provide unique tools and opportunities for the development of nanoscale bio-integrated devices.

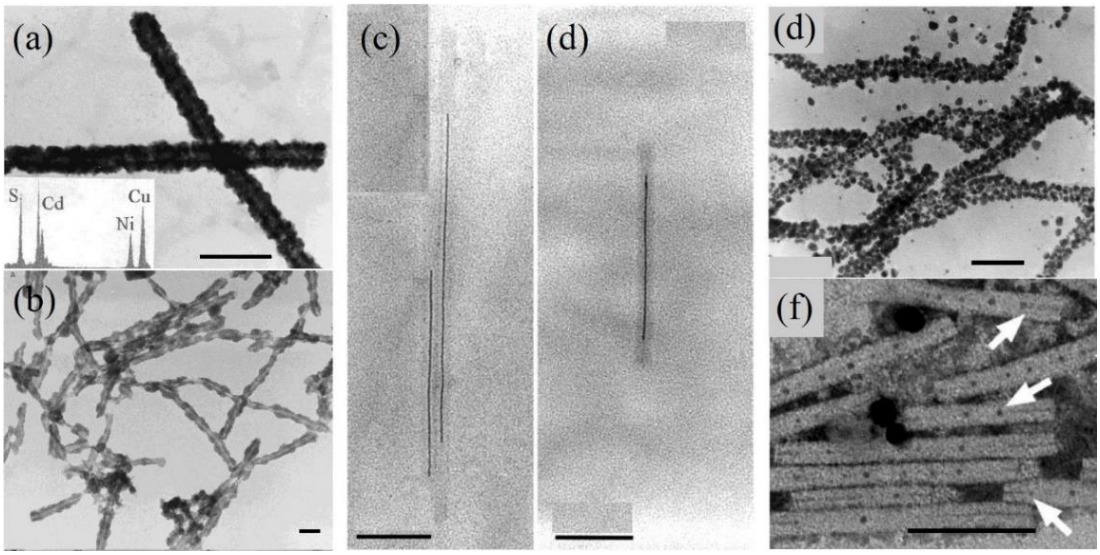

Figure 1-5. TEM micrographs showing inorganic nanomaterials synthesized using TMV as nanotemplate (scale bars: 100nm for all figures). (a) CdS and (b) Fe_2O_3-mineralized around outer surface of TMV particles (Ni and Cu EDX spectrum in (a) is from TEM grid and specimen holder, respectively).[109] (c,d) Spatially selective deposition through genetic modification allowed nanowire ~3-nm nanowire formation (c: Ni, d: Co) within the inner channel of TMVs using electroless metallization.[110] (d) Au and Ag (f) nano-composite materials were formed through chemical or photochemical reduction methods (the arrows in f indicates discretely arranged Ag nanoparticles within the central channel of TMV via photochemical reduction method).[111]

At a similar time point, Mann and co-workers have introduced the use of chemical or photochemical reduction methods for controlled deposition and organization of Pt, Au, or Ag nanoparticles.[111] Chemical reduction of Pt or Au containing precursors at acidic pH allowed the specific decoration of the external surface of wild-type TMV rods with metallic nanoparticles less than 10 nm in size (Figure 1-6c). Photochemical reduction of Ag precursors at pH7 resulted in nucleation and constrained growth of discrete Ag nanoparticles aligned within the 4 nm-wide inner

channel. They also have used mutant TMVs to confirm the effect of amino acid chains on the nucleation of metal ions, and concluded that the glutamic and aspartate acid groups (anionic charges) were involved in site-specific deposition of Ag nanoparticles at the inner channel.

A significant advancement towards reliable integration of TMVs with microdevices was reported by Harris and his co-workers who enhanced the metal binding properties of TMVs by genetically inserting cysteine groups at the N-terminus of TMV coat proteins.[112] The thiol functional groups in cysteine have high metal binding properties.[113] In particular, the covalent bonding available between thiol and gold provides a strong mechanism for immobilization of the highly functional nanoreceptors onto device surfaces. With the surface exposed cysteines, Au, Ag, and Pd clusters were synthesized around the TMV scaffold with enhanced density and versatility compared to wild-type TMVs.

Using the cysteine-modified TMV (TMV1cys), the first demonstration of using TMV within a functional device component was demonstrated by Culver and coworkers.[114,115] Introduction of TMV1cys onto Au-coated silicon substrates created self-assembled TMV layers on solid surfaces. The self-assembly process followed by electroless metallization (Pd activation + Ni or Co metallization) created densely arranged conductive nanoarrays displaying high surface area from the high-aspect-ratio TMV structure (Figure 1-7). In this work, a uniform coating of metal on TMV surface was demonstrated for the first time compared to the particularized metal clusters shown in previous works. Also, the concentration of TMV solution versus the density of final metallized TMVs were characterized, finding > ~0.1 mg/ml as an ideal concentration

range for efficient distribution of TMV samples for each TMV-based device fabrications. Also, they have demonstrated Ni-coated TMV particles as potential high performance electrodes for a NiO-Zn alkaline battery system. The TMV-templated Ni electrodes (TMV/Ni) resulted in a ~ 10-fold increase in energy density compared to planar Ni electrodes, confirming the applicability of TMV-templates for practical device applications. The creation of robust conductive nanomaterials directed further integration of the TMV/Ni into advanced microfabrication processes for creation of advanced functional components.

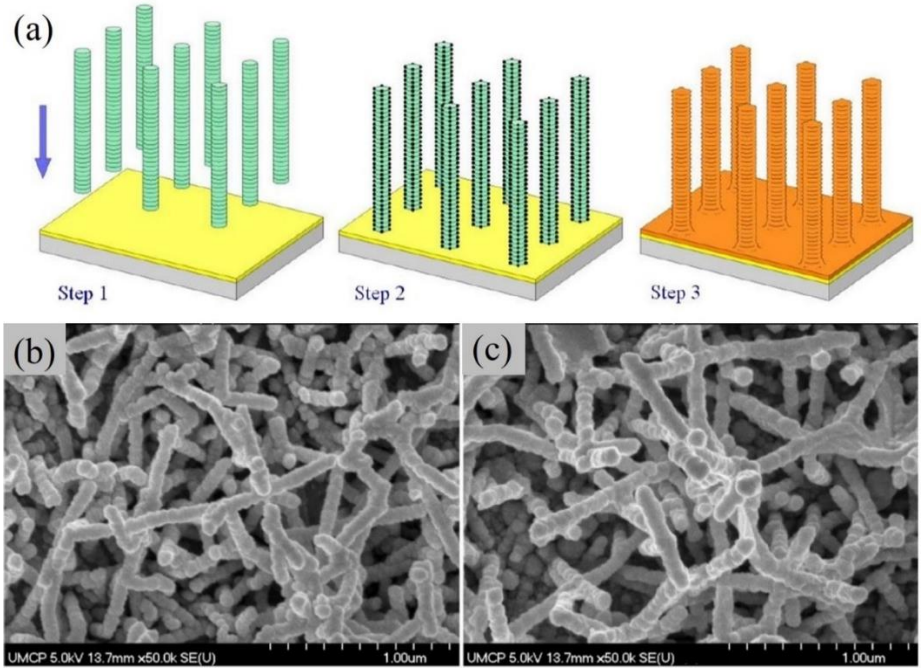

Figure 1-6. (a) Schematic representation of TMV1cys surface assembly and electroless metallization process; the TMV1cys binds onto the Au surface (step 1), it is activated with Pd catalyst (step 2) and finally for uniform nanostructured metal via electroless metallization (step 3). Scanning electron micrographs of (b) Ni- and (c) Co- coated TMV1cys on Au substrates confirm formation of nanostructured conductive materials. [114,116]

A prominent application is the use of TMV/Ni as a nanostructured current collector for the advancement of on-demand energy storage devices including Li-ion batteries and supercapacitors.[24,117–119] Process integration with thin-film deposition

technologies such as atomic layer deposition, physical vapor deposition (sputtering), and electrodeposition allowed various types of electrochemical charge storage materials (Si, RuO_2, TiO_2, V_2O_5, Sn) to be uniformly deposited over the TMV/Ni nanostructured element resulting in the definitive arrangement of charge storage elements at nanometer scale. Figure 1-8a shows an example of ALD V_2O_5 electrodes prepared on TMV/Ni template for Li-ion battery application. The core (conductive)/shell (electrochemically active) arrangement, as shown in (Figure 1-8b), is known as one of the most efficient arrangement for achieving effective use of the electrode active materials towards high gravimetric energy densities.[120,121]

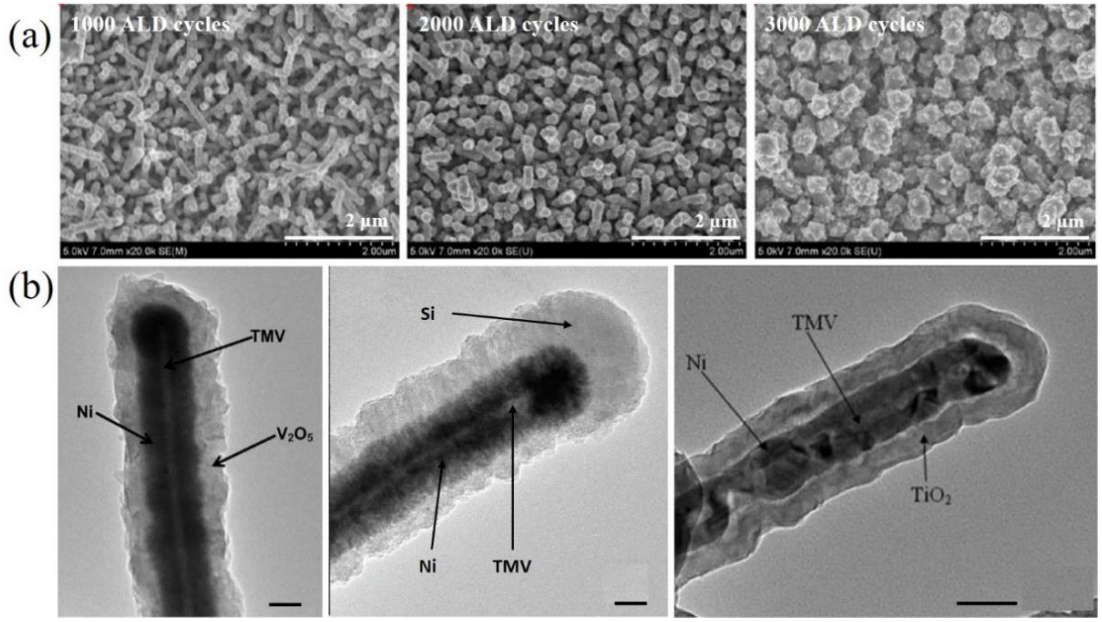

Figure 1-7. Electron micrographs of TMV-templated energy storage electrodes (scale bars: 50 nm unless specified). (a) The series of scanning electron microscopy images shows change in nanostructural morphology (porosity, roughness) in different cycles of V_2O_5 ALD.[24] (b) Process integration with thin-film deposition technologies, various types of core/shell structured charge storage electrodes have been demonstrated (left: TMV/Ni/V2O5,[24] center: TMV/Ni/Si,[121] right: TMV/Ni/TiO_2,[117] scale bars: 50 nm).

Additional applications of TMV templates for advanced micro/nano devices include the fabrication of digital memory devices,[122–124] vapor chemical sensors,[125]

conductive anti-reflective surfaces,[126] etc. Yang and co-workers have reported the use of a TMV-Pt composite as conductance-switching material towards the development of electronic bio-memory devices.[123] In their work, TMV-Pt composites were mixed with a polymer binding material (polyvinyl alcohol) and sandwiched between two Al electrodes. The TMV-based memory device was able to demonstrate write (2.5 V pulse), erase (-1.5 V pulse), and read (0.6 V pulse) functions by switching the conductance of the TMV-Pt composites up to 400 cycles. The first utilization of TMV scaffolds for sensors was reported by Wang and co-workers.[125] TMVs were used as a template for creating thin films of oligoaniline (OANI), a small molecule precursor of its parent polymer polyaniline (PANI); a conductive polymer effective for sensing volatile organic compounds (VOC). TMVs were found useful for arranging the small molecules onto the sensor surface; the change in conductance of the film was monitored when VOC was introduced into the custom designed sensing chamber.

In summary, the versatility of TMV's biological structure along with genetic modification technologies have been very useful for synthesis of a wide range of nanostructured materials in the progress of a wide range of micro/nano device developments. TMV is readily available at low-cost and its "non-infectious-to-mammals" property [127,128] direct great potential roles of TMVs as nanostructrual elements for the construction of nanoelectronics and bio-hybrid devices.

TMV and TMV-VLPs as highly functional biorecognition elements

Very recently, TMV's (or TMV-VLP's) ultrahigh density arrangement of surface receptors have received noticeable attention for utilization as recognition elements for development of bio/chemical sensors.[52,129–131] As introduced in Figure 1-

1, wild-type TMV displays a cylindrical high-aspect-ratio (16.7:1) structure - 300 nm in length, 18 nm in diameter, and 4 nm in inner channel width. The high surface area nanostructure is created by ~2130 identical coat proteins assembling around a single RNA strand, and the dense arrangement of CPs translates into a 2.3 nm pitch between the neighboring CPs.[56,57] The physicochemical properties and stability of the TMV is another intriguing and crucially important aspect for its practical use. Previous studies have verified the wide stability window in various "harsh" environmental conditions (temperatures up to 90 ºC, pH range: 2-8, various polar solvents) for TMV's biological functionality.[56,132] In addition, the well-established surface immobilization mechanism and the large pool of genetic modification[45] or chemical conjugation[133] routes offer exciting opportunities to apply TMV-derivatives as universal biorecognition elements or immobilization templates for creating high-performance biochemical sensors.

One of the very first works utilizing TMV-derivatives as recognition element in sensors was reported by our group in 2014.[130] In our work, a novel electrochemical sensing mechanism was introduced for the detection of small molecules. Specifically, TMV-VLP particles genetically-modified with specific peptides targeting a chemical explosive, trinitrotoluene (TNT), was used as a high-density binding agent in solution. Binding of TNT molecules to the body of the significantly larger TMV-VLPs modulated the diffusion coefficient of TNT molecules in electrochemical reaction (Figure 1-8). The concentration of TNT molecules was detected by measurement of differential current (TNT sample measurement - control sample measurement) which was reflected in reduction in electrochemical current measurement. While the sensing was not demonstrated in air - critical for detection of explosives - the work has

introduced interesting electrochemical sensing modality and demonstrated the excellent functionality (selectivity, and high receptor density, label-free sensing) of TMV-VLP as chemical recognition element.

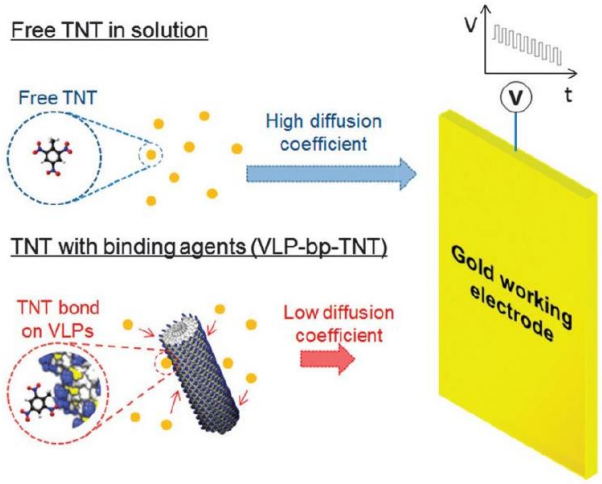

Figure 1-8. Schematic representation of electrochemical TNT sensing using TMV-VLPs binding agents modulating diffusion coefficient of the analyte.[130]

More recently, our group also have demonstrated the use of TMVs for biosensing applications.[129,134] In the recent reports, TMV-VLP genetically modified to express FLAG-tag (VLP-FLAG), a synthetic epitope tag, on its surface allowed the demonstration of immuno-sensing using anti-FLAG-antibodies as target analytes. While the C-terminus of the coat protein was modified with the target selective peptide, the N-terminus of the protein was equipped with cysteine residues allowing robust immobilization on device surfaces (N- and C-terminus of VLP CPs are exposed to the outer surface, Figure 1-9a). The immuno-sensing capability of VLP-FLAG has been demonstrated using two different transducers; an optical-ring resonator-based refractive index sensing[134] and inter-digitated electrode based electrochemical impedance sensing platforms[129] (Figure 1-9b). In both demonstrations, the

functionality of VLP-FLAG has been confirmed by selectively inducing signal changes (optical resonant frequency shift and change in impedance, respectively) due to the presence of target analyte, anti-FLAG antibodies. Further optimization of the sensor performance was conducted using the impedance sensing platform.[135] By incorporating an evaporation-assisted immobilization strategy, the very recent work by my former colleague was able to demonstrate label-free immuno-sensing, achieving an unprecedented detection limit of ~60 pM of anti-FLAG-antibodies with the impedance sensing platform.

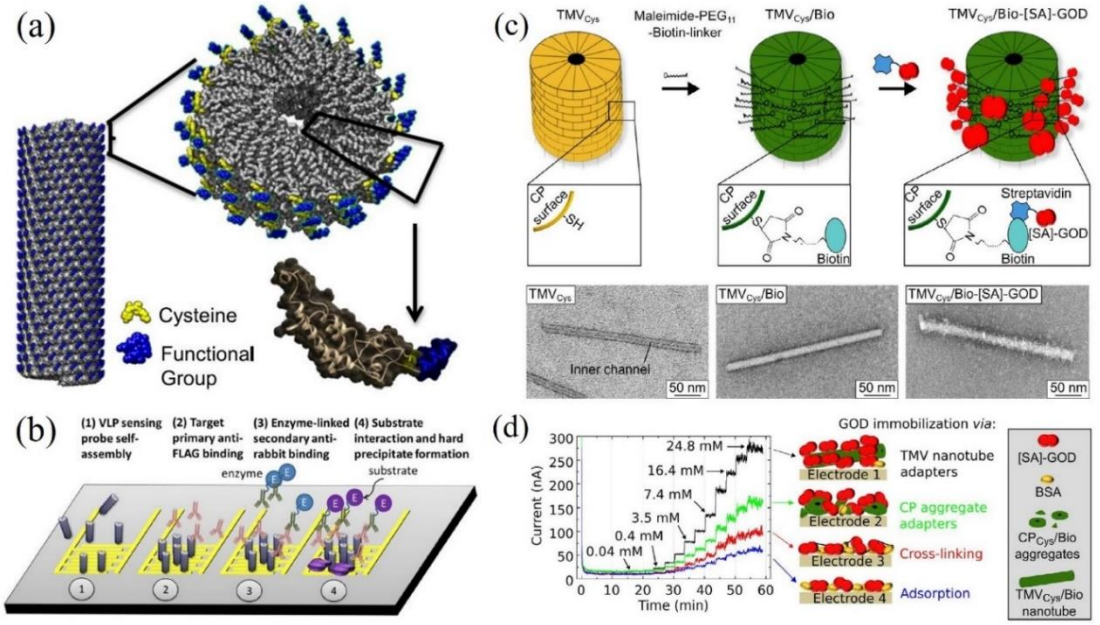

Figure 1-9. (a) Schematic representation of VLP-FLAG displaying both FLAG-tag (functional group) and cysteines on outer surfaces.[134] The VLP-FLAG has been utilized as immuno-biorecognition elements on impedimetric sensing plat forms as described in (b).[129] (c) Schematic of TMV-enzyme chemical conjugation process using hetero bifunctional crosslinkers. TEM images at corresponding synthesis stage show change in surface morphology of TMV due to molecular binding. (d) Characterization of enzymatic sensing performance at different immobilization conditions show best performance with full-length TMV-scaffolds.[52]

Use of TMV1cys as an enzyme-immobilization template was introduced by Wege and co-workers.[136] The thiols on the cysteines provide a facile chemical

conjugation route to link biorecognition element through chemical crosslinkers (Figure 1-9c). They have utilized the hetero-bifunctional crosslinker maleimide and biotin connected through a polyethylene glycol (PEG) bridging arm. The maleimide readily forms a covalent bond at pH7 with surface exposed thiols on TMV1cys. On the biotin-end, enzymes (glucose oxidase (GOx) and horseradish peroxide (HRP)) conjugated with streptavidins were functionalized, occupying at least 50% of cysteine residues on TMV surface. As a follow-up work, Schöning and co-workers (in collaboration with the Wege group) have recently integrated GOx conjugated TMV1cys (TMV-GOx) onto Pt electrodes for the demonstration of enzymatic sensing.[52] Using an amperometric electrochemical sensing scheme, as is widely used for glucose sensors, they have achieved a wide linear concentration range of 0.1 to 7.4 mM of glucose, covering the range relevant to human blood samples at 4.9 nA/mM sensitivity per 1 mm^2 electrode area. Also, reproducibility of sensing performance was evaluated by running 40 consecutive measurements over three days. Sensitivity remained constant after two days and retained ~60% of original sensitivity after three days. Based on their survey analysis, the enzymatic sensing performance of TMV-GOx are comparable with carbon nanotube (CNT)-based enzyme-electrodes in a similar electrode scheme, emphasizing the strength of TMVs for the development of high performance biorecognition elements. Additional interesting aspects of their studies include the comparative characterization of TMV rod-length dependence (enzyme-only vs. CP aggregates vs. full length) on sensing performance (Figure 1-9d). As expected, the GOx immobilized on full TMV1cys rods resulted in enhanced sensing signals, with less interruption from noise and faster response time (5 seconds).

In summary, the unique geometrical and biochemical characteristic possessed by TMV and its derivatives coupled with genetic modification and chemical conjugation technologies bring exciting motivation and opportunities to exploit these bionanoreceptors as smart biochemical recognition elements towards a wide range of biosensing applications. The readily available primary functionalities - multivalent receptors contributing to both immobilization and selective target recognition - of the bionanoreceptors imply strong potential as universal biorecognition elements.

1.3.3. Three-Dimensional Materials for Bioelectronics

Including TMV nanoscaffolds, various types of three-dimensional (3-D) structures with feature dimensions in the micro and nanometer scale regimes offer a number of advantages for miniaturized devices and systems including enhanced active surface area, improved packing/loading density and energy efficiency, etc. The obvious beneficial impact of 3-D structures for microsystems drove development of MEMS fabrication technologies such as the LIGA[137] or deep-reactive-ion-etching (DRIE)[138] processes to achieve true three-dimensional high-aspect-ratio geometries of device components at micro/nanoscale. The recent appearance of 3-D printing technologies (fused deposition modeling, sterolithography, polyjet printing, selective laser sintering, two-photon lithography, etc.) provide alternative means for creating complex 3-D structures with more degrees of freedom feature shapes (spherical, tetragonal, etc.) and their arrangement.[37] It needs to be noted here that, although current 3-D printing technologies are more user-friendly, easy-to-implement, and require less environmental control compared to MEMS fabrication, certain limitations such as poor printing resolutions, need for supporting materials/structures, and narrow range in

compatible materials (plastics, photo-curable polymers and resins, metals) have limited their wide-spread use for development of active miniature devices. In efforts to broadly adapt 3-D printing for micro/nano device fabrication, innovative strategies and synthesis of advanced functional printable materials are under development.[37,139,140] The 3-D micro/nano manufacturing technologies (MEMS fabrication and 3D Printing) are evolving continuously and advances in microsystems' components are leveraging the available resources to achieve unprecedented capabilities in a miniaturized environment. While there are innumerable reports demonstrating the effectiveness of 3-D structures for a variety of applications (energy storage and harvesting devices, micro heat management, textile sensors, photonic crystals, surface coating, etc.), the literature review below will focus on some of the recent reports utilizing 3-D micro and nano structures for the development of biochemical sensors with a strong emphasis on their benefit for sensing performance. The principles and methodologies incorporated in transducers used for biochemical sensors include electrochemical impedance spectroscopy,[129,141] optical resonance spectroscopy,[34,134] electrochemical current analysis,[130,142] mechanical resonance spectroscopy,[143,144] etc. For the various types of transducer elements, 3-D structural elements have played significant role for enhancing sensing/transducing performances.

One prominent demonstration includes the use of 3-D nanostructured electrodes for non-enzymatic glucose sensing primarily aimed at operating without the use of enzymes (GOx) and improving long-term reusability of the glucose sensors available in the market. Nanostructured electrodes comprised of electrocatalytic materials, including metals (Au, Pt, Pd, etc.), metal oxides (Co_3O_4, MnO_2, NiO, CuO, RuO_2, etc.),

alloys, (PtPb, PtRu, etc.), and other complexes, have shown non-enzymatic glucose sensing performances with exceptional selectivity[145] (Figure 1-10 displays examples of 3-D electrodes comprised of different materials for non-enzymatic glucose sensing). In order to understand non-enzymatic and selective catalytic electrode reactions, different models (e.g. activated chemisorption model, Incipient Hydrous Oxide Adatom Mediator (IHPAM) model) have been adapted or introduced to explain the enabling sensing mechanism.[146,147] While there will be minute differences in mechanisms for different electrode material types, general understanding is that 3-D nanostructures provide well-spaced adsorption sites on the surface of the electrocatalysts with geometry that contributes to the kinetic enhancement of the glucose oxidation process. Also, the polycrystalline surfaces at the discontinuous morphology of nanostructured electrodes (grain boundaries and edges) are more easily exposed to the solution than the bulk surfaces, becoming more liable to undergo facile glucose oxidation process.

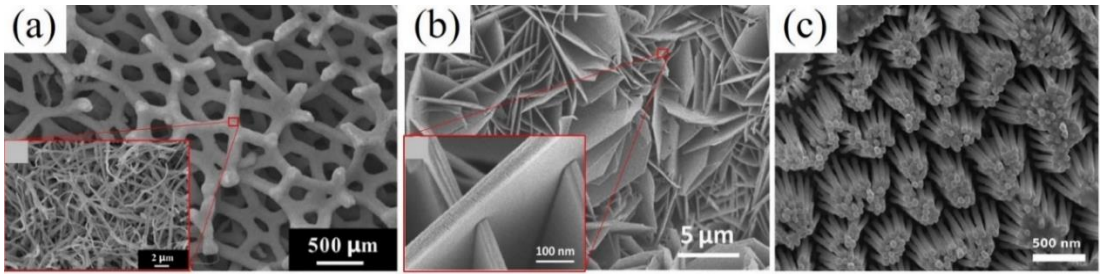

Figure 1-10. SEM images of 3-D micro/nano structured electrodes prepared for non-enzymatic glucose sensors. (a) CuO nanowires formed on 3-D Cu foam via electrochemical anodization,[148] (b) Ni-Fe nanocomposites formed on flexible carbon fiber paper via hydrothermal process,[149] and (c) Au nanowires grown by electrodeposition using porous anodic aluminum oxide template.[150]

In addition to the enzymatic sensing applications, micro-, nano-, and hierarchical- structure electrodes have been fabricated for a wide range of bio/chemical sensing applications utilizing electrochemical systems.[19,148] A recent report by Wang

and co-workers has demonstrated a 3-D electrochemical immunosensor incorporating non-covalently immobilized antibodies on free-standing macroporous graphene foam.[21] Leveraging the large surface-to-volume ratio geometry of their graphene electrode structure for label-free sensing of tumor biomarker, carcinoembryonic antigen (CEA), in serum samples with excellent performances (wide linear range of 0.1-750 nm/ml and low detection limit of 90 pg/ml). Also, Seo and co-workers have demonstrated use of graphene-based micropillar arrays to detect the small aromatic organic molecule, phenol.[151] By incorporating physisorption-based immobilization of a phenol sensitive enzyme, tyrosinase, onto the 3-D electrodes, the sensor achieved ultrahigh sensitivity of 3.9 nA/uM (linear range: 50 nM-2 μM) with a detection limit at 50 nM phenol. The use of 3-D microstructures was also found to be useful for the development of electrochemical impedance spectroscopy (EIS)-based sensors (impedimetric biosensors). Traditionally, the impedimetric biosensors utilized interdigitated electrodes (IDEs) patterned on planar surfaces.[129] The immobilization of biorecognition elements and analyte binding events induced change in the dielectric properties of the medium in between the separated electrodes resulting in a change in impedance of the electrode system. 3-D configuration of such capacitive IDE systems can enable enhanced sensor performance with a uniform distribution of electric fields across the electrodes, larger electrode surface area, and formation of a volumetric interface between the sensor electrode and analyte solution. Bratov et al. have introduced an interesting 3-D IDE designed to enhance its sensitivity for biochemical reactions taking place at the sensor surface.[152] Specifically, they placed a dielectric barrier structure in between IDEs to intensify current density within surface conductive

layer, thereby inducing higher change in electrochemical impedance at the presence of biochemical recognition events.[152,153] Their finite element model-based simulations in excellent correspondence with experimental results establish a novel 3-D impedimetric biosensing platform with high sensitivity.[154] Also, other groups have developed fabrication process to build three dimensional electrode structures on IDE sensors (e.g. micropillar arrays on IDEs,[155,156] 3-D grating electrodes [157]), and preliminary electrochemical characterization results show great potential for both non-faradaic and faradaic biochemical sensing applications.

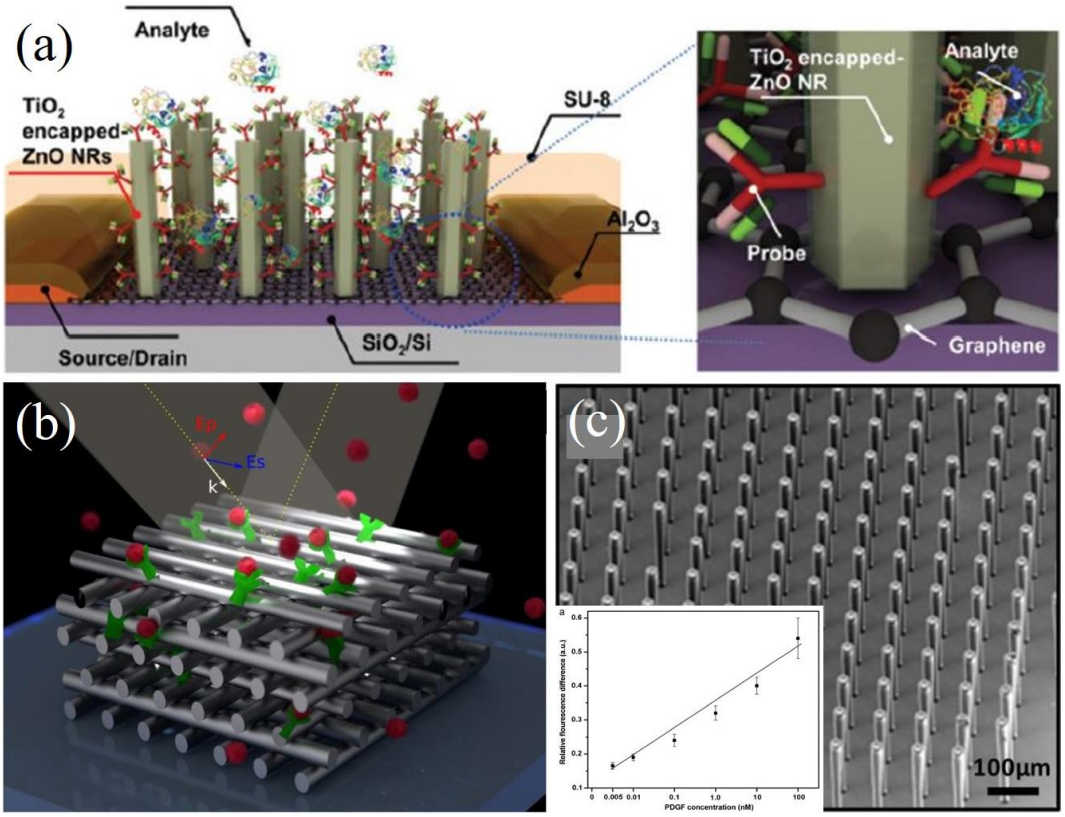

Figure 1-11. Schematic illustrations and SEM images of different sensing schemes utilizing 3-D components. (a) Schematic illustration of a 3D channel FET biosensor. The ZnO/TiO_2 gate micropillar arrays directly grown on graphene channel allows ultrafast and sensitive detection of protein analytes.[158] (b) Schematic illustration of biosensing using metamaterial. The green receptors are immobilized on the surface of 3-D surfaces and binding of analyte induces change in parameters of reflected light.[35] (c) Carbon micropillar arrays fabricated through pyrolyzing patterned photoresist was used as a high-surface-area substrate for fluorescence-based protein detection (inset graph shows linear increase in fluorescence intensity corresponding to analyte concentration).[22]

3-D micro and nano structures also has proven their utility for biosensors utilizing field-effect-transistor principles (bio-FET).[158,159] For example, Lee and co-workers have demonstrated fabrication of a graphene based bio-FET having vertically aligned and highly dense TiO_2-coated ZnO nanorods as transducing "gate" elements (Figure 1-11a).[158] The functionality of the novel 3-D bio-FET device was tested for an immuno-sensing application. By functionalizing prostate specific antigen (PSA) antibody as a biorecognition element on the 3-D surfaces, they were able to achieve an extremely large dynamic range of 10^7 and a sensitivity of 8 mV/dec (obtained from charge neutrality point) for detection of PSA. More exciting results include performance comparison with 2-D bio-FET confirming enhanced sensitivity (2.5 mV/dec to 8 mV/dec) and extremely fast response time (several tens of minutes~hours down to ~1 min).

Additional transduction platforms utilizing 3-D device platforms include optical sensing platform such as photonic crystal-based biosensors[35,160,161] or fluorescent biosensors[22] as shown in Figure 1-11b and 11c, respectively. Combined, 3-D structural components in micro and/or nanometer scales have proven an excellent ability to enhance biochemical sensing performances. Fabrication strategies for creating reproducible and robust 3-D structures and their physical and chemical compatibility with working bio/chemical molecules per adapted transduction mechanisms are the key considerations for successful demonstration of 3-D biochemical sensors/bioelectronics.

1.3.4. Enzyme-based Bioelectronics

As discussed in the introduction, enzymatic reactions integrated with microdevices and systems offer great opportunities for the advancement of

bioelectronics research and applications. The majority of developments have involved the use of glucose oxidase (GOx). In this section, technical backgrounds and future challenges of the two major areas of enzyme-based bioelectronics - enzymatic biosensors and EBCs - will be discussed in brief.

Enzymatic biosensors

Ever since Clark and Lyons introduced the first enzyme sensor employing glucose oxidase (GOx) and an oxygen electrode for glucose monitoring, extensive studies have been carried out to develop improved enzyme-based systems focused on monitoring various levels of analytes including glucose, lactate, glutamate, and cholesterol for a range of clinical applications.[10,162] Glucose is by far the most extensively studied analyte. It continues to attract considerable attention due to its importance in diabetes management, but also in glucose-based.

Over the generations of enzymatic sensor research toward more sensitive, stable, and continuous monitoring systems, the sensing mechanisms, materials, and electrode immobilization strategies have evolved to meet clinical requirements on demand. Figure 1-12a illustrates the amperometric glucose sensing principles developed along the course of research towards a more sensitive and stable system.[10] It is categorized into three distinctive generations. The first generation of enzymatic sensors employed oxygen as the electron acceptor, determining glucose concentration by following either consumption of oxygen or the liberation of hydrogen peroxide. In second generation, enzymes transfer electrons to artificial electron acceptors (also referred to as electron mediators or redox dyes) instead of oxygen to avoid interference from other redox species. The reduced mediators are monitored colorimetrically or

electrochemically. The third (or current) generation sensors employ direct electron transfer to the electrode, thus eliminating toxic artificial electron mediators and avoiding errors due to variations in the concentration of oxygen in blood samples.

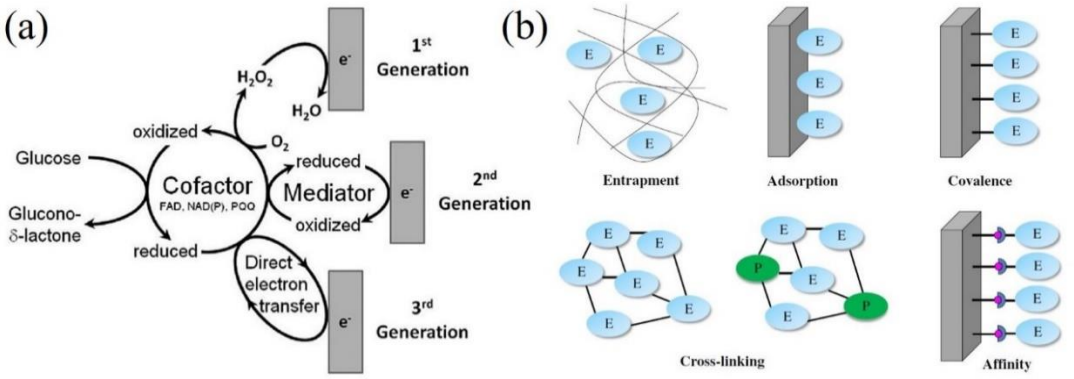

Figure 1-12. Schematic representations of (a) enzymatic electrocatalytic reactions,[10] and (b) enzyme surface immobilization strategies (E: enzymes, P: insert proteins).[64]

One of the key components impacting enzymatic sensor performance includes immobilization of enzymes onto electrode/transducer surfaces. It has been reported that the appropriate immobilization strategies can result in improvement in sensor life-time, sensitivity, and selectivity.[64] Hence, intensive efforts have been made to develop successful immobilization strategies. As illustrated in Figure 1-12b the enzyme immobilization techniques include use of simple physical adsorption, polymer/gel binders (entrapment), cross-linkers, and affinity or covalent binding to device surfaces.[64] Each technique has pros and cons in terms of enzyme activity, analyte diffusion, enzyme orientation, and level of complexity in immobilization processes.

The countless reports on enzyme-based sensors, reporting a range of fabrication strategies to improve sensing performance, provides as a great benchmark for assessment of this research. It is anticipated that utilization of TMV particles as stable

and high-density enzyme carrier supports will allow significant enhancement in sensing performance including sensitivity and long-term stability.

Enzymatic biofuel cells

EBCs are a type of fuel cell that utilizes enzymes as the electrocatalysts to catalyze oxidation of fuel (substrates) on anodes and reduction of oxygen or peroxide (oxidants) on cathodes for energy conversion to electricity. Due to the sustainable nature of the energy harvesting mechanism, it is considered a promising resource for the operation of low-power electronics or implantable devices.[14] Both the enzymatic sensors and EBCs share many identical system components impacting their performance ranging from enzymes, substrates, mediators, and the charge transfer mechanisms involved for collecting electrons from enzymatic reactions to electrodes. However, a complete fuel cell system (Figure 1-13) adds slightly more intense considerations onto system components (electron transfer mechanisms, pair of cathodic and anodic enzymes, enzyme activity and immobilization density, etc.) in order to increase the energy harvesting performance (energy and power densities), which has no upper boundary for satisfaction.

Figure 1-13 describes the typical system components comprising EBCs. On the anodic electrode (left), the mediated electron transfer (MET) mechanism is described where the electrons generated from oxidation of substrates in the presence of the enzyme reaches the electrode through mediators. On the other side (right), the direct electron transfer (DET) mechanism is described for the cathodic reactions where the electrons from the electrodes are delivered to the enzymes without the mediator. From an energy harvesting perspective, researchers desire to eliminate mediators in order to

increase operation potential window of EBCs. Also, the multiple charge transfer reactions are not favorable which may limit the maximum operational power range.

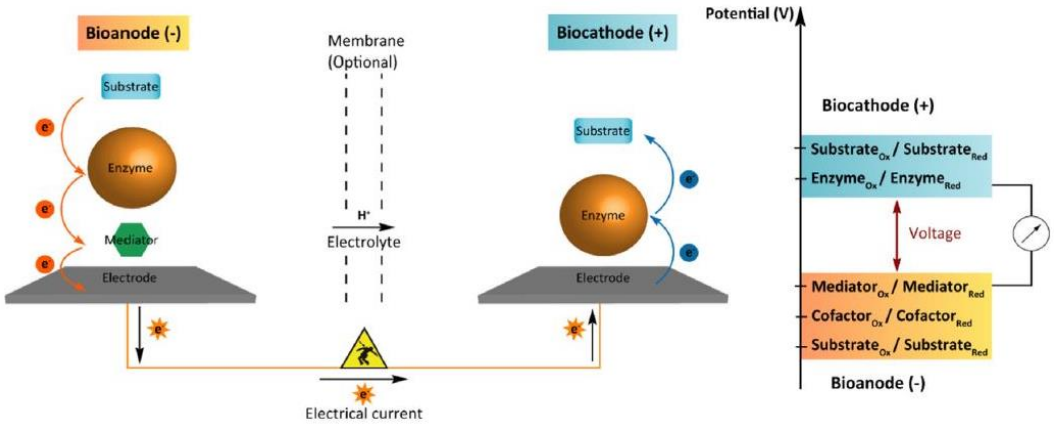

Figure 1-13. Schematic of an EBC utilizing a MET-based bioanode and a DET-based biocathode.[16]

Interestingly however, although the DET mechanism has become the goal for EBC development, most EBCs in literature continues to utilize MET, mainly because the MET systems typically resulted in higher current densities, even though they have higher potential losses and issues with mediator stability. This is attributed to the stringent requirement in orientation and proximity of immobilized enzymes to the electrodes for DET. In other words, DET system will only collect electrons from a sheet of enzymes that are located very close to the electrode surfaces (<15 nm) while the MET system could harvest from a volume of enzymes through mediators.[163] This implies that, irrespective to the electron charge transfer mechanisms involved, it is essential to induce high density catalytic reactions with robust enzyme immobilization for advanced energy harvesting performance.

1.4. Structure of Dissertation

Chapter 1 has presented the motivation and the literature reviews to provide the aims and scope of this thesis research. The following three chapters will introduce the major accomplishments achieved through out this work. Chapter 1 will present the materials and strategies to demonstrate hierarchical construction of bio-integrated 3-D devices along with the fundamental understandings behind the potential limitations associated with material wetting properties. Chapter 3 will introduce the development of an electrowetting-assisted 3-D biofabrication technology enabling programmable and scalable patterning of biological molecules onto 3-D device substrates. Chapter 4 will introduce the development of an on-chip bioconjugation method for high-density immobilization of enzymes using TMV particles as a robust template. The 3-D biofabrication technique will be incorporated into the enzyme immobilization process to demonstrate scalable and enhanced biomolecular activity on chip. Chapter 5 will provide summary and conclusion of this thesis research with potential future research.

Chapter 2: Integration of Biomacromolecules with High-Aspect-Ratio Microstructures

Integration of biological molecules into microfabrication processes has been extensively explored for the development of a wide range of micro-/nano-devices. Their nature-inspired structural and functional versatility combined with advances in biology and bioengineering has great advantages for creating tailored nanoscale functionalities on devices for a numerous applications including energy storage and sensing devices.[164] To further enhance the device functionality, the TMV nanoscaffolds were integrated with gold micropillar array (μPAs) to create hierarchical structures. This is one of the most effective ways to create high surface area electrodes, taking advantage of building blocks with different length-scales.[136] However, TMV self-assembly suffers from limitations on high surface area microstructures, showing reduced bio-nanoparticle surface coverage on the vertical and bottom surfaces of high-aspect-ratio (HAR) geometries.[165] In this the dissertation thus far, critical geometric parameters of the microstructures that govern the virus assembly morphology have been characterized, enabling the use of optimized bio-templated hierarchical architectures. Additionally, the enhanced functionality of the high-surface-area electrodes created by successful integration of TMV and microstructured electrodes has been evaluated in a NiO based electrochemical charge storage system with a detailed study of correlation between charge storage performance and change in electrode morphology.

2.1. Design and Fabrication of 3D Microdevice Component: Micropillar Arrays

While high density microstructures are desirable due to the increased surface-to-volume ratio of 3-D structures, the previous work reported by Gerasopoulos et al.[115] implies that biofunctionalization on such geometries may become limited by surface tension of liquid at the microscale. In order to clearly understand the limiting principle, Au-coated Si-based μPA electrodes having different geometries have been designed as model 3-D electrode structures.

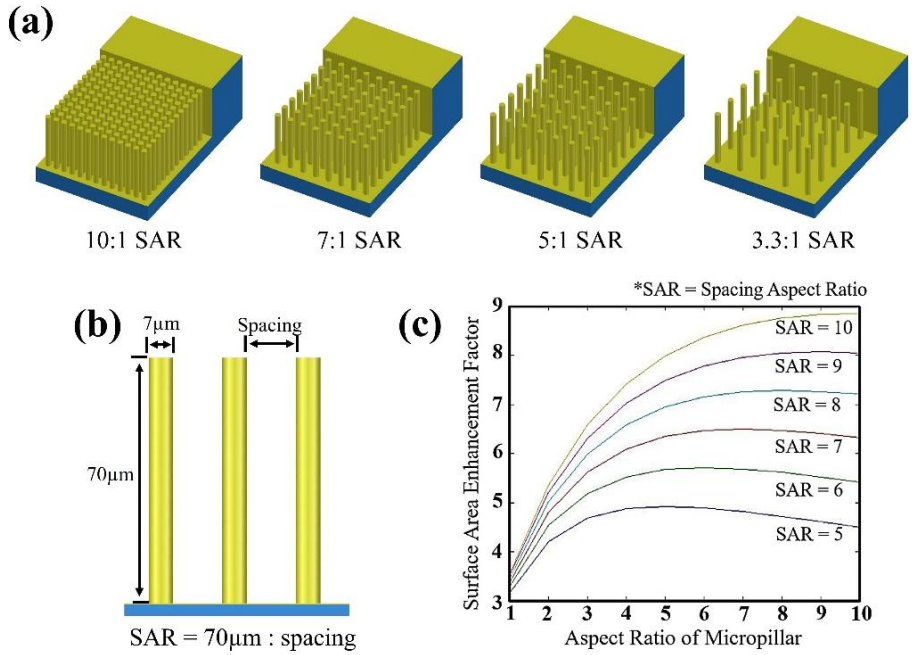

Figure 2-1. Schematics of (a) the four micropillar array substrates in different geometries and (b) the dimension factors shown in cross-sectional view. (c) The plot shows the surface area enhancement factors that could be achieved by modulating pillar and SARs.

A set of μPA electrodes having varying pillar densities have been designed, as described in Figure 2-1. All pillars have been designed to have 10:1 aspect-ratio with 7 μm diameter and 70 μm height, while the spacing between the nearest neighboring pillars were varied from 7 μm to 21 μm. This results in spacing aspect-ratios (SARs)

of 10:1, 7:1, 5:1, and 3.3:1 with the 70 µm etched trench height (Figure 2-1b). The plot shown in Figure 2-1c explains the role of the two parameters – spacing and pillar aspect ratios – for determination of the surface area enhancement factor of the µPAs; The theoretical surface area enhancement factor (E) was calculated based on the parametric equation ($E = 1 + (\pi \cdot d \cdot h)/s^2$) introduced by Gerasopoulos et al.[24] The parameter d is the pillar diameter, h is the pillar height, and s is the distance between nearest neighboring pillars (center to center). Considering that the functional density and surface area of TMV itself is predetermined by nature, it is important to load TMV particles onto high density µPAs to achieve greater functionality of the resulting hierarchical components.

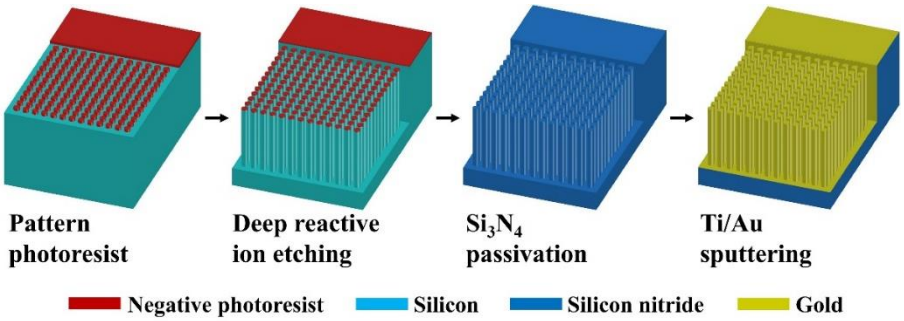

Figure 2-2. Microfarbication process flow for the Au-coated micropillar arrays.

The fabrication process for the µPAs is illustrated in Figure 2-2. A silicon substrate has been patterned with a negative photoresist (NR-9 1500PY) at a thickness of ~1.5 µm, and the trenches are etched using deep-reactive-ion-etching (DRIE, UMHigh recipe at University of Maryland Nanocenter FabLab). The etch selectivity between the photoresist and Si substrate was higher than 100, with only ~0.5 µm of the photoresist etch mask removed after 70 µm etching of Si (~0.55 µm/DRIE cycle). The etched wafer was diced into a chip scale with dimension of 1×1.7 cm^2 (1×1 cm^2 pillar

array area), and both sides of the electrode were passivated with 500 nm PECVD Si_3N_4 at 300 °C followed by sputter deposition of Ti (30 nm)/Au (120 nm).

2.2. TMV Self-Assembly on Micropillar Arrays Exhibiting Varying Structural Density

As described in Figure 2-3, three approaches for nanotexturing the μPA electrodes were investigated – (1) typical, previously published TMV self-assembly and metallization protocol,[114] (2) pre-treatment of the electrodes using isopropyl alcohol (IPA), and (3) ultrasonication after the immersion of the electrode into TMV solution. (1) The typical process involves overnight self-assembly of TMV particles during immersion of the Au-coated electrode into 0.2 mg/ml TMV solution in 0.1 M phosphate buffer (pH 7); an 18-hour incubation is allowed for surface self-assembly via thiol-gold binding.[114] Subsequently, an electroless Ni metallization process follows initial Pd surface activation. (2) For the IPA pre-treatment, the μPA electrodes were rinsed and immersed in IPA for 5 minutes followed by the TMV self-assembly and metallization. (3) For ultrasonication, the electrodes were immersed in the TMV solution and placed in an ultrasonic bath for 5 minutes prior to overnight self-assembly and metallization. The IPA treatment was intended to increase hydrophilicity of surfaces with hydroxyl groups, which can lead to enhanced wettability of the array structure. The ultrasonication is intended to facilitate TMV diffusion into the microcavities between pillars by agitating the virus solution within the array structure. The goal is to identify the threshold geometrical parameters at which limited functionalization occurs and convert such limitation into a control parameter for patterning TMVs onto 3-D structure surfaces.

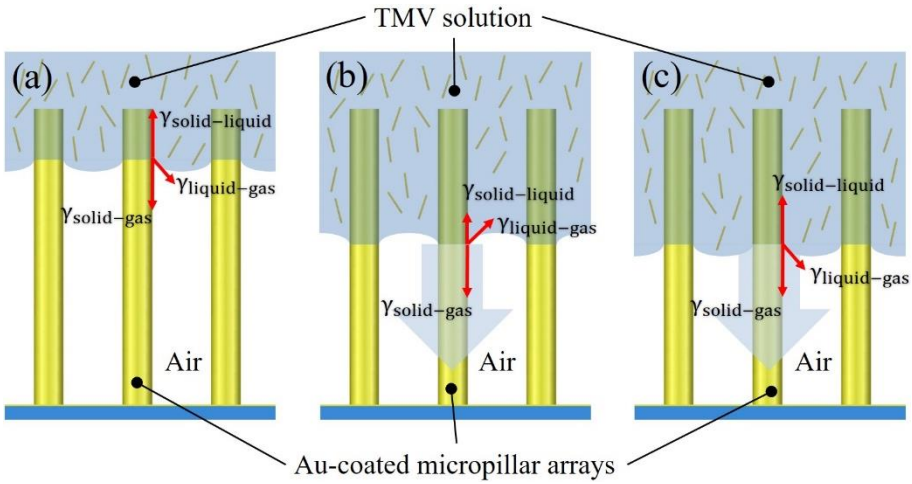

Figure 2-3. Illustration of TMV solution wetting on the Au-coated μPAs in three different approach; (a) traditional method, (b) pretreatment of the electrodes with IPA for enhanced surface wettability, and (c) ultrasonication to remove air medium through induced mechanical agitation.

The immobilization of TMV particles onto the different micropillar arrays were first characterized using the standard method. Figure 2-4 shows a series of cross-sectional scanning electron micrographs (SEMs) of TMV immobilized μPAs acquired after electroless Ni metallization (the detailed protocol is explained in a previous report by Royston et al.[114]). As clearly shown, while the pillars located at the edge of the arrays display complete nanotexturing of their side-wall surfaces by the TMV immobilization (Figure 2-4a – 4d), the pillars located at the center of the arrays showed a gradual reduction of virus surface coverage towards the bottom of the pillars correlated to decreasing SAR (Figure 2-4e-h). Uniform TMV assembly was achieved only on pillar arrays with 3.3:1 SAR (Figure 2-4h). This, combined with the TMV assembly profile from the edge towards the center of the pillar arrays (Figure 2-4i, 7:1 SAR), is evidence that the reduced TMV assembly density in the deep microcavities can likely be attributed to the surface tension of the TMV solution on the structurally hydrophobic pillar arrays (further discussed in Chapter 3).

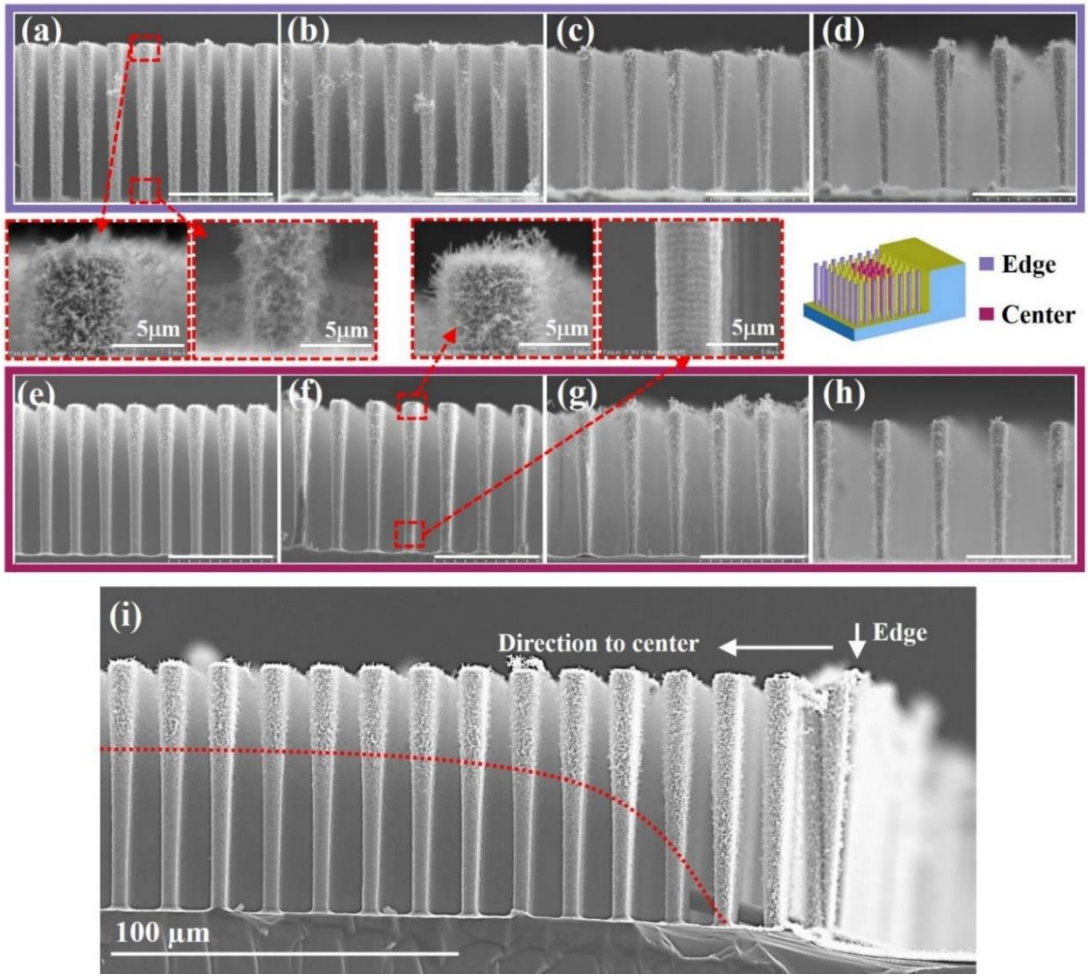

Figure 2-4. Cross-sectional SEM characterization of traditional TMV functionalization process on micropillar arrays having different SARs. (a-d) Complete coverage of TMV are achived on the sidewalls of the pillars located at the array edge. However, gradual decrease in TMV coverage is observed at the lower part of the pillar surfaces located in the array center region with increase in SAR ((a,e) 10:1 SAR, (b,f) 7:1 SAR, (c,g) 5:1 SAR, (d,f) 3.3:1 SAR, scale bars: 50 µm unless specified). (i) The limited access of TMV solution into the 7:1 SAR pillar arrays resulted in creation of TMV-nanotexture profile from edge to the center.

Based on the identified limitations, efforts were made to induce enhanced wetting of the microcavities with TMV solution. First, pre-treatment of the µPAs was attempted with a low surface energy/tension liquid. Therein, the substrate was first immersed in isopropyl alcohol (IPA) for 5 minutes to increase the surface wettability and then transferred into TMV solution for the overnight self-assembly. Another method investigated using ultrasonication was intended to induce mechanical agitation thereby removing the air trapped underneath the liquid and introduce TMV solution

into the cavities. For this, plastic containers with the micropillar array substrate immersed TMV solution were placed in the ultrasonicator for 1 minute and left overnight for self-assembly.

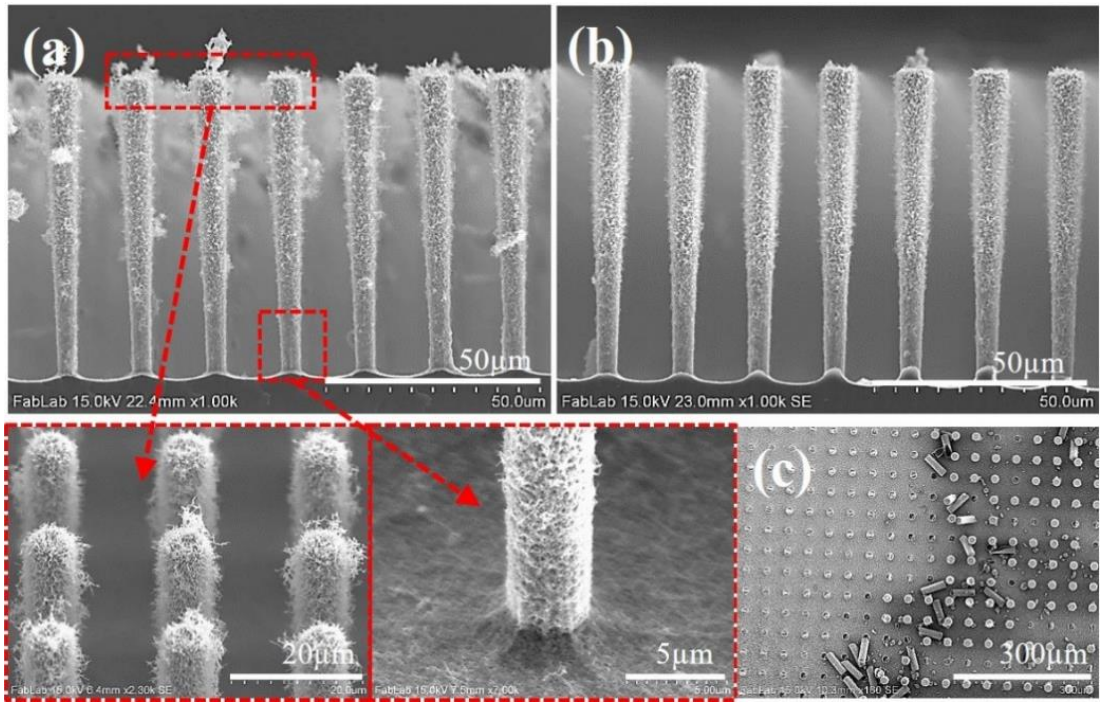

Figure 2-5. SEM images taken from the TMV functionalize micropillar arrays (7:1 SAR) using (a) IPA pre-treatment, and (b,c) ultrasonication.

The SEMs in Figure 2-5 show the results from µPAs (7:1 SAR) located at the center of electrodes treated with IPA (Figure 2-5a) and ultrasonication (Figure 2-5b and 5c). When compared with Figure 2-4f for the same SAR, an obvious improvement of the virus coating is observed from both methods. However, a significant fraction of pillars collapsed during ultrasonication due to the induced mechanical agitation (Figure 2-5c). With the IPA pretreatment, while the extent of TMV coating on the deep surfaces has improved, it showed poor conformality from top to bottom of the pillar surface – low density of TMVs are observed at the bottom compared to more complex clusters

toward the top (compared in the zoom-in SEMs). While the IPA treatment was effective for SAR up to 5:1 (IPA treatment yielded homogeneous TMV coating for 3.3:1 and 5:1 SAR micropillar arrays, while 7:1 SAR geometry still showed poor coating at the bottom (Figure 2-5a)), these results indicated the need for further study and improvements for complete loading of TMVs onto high SAR micropillar arrays which will be further addressed in Chapter 3.

2.3. Enhanced Electrode Functionality in Electrochemical Charge Storage System

The performance of the hierarchical Ni electrodes assembled by combination of TMV1cys and the μPA (SAR 5:1) electrodes has been characterized in NiO-based electrochemical charge storage (ECS) system. This section will provide background and motivation behind the application of TMV-μPA assembled hierarchical electrodes for such ECS system as well as the characterization results for NiO forming process on the hierarchical Ni surface and enhanced electrochemical charge storage performances.

ECS devices including Li-ion batteries and electrochemical capacitors have received significant attention due to the rapidly growing electronics market (e.g. electric vehicles, portable electronics, etc.) requiring charge storage devices with both high power and energy densities.[166] Particularly, the recent development of faradaic electrode materials in micro/nanoscale geometries is one of the most significant advancements, where the high surface area-to-volume ratio coupled with facile charge storage kinetics are essential for reaching the desired performance criteria.[97,167]

Various transition metal oxides (Co_3O_4, MnO_2, NiO, etc.) and their composites are very attractive candidates for the high performance ECS electrodes owe to their excellent faradaic charge storage characteristics at economic costs. Among the

potential candidates, NiO brings great interest with its excellent "battery-like" charge storage behavior exhibiting very high theoretical gravimetric capacities of 359 mAh g^{-1} and 718 mAh g^{-1} in alkaline ($NiO + OH^- \leftrightarrow NiOOH + e^-$, in 0 - 0.5 V vs. Ag/AgCl) and Li^+ ($NiO + 2Li^+ + 2e^- \rightarrow Ni + Li_2O$, in 0.005 - 3 V vs. Li-foil) electrolytes, respectively.[168,169] For this reason, many researchers have recently investigated the use of NiO as electrode materials for both electrochemical capacitors and Li-ion batteries. Luan et al.[170] have demonstrated an asymmetric supercapacitor device combining NiO nanoflakes (cathode) and reduced graphene oxide (anode) grown on carbon cloth and Ni foam, respectively. The asymmetric configuration allowed expansion of the operation potential window up to 1.7 V in alkaline electrolyte (1 M KOH) with remarkable areal capacitance (248 mF cm^{-2} at 1 mA cm^{-2}) benefiting from the high surface area NiO electrodes. Also, nanoscale NiO has been investigated as an anode material for Li-ion batteries in recent years for its high theoretical Li capacity compared to conventional graphite anode materials. Characterized in half-cell configuration (vs. Li-foil), many articles have reported reversible gravimetric energy density reaching or exceeding its theoretical limit at 1C current rate, representing more than a 2-fold increase compared to conventional carbon-based anode materials.[169,171,172] It should be noted here that the charge capacities in previous ECS NiO reports have been evaluated in different units depending on their targeted ECS systems (F g^{-1} or F cm^{-2} for electrochemical capacitors, and mAh g^{-1} or mAh cm^{-2} for batteries). Considering a recent report by Brousse et al.[173], suggesting classification criteria for proper categorization/characterization of electrode materials for electrochemical capacitors, the charge capacities in this work are presented in μAh cm^{-2} considering the NiO's

"battery-like" electrochemical signature.

Various methods for fabrication/synthesis of micro/nanoscale NiO electrodes have been reported. In general, NiO was either directly synthesized on Ni or other current collectors, or prepared in nanoparticle forms, which requires mixing with polymer binders and conductive additives.[169,171,174–179] Comparing the two methods, the latter suffers from lack of electrical connectivity between the current collector and the active material while the direct synthesis methods ensure continuous connection between the two electrode components critical for efficient charge adsorption/transfer mechanisms at the electrolyte/electrode interface. Using this approach, Wang et al.[178] achieved 99% of NiO's theoretical gravimetric capacity (355 mAh g^{-1} in 2 M KOH) by annealing $Ni(OH)_2$ precursors that were directly precipitated on Ni foam. The uniform nanoscale active layer coating over the current collector is believed to be one of the key factors in achieving high NiO-based ECS performances, compensating for the low electrical conductivity of the NiO.[177,178,180]

In the past decade, our group and collaborators have reported the use of genetically modified TMV particles as nanostructured templates for various ECS devices. Integrating the TMV process with microfabrication techniques, Ni-coated TMVs (TMV/Ni) have served as nanoscale three-dimensional current collectors for Li-ion battery and supercapacitor electrodes.[24,117,119,121] These nanoelectrode architectures have relied on additional thin-film deposition steps for the formation of uniform ECS layers on the TMV/Ni.

A NiO-based ECS system was selected for the evaluation of the hierarchical Ni electrodes based on our expertise in evaluating ECS electrode materials. This also

extends the library of TMV-based ECS electrodes by incorporating new electrochemically active material (NiO) which has not been investigated before. The formation of NiO layer on TMV/Ni surfaces were enabled by simple thermal annealing process in a box furnace filled with air. The thermal annealing process is characterized using X-ray photoelectron spectroscopy (XPS, Kratos AXIS 165 spectroscopy), and transmission electron microscopy (JEM 2100 FEG-TEM) with scanning TEM (STEM) and electron energy loss spectroscopy (EELS) capabilities. As-prepared electroless Ni on TMV is metallic with residual oxides (NiO) and hydroxides ($Ni(OH)_2$) on its surface.[114] Thermal oxidation at high temperatures can result in removal of $Ni(OH)_2$ and increase in the NiO content as illustrated in Figure 2-6. For process optimization, TMV/Ni electrodes are annealed at four different temperatures - room temperature, 200 ºC, 300 ºC, and 400 ºC - in an air-filled box furnace. The temperatures were ramped at a rate of 5 ºC min^{-1} to the target temperatures and spontaneously cooled down to room temperature after a 2-hour annealing step.

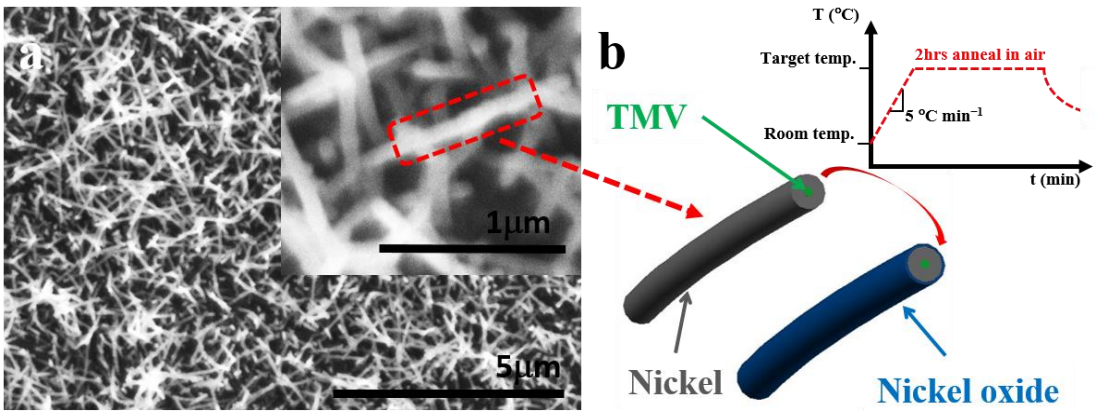

Figure 2-6. (a) Top-down SEM image of TMV/Ni nanostructure and (b) schematic description of thermal oxidation process for creating NiO-shell layer over TMV/Ni-core.

XPS is a surface sensitive analysis method that allows clear observation of the increase in NiO content on TMV/Ni surfaces with the increase in annealing temperatures. Figure 2-7 compares the XPS spectrum of Ni $2p_{3/2}$ and O 1s (electron orbitals) from the four samples, and three clear indications of NiO formation are observed from the spectrum analysis: (1) NiO formation over the Ni surface results in the peak intensity/area percentage reduction and increase at 852.2 eV (Ni $2p_{3/2}$, Figure 2-7a-c) and 529.5 eV (O 1s, Figure 2-7e-f), respectively, with more abrupt change at 300 °C. (2) The plots in Figure 2-7d and 2-7h are unique spectrum configurations for crystalline nickel oxide with the peaks revealed at 854.2 eV and 529.5 eV for Ni $2p_{3/2}$ and O 1s, respectively.[181] (3) The complete removal of the peak at 852.2 eV from Ni $2p_{3/2}$ indicates increased growth of NiO on/into the Ni at higher annealing temperatures.[182]

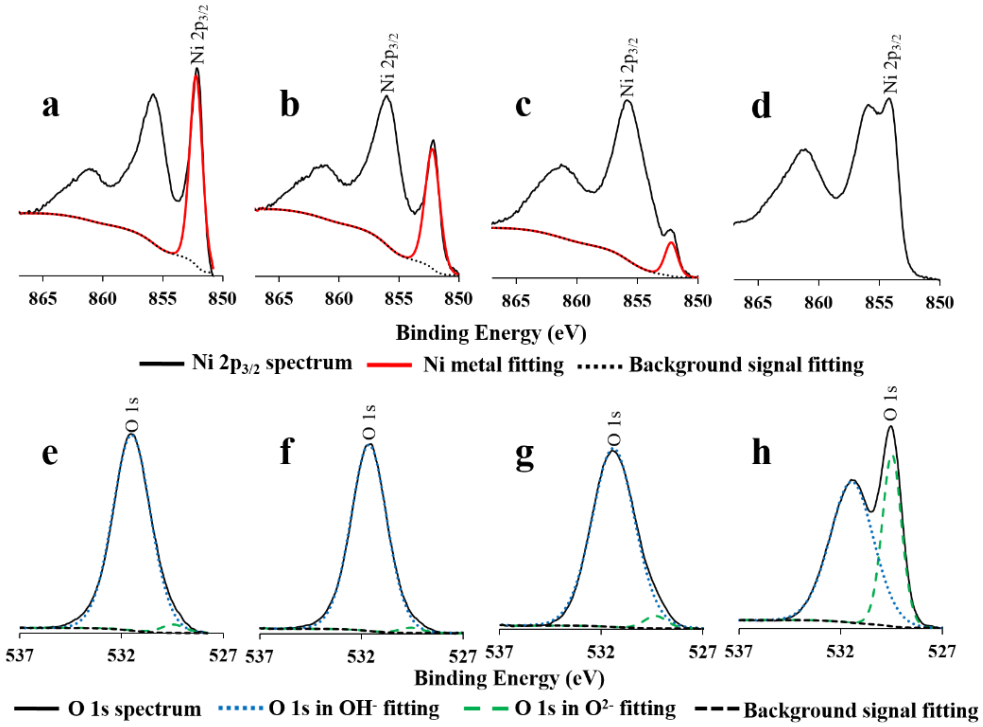

Figure 2-7. XPS analysis of (a-d) Ni $2p_{3/2}$ and (e-h) O 1s from the TMV/Ni electrodes annealed at different temperatures; (a, e) room temperature, (b, f) 200 °C, (c, g) 300 °C, and (d, h) 400 °C.

The uniform formation of NiO on a TMV/Ni nanorod after the 300 ºC annealing process is verified by STEM in Figure 2-8a. The obtained high-angle annular dark-field (HAADF) image clearly shows the TMV/Ni-core covered by NiO-shell via image contrast variation reflecting the differences in atomic numbers of the constituent materials. Also, the EELS analysis further confirms the core-shell nanorod structures with Ni and O scanning profiles along the cross-section of the rod structure. The resulting TMV/Ni/NiO nanorod electrode features ~ 130 nm final thickness, predominately defined by duration of electroless Ni coating process (4 minutes), with uniform coating of a thin NiO active layer having continuous electrical connection with the underlying Ni current collector. The thickness of TMV/Ni/NiO nanorod electrode is ~50% thinner than previously reported TMV templated electrodes (TMV/Ni/TiO_2, TMV/Ni/Si, TMV/Ni/V_2O_5, etc.), which required additional deposition of 30 to 60 nm-thick active layers over TMV/Ni [24,117,121]. This represents a significant advantage of the annealing process resulting in minimal blockage of the spacings between TMV/Ni rods during the active layer formation allowing full access of electrolytes into the open nanocavities and active layers for optimal performances. The final electrode structure is shown in the diagonal and cross-sectional SEM images in Figure 2-8b and c, respectively. The fabricated Au-coated Si micropillars are approximately 70 µm tall with 7 µm and 14 µm dimensions for pillar diameter and spacing between nearest neighboring pillars, respectively. The hierarchical Ni/NiO electrodes are successfully fabricated via formation of an ultra-high density TMV-based active network over the high-aspect-ratio uPAs. As discussed earlier, the IPA treatment of the electrode surface does not hinder structural stability of TMVs during their self-assembly process yet

allows complete and uniform coating of the biological scaffolds along the micropillar surfaces into the deep microcavities (Figure 2-8c). Based on our previous reports (up to 7-fold increase in energy densities by TMV nanostructures),[24] and the calculated surface area enhancement factor (×4.5) from the micropillar arrays, nearly 30-fold increase in areal charge capacity (μAh cm^{-2}) is expected in electrochemical performance characterization.

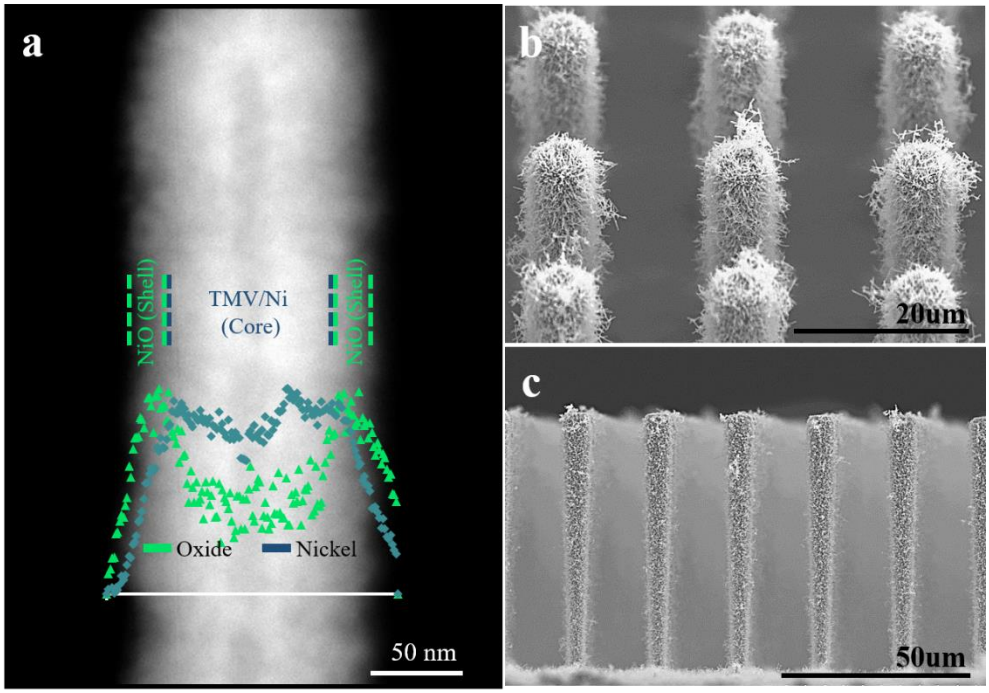

Figure 2-8. STEM-EELS analysis and SEM images of the fabricated electrodes: (a) STEM image of a TMV/Ni/NiO nanorod with EELS analysis. (b) Diagonal and (c) cross-sectional view of the hierarchical-Ni/NiO electrodes.

All electrochemical characterization is performed using a potentiostat (Biologic VSP-300) with a three-electrode-system (working: NiO electrodes, counter: Pt-foil (1×1 cm^2), reference: Ag/AgCl in 1 M KCl) immersed in 2 M KOH aqueous electrolyte ($NiO + OH^- \leftrightarrow NiOOH + e^-$). Optimal annealing temperature was characterized by testing nanostructured-Ni/NiO (TMV/Ni/NiO on planar Au substrate) electrodes in

galvanostatic charge/discharge cycles at 2 mA cm^{-2}, and the reversible charge storage behavior was characterized in cyclic voltammetry with a range of scan rates (10 – 100 mV s^{-1}). All electrochemical testing was performed within the 0 - 0.5 V potential window vs. Ag/AgCl reference electrode. The electrochemical performance of the hierarchical-Ni/NiO electrodes is evaluated in comparison with nanostructured- and planar-Ni/NiO electrodes (the planar-Ni/NiO electrodes were prepared by electroless-Ni metallization on planar-Au substrate, without TMV self-assembly, followed by the 300 ºC annealing process). The differences in charge storage performance between the three electrodes were analyzed in correlation with changes in both the double layer portion of the charge capacity and electrode morphologies (examined using JEM 2100 FEG-TEM and Tescan XEIA FEG-SEM) − in correlation with the changes in electrochemical impedance spectroscopy (EIS) − through charge/discharge cycling to investigate the cause of nonlinear charge capacity increase phenomena observed during the initial charge/discharge cycles.

Based on the XPS analysis results, nanostructured electrodes (TMV/Ni on planar Au substrate) were annealed at temperatures above 200 °C (250 °C, 300 °C, 350 °C, and 400 °C). As shown in Figure 2-9a, the areal capacity of the electrode results in a significant increase at 300 °C annealing condition (20.5 µAh cm^{-2}) compared to the 250 °C annealing condition (4.3 µAh cm^{-2}), while the electrodes annealed at higher temperatures show degraded performance with 10.2 uAh cm^{-2} and 2.2 uAh cm^{-2} for 350 °C and 400 °C annealing conditions, respectively. The significant increase at the 300 °C annealing condition can be explained by the facile thermal oxidation process of Ni at 300 °C.[183] The lower capacities measured from samples processed at temperatures

above 300 °C can be attributed to both an increase in active layer thickness which limits rate capability, and the growth of oxides on/into Ni layer resulting in loss of conductivity of the electrode system. The cyclic voltammetry (CV) curves for electrodes annealed at 300 °C, shown in Figure 2-9b, exhibit reversible faradaic reaction with clear corresponding redox peaks for NiO confirming its battery-type charge storage behavior within a wide range of scan rates (10 – 100 mV s^{-1}).

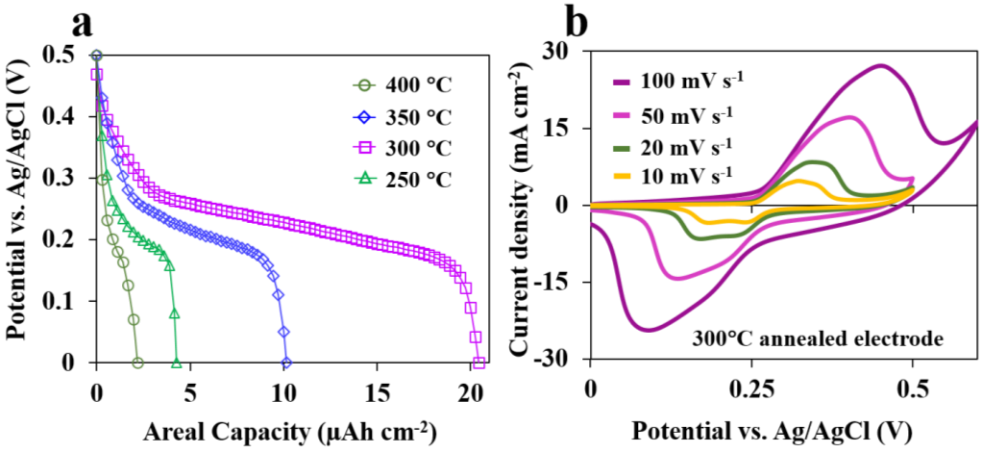

Figure 2-9. Electrochemical characterization of nanostructured-Ni/NiO electrodes; (a) Galvanostatic discharge plots of the electrodes annealed at different temperatures. (b) CV curves of 300 °C-annealed nanostructured-Ni/NiO.

In order to evaluate the increase in areal charge capacity of the hierarchical-Ni/NiO, the NiO electrodes are prepared in three different electrode geometries (planar-, nanostructured-, and hierarchical-Ni/NiO). All electrodes are annealed at 300 °C for two hours. The areal discharge capacity measured by galvanostatic charge/discharge (2 mA cm^{-2}) is compared between the three electrode types over the first 500 cycles. As shown in Figure 2-10a, the electrodes are successfully cycled with no signs of operational failure with the charge capacities ordered in expected hierarchy (planar < nanostructured < hierarchical). However, a significant nonlinear capacity increase is

observed over the 500 cycles for the nanostructured- and hierarchical-Ni/NiO (26 % and 193 %, respectively), while the planar-Ni/NiO show minimal increase of 7 %. Comparing the nanostructured- and planar-Ni/NiO, an approximately 10-fold increase in areal capacity is achieved at the 500th cycle (24.3 µAh cm^{-2} vs. 2.5 µAh cm^{-2}), which is a noticeable improvement from our previous report (7-fold increase).[24] The increased enhancement factor from 7 to 10 is assigned to the preserved TMV/Ni morphology during the active layer formation step as discussed in previous section.

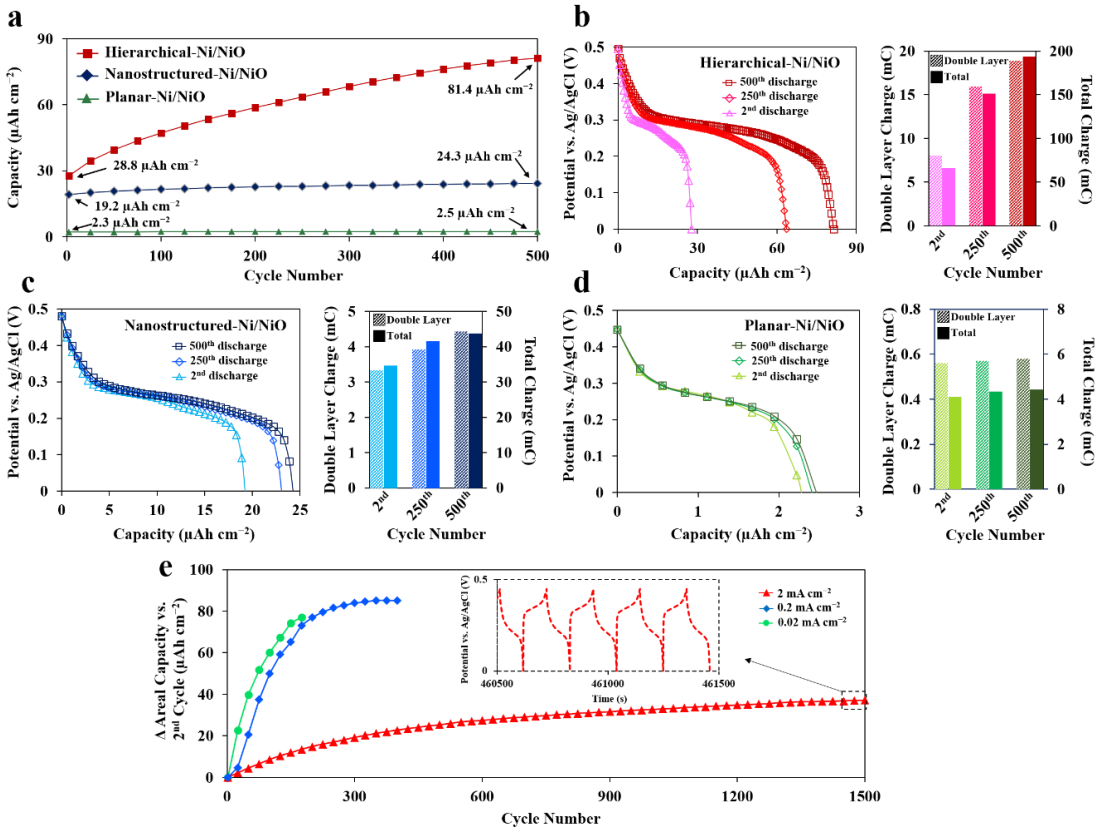

Figure 2-10. Comparisons of initial capacity increase for the three different electrode geometries; hierarchical, nanostructured, and planar. (a) Areal capacity of the three electrodes (hierarchical-, nanostructured-, and planar-Ni/NiO) over the first 500 galvanostatic cycles at 2 mA cm^{-2}. Discharge plots from 2nd, 250th, and 500th cycles with comparisons of estimated double layer and total charges in (b) hierarchical, (c) nanostructured, and (d) planar electrodes. (e) Areal capacity increase of the hierarchical-Ni/NiO at three different current densities (0.02, 0.2, and 2 mA cm^{-2}).

For the hierarchical electrode, the initial capacity is measured lower than expected. However, the capacity reaches a very high value of 81.4 μAh cm^{-2} after the nonlinear increase by the end of the 500^{th} cycle. This exceeds that of the nanostructured- (24.3 μAh cm^{-2}) and planar-Ni/NiO (2.5 μAh cm^{-2}) by 3.3 and 32.6 times, respectively. It is hypothesized that the capacity increase is due to the increase in both active material (oxidized Ni) and surface area/mesoporosity during the charge/discharge cycling.

To test the hypothesis, the change in active surface area for the different electrode structures was examined during the initial capacity increase. From the discharge plots in Figure 2-10b through 10d (displaying 2^{nd}, 250^{th}, and 500^{th} discharge cycles per electrode types), the amount of double layer charge, which greatly depends on the active surface area, is estimated from the potential range outside the major redox potential window.[184] Specifically, the double layer charge is calculated in the potential range of 0.35 - 0.5 V for the three sample types, and the values are compared with the total charge (0 – 0.5 V) at three different cycles (2^{nd}, 250^{th}, and 500^{th}). A similar increasing trend between the double layer and total charge can be observed (Figure 2-10b through 10d) from all three electrode types, which strongly supports the assumption of the active area increase during the initial cycling. It is very likely that the larger increase in areal capacity observed for the hierarchical versus the nanostructured electrodes is attributed to the dual length-scale architecture of the hierarchical electrode, particularly the micropillar morphology. The rate dependence of the capacity increase of the hierarchical electrodes has also been examined. As shown in Figure 2-10e, lower current densities show higher rate in the initial capacity

increase per cycles due to the increased time of charge diffusion at the electrode/electrolyte boundary. This result holds for all three electrodes as saturation in the areal capacity increase is reached faster at lower current densities. The hierarchical electrodes tested at 2 mA cm^{-2} show excellent cycle stability up to 1500 charge/discharge cycles without any capacity fading (Figure 2-10e).

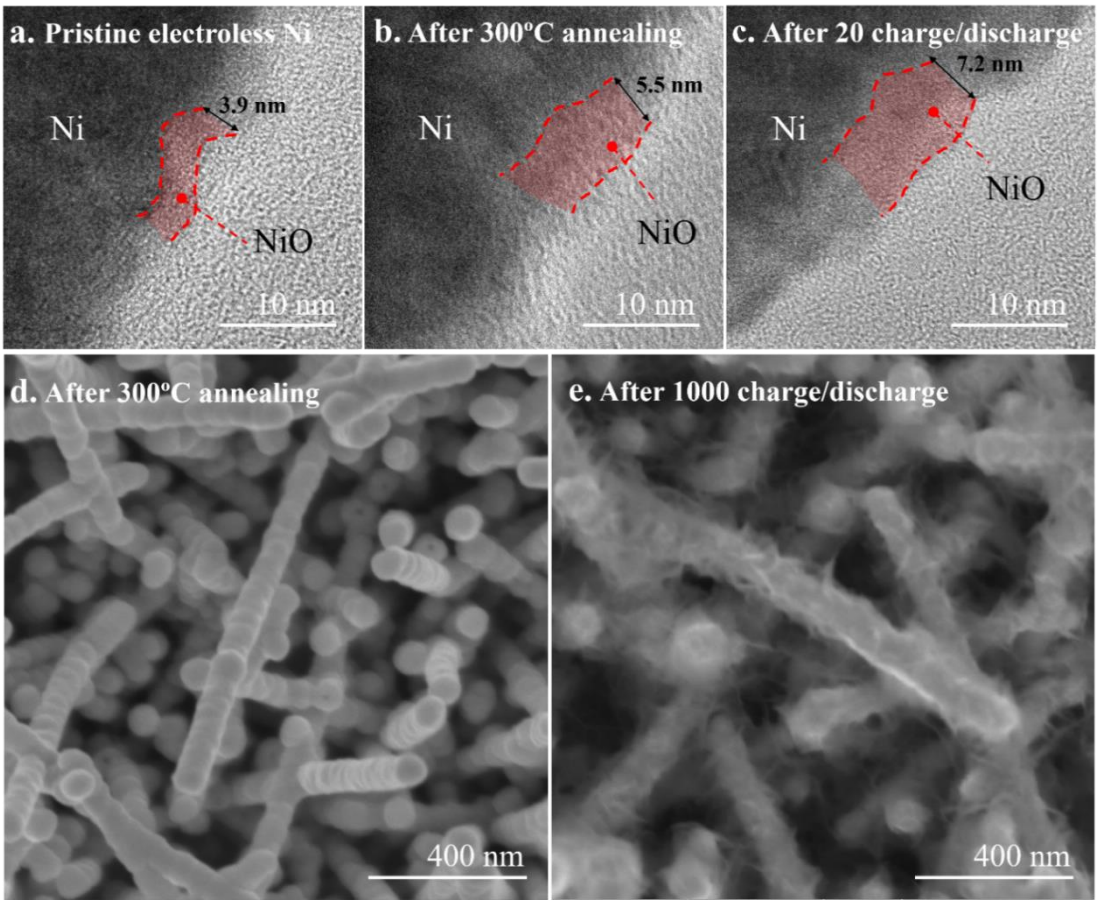

Figure 2-11. Electron microscopy images comparing TMV/Ni/NiO surfaces and structures after different steps in the experimental process. (top) TEM images comparing thickness of NiO layers at three different conditions: (a) pristine electroless Ni on TMV, (b) after 300 °C annealing of TMV/Ni, and (c) after 20 galvanostatic charge/discharge cycles of TMV/Ni/NiO at 2 mA cm^{-2}. (bottom) SEM images comparing TMV/Ni/NiO (d) before and (e) after 1000 galvanostatic charge/discharge cycles at 2 mA cm^{-2}.

To further understand the capacity increase phenomena, changes in both the NiO layer thickness and the nanostructure morphology during the initial cycles were

examined in electron microscopy images as shown in Figure 2-11. The TEM images shown in Figure 2-11a through 11c compare the electrode surfaces after different stages in the experimental process (Figure 2-11a: pristine electroless Ni, Figure 2-11b: after 300 °C annealing step, Figure 2-11c: after 20 charge/discharge cycles at 2 mA cm^{-2}). The thickness of the NiO layer was approximated by analyzing the apparent difference in TEM image contrast between metal (Ni) and dielectric (NiO) layers. Comparing the thickness of the red shadowed region between the dotted line boundaries, a significant increase in NiO thickness can be observed from pristine Ni (residual oxide) to the electrochemically cycled electrodes. This implies that there is an increase in active NiO content not only during the annealing process but also during the initial electrochemical cycling in KOH electrolyte. Specifically the Ni underneath the thermal NiO layer is being electrochemically oxidized during charging and participates in charge storage reactions in the subsequent cycles.[184,185] The SEM images shown in Figure 2-11d and 11e compares the nanostructure morphology of the TMV/Ni/NiO electrodes (Figure 2-11d) before and (Figure 2-11e) after a 1000 charge/discharge cycles. A significant change in surface morphology along with an increase in diameter of the nanorod electrodes are observed after the extended number of electrochemical cycling. The observations combined suggest two mechanisms involved in the material activation process during the initial cycling; 1) uniform growth of the NiO layer underneath the annealed oxide layer (Figure 2-11c), and 2) formation of a complex mesoscale structure within the NiO film (Figure 2-11e). Considering these observations in correlation with the non-linear capacity increase phenomena, it can be inferred that the suggested activation stages play a significant role increasing the charge capacity along the initial

cycle. The non-linear increase, reaching saturation level, is possibly due to the concurrent loss in nanostructure porosity by the expansion in diameter of nanorods.

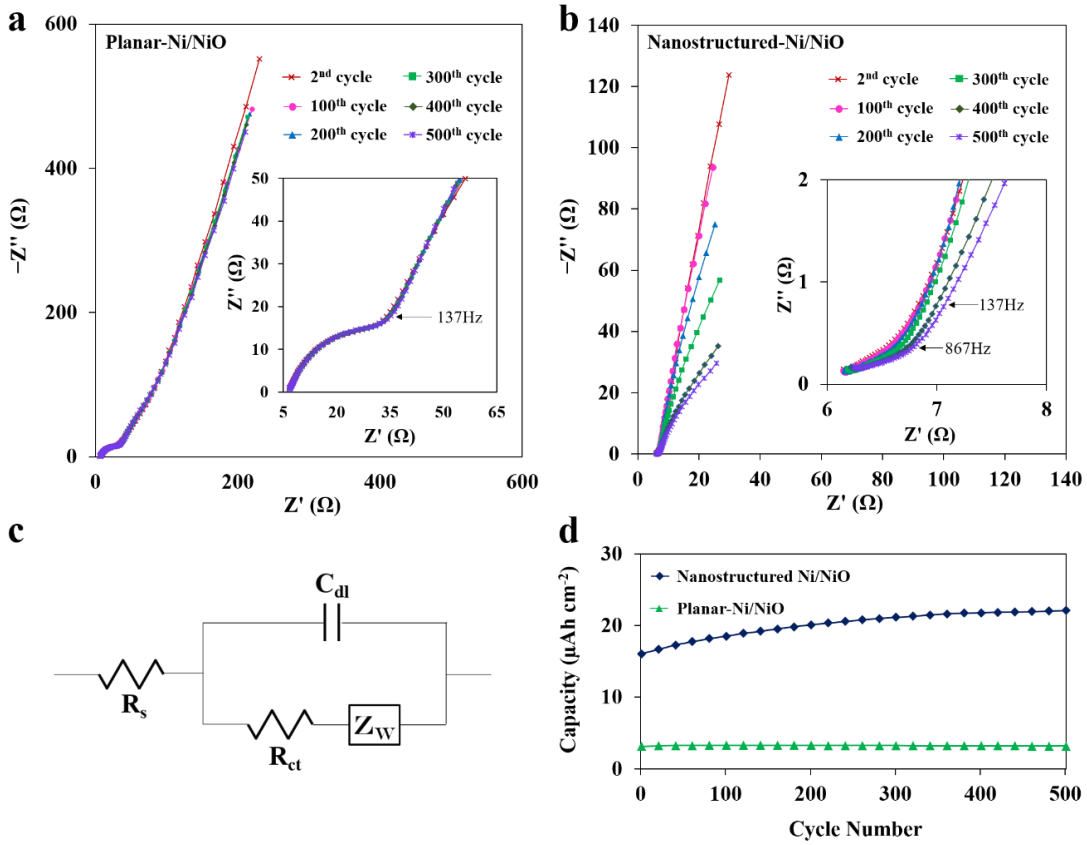

Figure 2-12. The Nyquist plots acquired from (a) planar-Ni/NiO and (b) nanostructured Ni/NiO during the first 500 galvanostatic charge/discharge at 2 mA cm^{-2}. (c) The Randles circuit diagram used for analysis of the Nyquist plots and (d) areal discharge capacity of the nanostructured- and planar-Ni/NiO electrodes over the first 500 cycles acquired along with the EIS measurements.

The EIS analysis (0.25 V working electrode potential vs. Ag/AgCl with 20 mV AC perturbation sweep from 1 Hz to 100 kHz) shown in Figure 2-12 also supports the idea of complex activation of NiO during the initial cycling. The Nyquist plots can be analyzed by looking at the two frequency regions where the plot generally displays semi-circular plot configuration at high frequencies reflecting a combination of the bulk electrolyte resistance (R_s), charge transfer resistance (R_{ct}), and double layer capacitance

(C_{dl}), while the straight line in the lower frequency region represents diffusion-governed electrochemical processes, interpreted by Warburg-impedance (Z_w). The Nyquist plot acquired from planar- and nanostructured-Ni/NiO electrodes are shown in Figure 2-12a and 12b, respectively. The charge transfer resistance of the planar-Ni/NiO is estimated to be ~35 Ω from the arc-shape in the high frequency region (> 137 Hz) using Randles-equivalent circuit (Figure 2-12c). Over the initial 500 cycles, there is no noticeable change in the plot configuration which is in good correspondence with the steady charge storage performance of the planar-Ni/NiO electrode (Figure 2-12d). However, the plot acquired from the nanostructured-Ni/NiO (Figure 2-12d) shows a significant change over the initial cycles. The overall impedance of the electrode is largely reduced compared to the planar-Ni/NiO attributed to the increase in active surface area by the TMV scaffolds. Also, the semi-circular plot configuration at the high frequency region (> 867 Hz), is significantly depressed/diminished showing almost a linear line in all consecutive measurements. This is an indication of low R_{ct} of the nanostructured-Ni/NiO better facilitating faradaic charge storage reactions.[186,187] More interestingly, the appearance of the arc-shape in the low-frequency linear lines (< 137 Hz) become distinctive along with the increase in cycle numbers − implying both the emergence of secondary charge transfer kinetics and reduction of the involved R_{ct} along with the activation phases of the NiO layer during the initial cycling.

These results combined strongly imply that the electrochemical formation of NiO (or $Ni(OH)_2$) content and an increase of the mesoscale active network ultimately cause the increase in active surface area resulting in enhanced charge storage performance. Also, the non-linear increase and saturation of the charge capacity

increase suggest that this electrochemically induced process is self-limited most likely due to limited charge diffusion and reduced electrical conductivity as a result of the active layer growth into the TMV/Ni-core. Combined results can provide further understanding of previous reports showing similar capacity increase phenomena in micro/nanostructured NiO electrodes for different ECS applications.[169,175,176,179]

The hierarchical-Ni/NiO electrodes were fabricated based on the TMV/Ni robust nanostructure platform integrated with Si-based μPAs. The uniform formation of thin NiO active layer is achieved by a simple thermal oxidation, and the formation of TMV/Ni (core)/NiO (shell) nanorod is confirmed by STEM and EELS analysis. Both the well-preserved nanostructural porosity of TMV/Ni after the annealing process and the successful integration of TMVs with Si microstructures allowed unprecedented charge capacity increase factors – ×10 with the nanostructured electrodes, and ×32.6 with the hierarchical electrodes compared to the planar ones – when compared with other TMV-templated ECS systems reported previously. Also, the analysis and discussions on the interesting charge capacity increase phenomena of the TMV/Ni/NiO electrodes should be applicable for understanding the electrochemical behavior and degradation mechanisms of other micro/nanostructured NiO electrodes investigated for ECS applications. This work greatly expands the potential applications of TMVs for next generation ECS devices with simple fabrication and excellent electrochemical cycle stability. If the uniform formation of other transition metal layers can be achieved over TMV surfaces, the annealing process can be further expanded for creating nano-core (metal)/shell (metal oxide) electrodes to benefit additional advanced ECS systems.

2.4. Chapter Summary

In this chapter, integration of TMV1cys particles with μPAs displaying different densities has been studied indicating critical dependence 3-D surface biomolecular functionalization on density/aspect ratio of the device structures. The surface pretreatment of the 3D electrodes with IPA have allowed uniform surface functionalization with TMV1cys on μPAs displaying SARs up to 5:1 - indicating that this method to, which increases the wettability of the 3D structured surface, is a route for enhanced biofunctionalization. The performance of TMV-μPA assembled hierarchical electrodes has been characterized in NiO-based ECS system demonstrating a significant increase in charge storage performance. Combined results indicate that development of methods to allow uniform functionalization of the biomacromolecules on surfaces of densely arranged 3D structures - overcoming the limitations of wettability - will allow biomaterial-based manufacturing methods for creating fully scalable micro/nano device components.

Chapter 3: Electrowetting-Assisted 3D Biofabrication

3.1. Wetting Properties of Micro-/Nano- Structured Materials

Considering biomolecules require storage in properly buffered liquid solutions to maintain their biological function, it is crucial to understand the wetting properties of device substrates for successful immobilization. Wetting is the ability of a liquid to maintain contact with a solid surface resulting from intermolecular interactions when both are brought together. This is a surface phenomenon at the molecular scale, and the level of wetting is determined by the surface tension γ balance formed at the intersection of three immiscible phases (e.g. $\gamma_{solid\text{-}liquid}$, $\gamma_{solid\text{-}gas}$, $\gamma_{liquid\text{-}gas}$). The balance of these three surface tensions at equilibrium is often characterized by measuring the contact angle θ_c of a sessile drop which translates into the wettability of the solid material. Figure 3-1 describes the relationship between the three surface tensions and the contact angle, and the Young equation (Eq. 3-1) provides a mathematical interpretation of the force balance between the surface tensions at thermal equilibrium.[188] The wettability of a material surface is defined by the measured contact angle with $\theta_c = 0$ º for complete wetting, $\theta_c < 5$ º for superhydrophilic surfaces, , 5 º $< \theta_c < 90$ º for hydrophilic surfaces, , 90 º $< \theta_c < 150$ º for hydrophobic surfaces, 150 º $< \theta_c < 180$ º for superhydrophobic surfaces, and $\theta_c = 180$ º for non-wetting. Wettability heavily relies on the surface energies between the interfacing immiscible phases and the roughness or microtextures of the solid substrate in contact with the liquid.[189] In particular, the superhydrophobic states with θ_c above 150 º are only achievable with rough or micro-textured surfaces which have received significant attention due to their extreme water-repelling and surface-cleaning capabilities.[190]

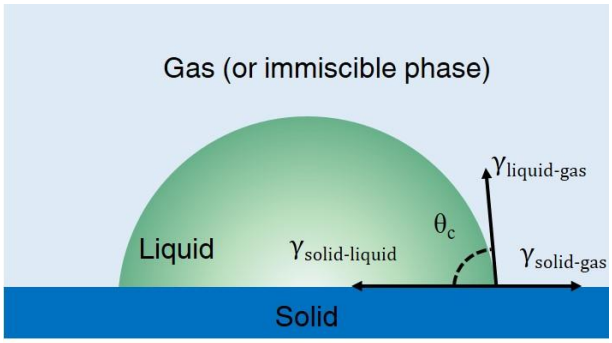

Figure 3-1. Contact angle (θ_c) formation of sessile drop on solid surface.

$$\gamma_{solid-gas} = \gamma_{solid-liquid} + \gamma_{liquid-gas} \cos\theta_c \qquad \text{(Eq. 3-1)}$$

Figure 3-2 shows two distinct wetting states of a μPA substrate - an exemplary microtextured substrate widely utilized for studying the effect of microtextures and roughness on wetting.[191] The wetting of liquid on rough/textured surfaces involves the balance between liquid penetration into the rough groove and entrapment of air bubbles inside the groove underneath the liquid. The basis for studying equilibrium wetting on rough surfaces was initially established by Wenzel,[192] Cassie, and Baxter.[193] The Wenzel equation (Eq. 3-2) models the homogeneous wetting regime (Figure 3-2a) and yields the Wenzel apparent contact angle θ_c^* in relation to the Young contact angle θ_c via the surface roughness ratio *r*. The surface roughness ratio is defined as the ratio of the true area of the solid surface to its nominal area. While this equation is applicable when dealing with a heterogeneous wetting regime (Figure 3-2b), the Wenzel model is not sufficient in understand the transitional wetting states. A more complex model was introduced by Cassie and Baxter (Figure 3-2b) as shown in Eq. 3-3 (Cassie-Baxter equation). They considered the heterogeneity of the surface material and wetting by dividing the surface roughness ratio *r* into r_f and *f*, which are the roughness ratio of the wet surface area, and the fraction of solid surface area wet by the liquid, respectively.

It should be noted here that the two equations (Eq. 3-1 and Eq. 3-2) become identical when $f = 1$ ($r_f = r$), and both equations are correct only if the liquid drop is sufficiently large compared with the typical roughness scale.[194]

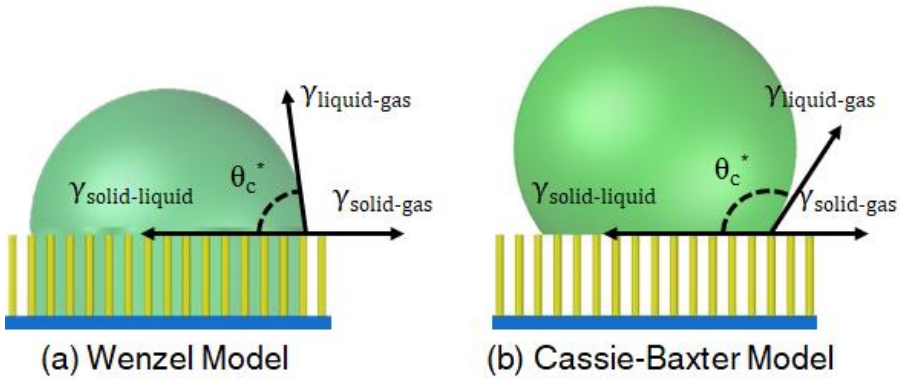

Figure 3-2. Wetting on μPAs. (a) Wenzel and (b) Cassie-Baxter Model.

$$\cos \theta_c^* = r \cdot \cos \theta_c \qquad \text{(Eq. 3-2)}$$

$$\cos \theta_c^* = r_f \cdot f \cdot \cos \theta_c + f - 1 \qquad \text{(Eq. 3-3)}$$

3.2. Electrowetting Technique for Droplet Manipulations

While the hydrophobic nature of densely and heterogeneously arranged microtextures has proven beneficial for certain applications (self-cleaning optical surfaces, water-repellent coatings, etc.),[195,196] these features become major obstacles for successful functionalization of biorecognition elements onto high surface area devices by limiting the introduction of biomolecules into deep microcavities. More significantly, structural hydrophobicity is even present when there is a hydrophilic surface chemistry (e.g. metals used for transducer electrodes)[197–200] and it becomes more challenging to induce a transition in wetting state (e.g. Wenzel state to Cassie-Baxter state) when the structures are designed with a higher density and aspect ratio.[201]

Different methods have been investigated for controlling transitions between the Cassie-Baxter and Wenzel states. For instance, Lafuma et al. have applied a pressure load onto a sessile drop of water sitting on a square lattice of triangular spikes (2 µm height and spacing) comprised of a complex UV-curable mixture of perfluoracrylates and non-fluorinated acrylates.[189] By using a plate to apply pressure onto the sessile drop, they were able to achieve ~20º shift in contact angle with an applied pressure of 200 Pa. The contact angle hysteresis measurement of ~100º (compared to 5º for original sessile drop) supported their argument that the wetting state had made the transition from Cassie-Baxter to Wenzel state. Another effort to induce increased structural wettability was achieved by Nakae et al. using a surfactant (sodium dodecyl sulfate (SDS)). SDS is a synthetic organic compound widely used in cleaning and hygiene products (detergent).[202] Mixing SDS with the liquid drop lowers the surface tension, allowing it to spread better on solid surfaces. While this enhanced structural wetting, the method is not compatible with biofabrication processes, as it will cause denaturation of the biomolecules.

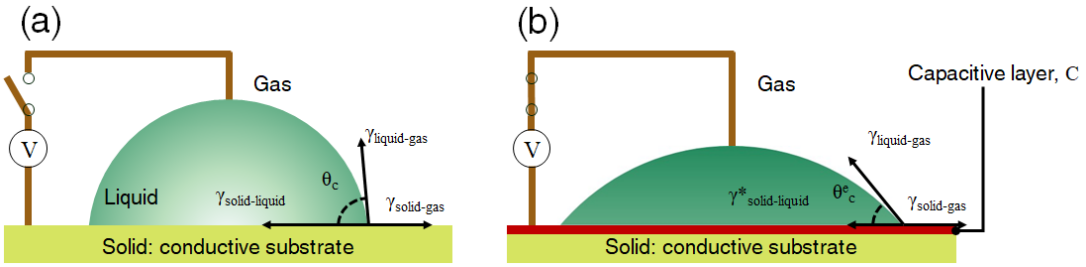

Figure 3-3. Electrowetting: (a) equilibrium and (b) steady-state droplet configurations.

One interesting method used for material wettability transitions is the use of electric potential to induce a transition in structural wettability, widely known as electrowetting.[39,203] Due to the high controllability over manipulation of a liquid droplet

on solid surfaces, it is utilized for a wide range of applications including liquid-based optical components,[204,205] display technologies,[206,207] LOC microfluidics (digital-microfluidics),[208,209] and, most relevant to this work, for micro/nano-textured surface wetting.[39,210,211] Figure 3-3 describes the electrowetting process on a homogeneous substrate. A liquid droplet with a typical size of 1 mm or less is placed on a conductive substrate, and the application of an electric potential V drives a reduction in solid-liquid surface tension $\gamma_{solid\text{-}liquid}$ inducing a decrease in contact angle and spreading the liquid over the surface. This is widely understood as a capacitive effect as described in Lippmann's derivation (Eq. 3-4), where $\gamma^*_{solid\text{-}liquid}$ is the effective surface tension at the solid-liquid interface under the applied voltage, and the capacitance $C = \varepsilon_0\varepsilon_r/d_H$ where ε_0 is permittivity of free space, and ε_r and d_H are each the permittivity and thickness of the double layer, respectively. The applied voltage *V* spontaneously builds an electric double layer at the solid-liquid interface consisting of charges on the metal surface and a cloud of oppositely charged counter-ions on the liquid side of the interface.

$$\gamma^*_{solid\text{-}liquid} = \gamma_{solid\text{-}liquid} - C \cdot V^2/2 \qquad \text{(Eq. 3-4)}$$

$$\cos\theta^e_c = \cos\theta_c + (C \cdot V^2)/(2 \cdot \gamma_{liquid\text{-}gas}) \qquad \text{(Eq. 3-5)}$$

Incorporating the effect of applied voltage into the Young equation (Eq. 3-1), the steady-state contact angle can be derived as shown in Eq. 3-5. The contact angle thus decreases rapidly upon the application of a voltage. It should be noted that the equation is only applicable within a voltage range below the onset of electrolytic processes.[203] Also, all thermodynamic derivations explaining electrowetting neglect the effect of gravity, considering that the Bond number ($B_0 = \sqrt{g\Delta\rho R^2/\gamma_{liquid-gas}}$) -

measuring the strength of gravity with respect to surface tension, g : gravity acceleration, $\Delta\rho$: density difference between the two phases (e.g. gas and liquid), R: characteristic length scale of the liquid geometry - is smaller than unity under ambient conditions.[203]

Table 3-1. Summary of experimental reports of electrowetting on 3-D micro/nano substrates.

Reference	3-D Substrates	Liquids	Applied Voltages	Contact Angle Transition
212	Hydrophobic film coated Si nanoposts	0.01 M cyclopantanol	22 V (DC)	~160 º to 110 º
211	Aligned CNT films on Cu	DI water, 0.03 M NaCl	50 V (DC) for water, 10 V (DC) for 0.03M NaCl	155 º to 98 º (DI water) 155 º to 50 º (NaCl)
213	Teflon-coated SU-8 microposts on Au-coated glass substrate	0.01 M KCl	130 V (DC)	152 º to 114 º
214	Parylene-coated CNT	DI water	80 V (DC)	109 º to ~95 º
210	C_4F_8-coated Si nanowires on SiO_2 substrate	100 mM KCl in both air and oil	150 V_{TRMS} (300 V_{pp} at 1 kHz)	164 º to 106 º (oil) 160 º to 137 º (air)
215	Teflon-coated ZnO nanorods on indium-tin-oxide (ITO) substrate	DI water, 0.3 M NaCl	40 V (DC)	170 º to 151 º (DI water) 155 º to 77 º (NaCl)
216	Amorphous carbon nanoparticles capped CNT on Si substrate	DI water, 0.1M NaCl	43 V (DC) for DI water 15 V (DC) for 0.1M NaCl	~170 º to ~104 º for both liquids
217	C_4F_8-coated Si nanopillar arrays	Glycerol + NH_4Cl + DI water	21 V (DC)	170 º to ~110 º

In applying these electrowetting principles, a number of researchers have accomplished demonstrations of wettability transitions in 3-D structured materials including Si nanoposts, epoxy microposts, and carbon nanotubes (CNT), as summarized in Table 3-1. Evidently, all examples feature hydrophobic surface chemistry (e.g. fluorocarbon coating, CNT), and the addition of the micro/nano structures leads to superhydrophobicity. Due to the implementation of hydrophobic material coatings (insulating dielectrics) or the limited conductivity of CNT nanowires,

most of the work required using voltages above the electrolytic reaction boundary to induce a sufficient wettability transition. While lower voltages are expected to function on exposed conductive substrates, applying electrowetting for biofabrication demands careful consideration of the effect of applied voltage levels to the integrity of biomolecules to validate electrowetting biocompatibility. Additionally, the effectiveness of AC voltage signal demonstrated by Verplanck et al.[210] is promising for biofabrication as it might help to significantly reduce the electrolytic reaction upon wetting of solution into micro/nanocavities.

3.3. Surface Wettability Characterization of the Micropillar Arrays

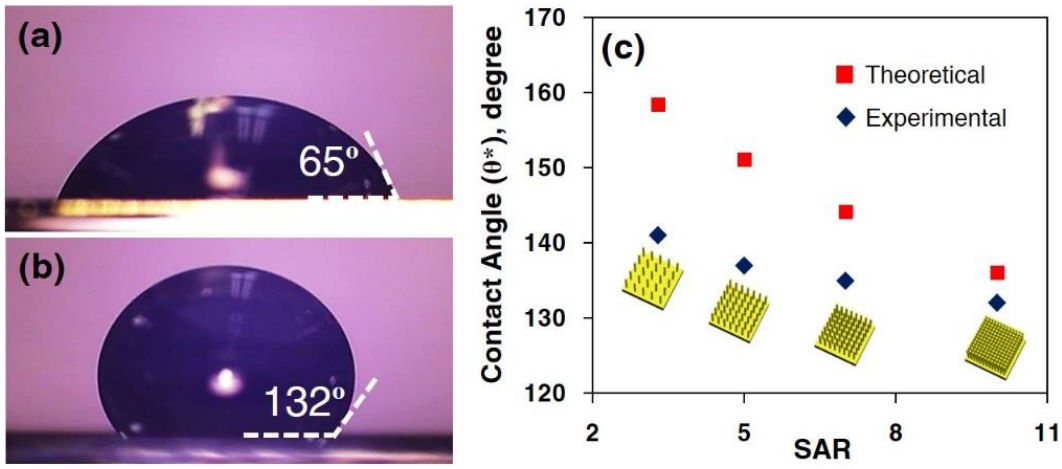

Figure 3-4. Comparison of apparent contact angle measurements of 10 µl sessile drops of TMV1cys solution (0.2 mg/ml in 0.1 M PB solution) on Au-coated (a) planar and (b) µPA (SAR=10) electrodes. (c) The experimentally measured contact angles (θ*) follow theoretically expected trend while there is increasing disparity with lower SARs.

As an initial step, the structurally hydrophobic properties of Au-coated µPAs are characterized via contact angle measurements of 10 µl sessile drops of the TMV1cys solution on Au-coated planar (Figure 3-4a) and µPA electrodes (Figure 3-4b). While the planar Au surface exhibits a hydrophilic nature with a 65° contact angle, the µPAs yield more hydrophobic characteristics as indicated by a 132° contact angle

(Cassie-Baxter state). This is close to the theoretically expected value (136º), calculated based on the Cassie-Baxter equation (Eq. 3-6), where θ* is the apparent contact angle on the μPAs, ϕ_s is the fraction of the solid in contact with the TMV1cys solution, and θ_0 is the contact angle on the planar Au substrate.[39]

$$\cos \theta^* = -1 + \phi_s (1 + \cos \theta_0) \quad (3\text{-}6)$$

Figure 3-4c plots both theoretically expected (derived from Cassie-Baxter equation (Eq. 3-6) with θ_0=65º, and ϕ_s calculated from the pillar geometry) and experimentally acquired contact angles (θ*) indicating that the hydrophobicity of the μPAs decreases with an increase in SAR. The disparity between the two can be attributed to the gentle pressure applied when loading the droplet onto the μPAs via syringe tips and hydrophilic surface (Au) inducing liquid pinning onto the pillar tips.[218] Such a wetting state is only valid when there is no external disruption force due to the hydrophilicity of the Au surface. Once the Cassie-Baxter state is disrupted with an external force (e.g. mass loading), a faster transition of the wetting state – indicated by the droplet spreading into the cavities (transitioning to the *Wenzel* state) – is observed with the lower SAR μPAs. It becomes a significant challenge to introduce the solution into narrower cavities (SAR ≥ 7) that do not easily transition to a Wenzel state, attributed to less pressure loading per each spacing segment. In other words, the wider spacing reduces ϕ_s which as a result increases the fraction of the liquid droplet that is supported by the micropillars.[38,218] The TMV1cys droplets on such high SAR μPAs are readilly movable with no traceable liquids remaining on the electrode surface.

3.4. Application of Electrowetting for 3D Biomaterial-Device Integration

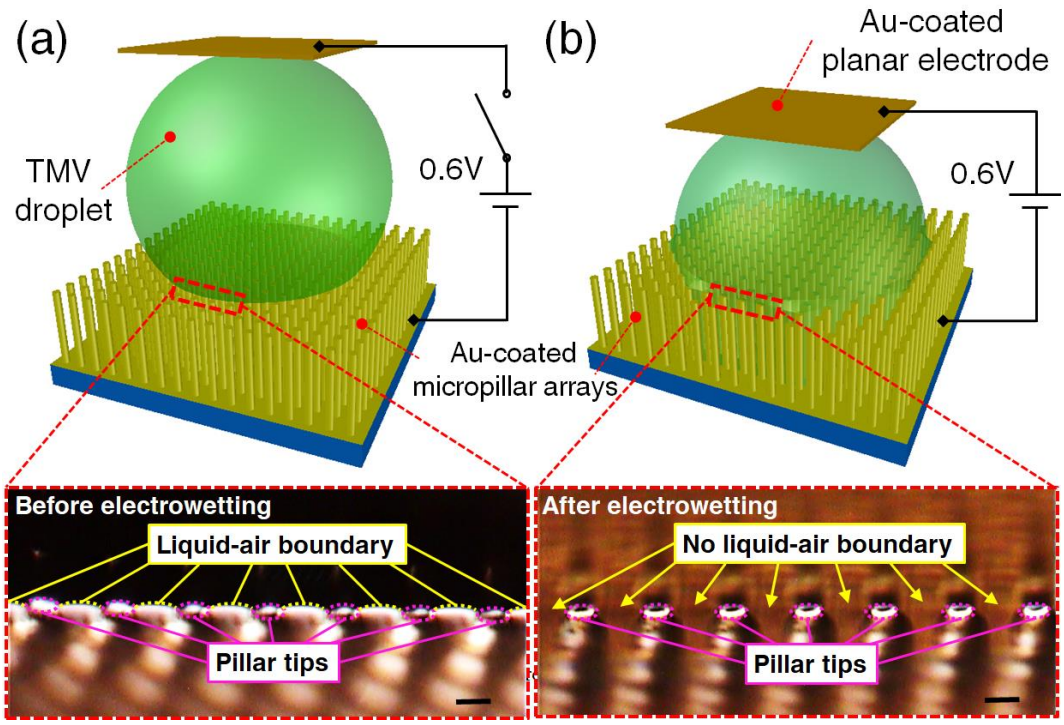

Figure 3-5. Schematics of the TMV droplet on μPAs (top) with optical microscopy from the top of the μPAs interfacing with droplet edges (bottom). The (a) Casie-Baxter state and (b) the Wenzel state of the droplet is clearly observed in the microscopy images (focusing at edge-on pillar tips) taken before and after electrowetting, respectively (scale bars: 10μm).

Figure 3-5 describes the initial effort to demonstrate the effectiveness of electrowetting for introducing TMV solution into the micropillar cavities. A 10 μl droplet of TMV solution was located on top of the μPAs and a planar electrode was placed on top sandwiching the droplet in between the two electrodes. A 3-D printed structural component was used to separate the two electrodes with 1 mm spacing, and a DC power supply (Agilent E3681A) was connected to supply electrowetting voltage. While it was difficult to monitor the wetting process due to the top electrode blocking the light, it was identified that applying a DC 0.6 V for 1 minute would induce sufficient wetting to allow complete immobilization of TMVs onto 7:1 SAR μPAs. The optical

microscope images in Figure 3-5 are taken from the wetting edges of μPAs – focused at pillar tips – before and after the electrowetting. Before applying the voltage, the clear surface tension boundary is observed at the pillar tips, indicating the liquid is in the Cassie-Baxter state with the surface in an upward arc shape of liquid surface due to the hydrophilic surface chemistry. After electrowetting, the boundary at the tip disappeared indicating the liquid was introduced into the microcavities.

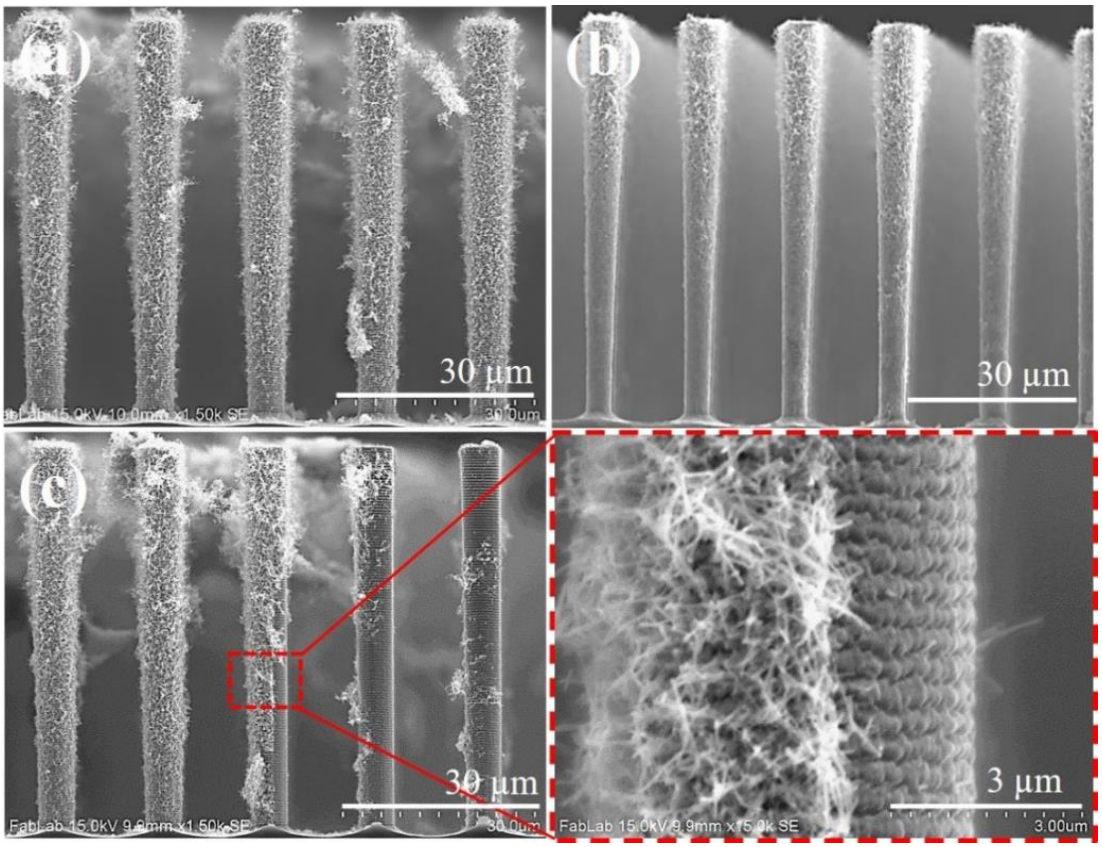

Figure 3-6. Cross-sectional SEM images of the nanostructured TMVs on the μPAs (7:1 SAR). (a) Electrowetting allowed near-complete TMV coverage along the deep sidewalls compared to the (b) result using the traditional method. (c) The clear functionalization boundary is observed at the wetting edge demonstrating the discrete nature of the method.

This was further characterized via cross-sectional SEM as shown in Figure 3-6. A complete and uniform coverage of TMVs on pillar side walls is achieved at the center of the μPAs (Figure 3-6a), a significant improvement over the traditional method

(Figure 3-6b) and the IPA treatment method. More interestingly, a clear immobilization boundary was observed on a single pillar sidewall located at the wetting edge (Figure 3-6c). This indicated that the wetting of the 3-D structure can be locally controlled utilizing the surface tension created by the densely arranged pillar surfaces as a control parameter for lateral spreading of the liquid.

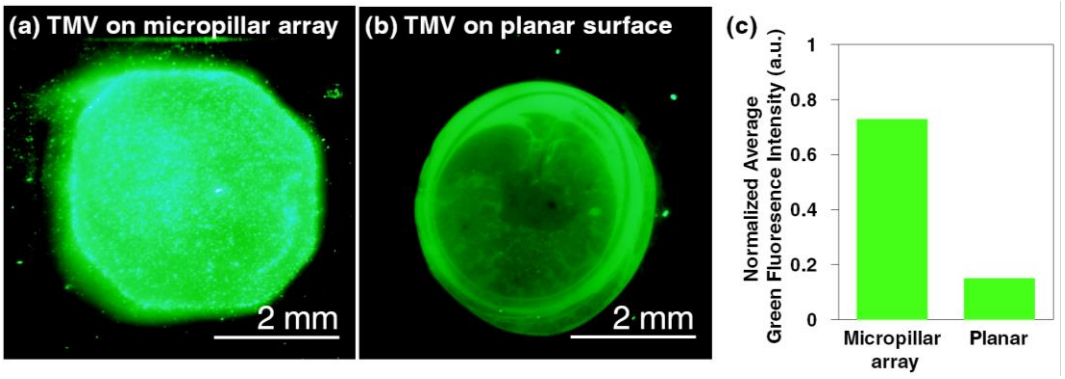

Figure 3-7. Fluorescent microscopy from (a) electrowetted TMVs on μPAs (SAR 7:1), and (b) non-electrowetted TMVs on planar Au substrate. (c) Comparison of normalized average green fluorescence intensity between (a) and (b).

The biochemical activity and increased immobilization density was characterized using a fluorescent labeling agent (fluorescein-5-maleimide) targeting thiols on TMV surface. Fluorescent microscope settings were identical for both images (e.g. magnification, exposure time, etc.). As shown in Figure 3-7, the electrowetting-processed TMVs retained excellent biochemical activity. The 5-fold increase in fluorescence intensity compared to the TMVs on planar Au substrates directly indicates the increased biochemical reactivity/density due to the underlying μPAs (SAR 7:1). This increase factor measures slightly below the theoretically expected value of 6.3 (refer to Figure 2-1c). Potential reasons for this result are 1) wider focal depth for the 3D structure compared to the planar substrate, and 2) possible emission losses within

the volume of the μPAs. While this initial effort has demonstrated the effectiveness of the electrowetting, a rigorous modification in the experimental configuration was necessary to allow both 1) characterization of the electrowetting process and 2) better utilization of the localized functionalization to be able to pattern the hierarchical arrangement of TMV particles onto a single μPA substrate for arrayed or multiplexed bioelectronics applications.

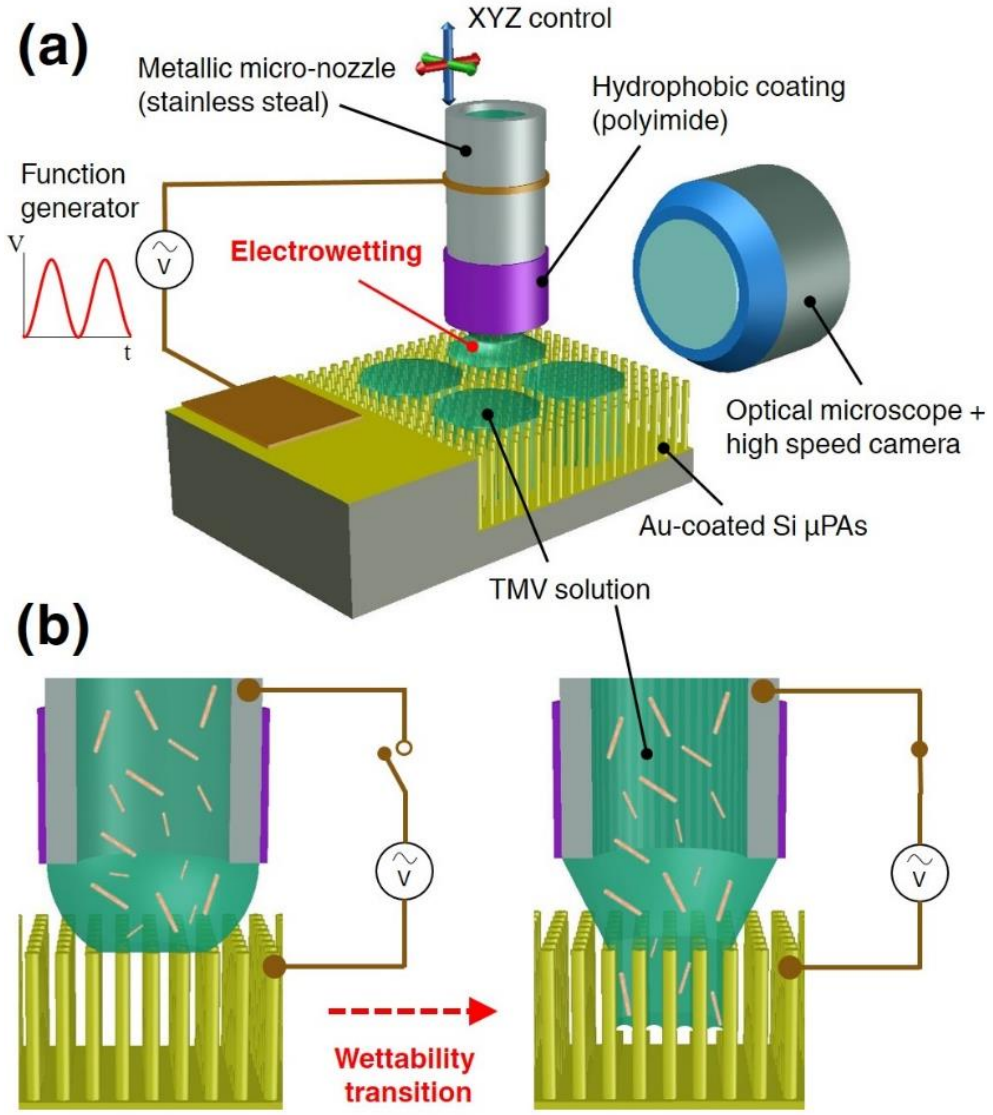

Figure 3-8. (a) An overview of the custom-built system for 3-D electro-bioprinting (3D-EBP) , and (b) cross-sectional schematics describing the electrowetting-induced structural wettability transition; introducing TMV1cys into the deep microcavities.

A custom-built set up was developed to characterize and implement 3-D electro-bioprinting (3-D EBP) of TMV1cys solutions onto high-density (SAR 10:1) μPA electrodes. Figure 3-8a illustrates an overview of the developed system comprising six major elements: 1) TMV1cys solution, 2) Au-coated Si μPA electrode, 3) stainless-steel nozzle with its tip coated with a hydrophobic film (polyimide), 4) AC function generator (Agilent 33220A), 5) XYZ micromanipulator (Velmex modules), and 6) optical microscope with high-speed image capture capability (Redlake MotionPro HS-3). The electrowetting process is conducted in air at room temperature. The TMV1cys solution functions as a "biological ink" to functionalize and pattern the μPAs. As mentioned before, the TMV1cys used in this work is genetically modified with cysteines, which contain thiol groups (-SH), on their surfaces. This allows TMV1cys macromolecules to self-assemble onto Au surfaces through Au-thiol binding, and achieve uniform metallization over their nanoscale structure through electroless plating.[114] This is critical for the successful demonstration of this approach, allowing characterization of functionalization morphology and biochemical activity after the electrowetting process via SEM and fluorescent labeling. The μPA electrode serves as a 3-D substrate in the system. The hydrophobicity provides physical control over the wetting and patterning process by limiting the substrate wetting at thermal equilibrium. The Au layer coated over the Si pillar structure functions as the electrode for the electrowetting process, as well as a means for the functionalization of TMV1cys through the Au-thiol binding mechanism. Considering the hydrophobicity of the substrate, it is challenging to accurately position the TMV1cys solution on the μPAs, and even more problematic when the volume of the solution is in the micro-liter range.

This is overcome by the use of a modified metallic nozzle and the XYZ micromanipulator positioned over the substrate. Specifically, the hydrophobic film (polyimide) coating around the outer surface of the metallic nozzle enables formation of a semi-spherical hanging drop of the biological solution. This key modification enhances control over the amount of solution dispensed during each electrowetting step (~1 µl/electrowetting). Without the coating, the dispensed liquid would immediately roll upward to the outer metallic surface, hence preventing control over the size and amount of the solution used for the electrowetting step.

The cross-section of the electrowetting step is depicted in Figure 3-8b. As shown in the left figure, the TMV1cys solution at the nozzle adopts the Cassie-Baxter state when it is loaded onto the µPAs. When the voltage is applied, an instant transition in surface wettability is induced, driving the TMV1cys solution into the microcavities transitioning to the Wenzel state.[39] This allows uniform self-assemby/functionalization of TMV1cys onto the surfaces of the deep microstructures. In order to apply the electrowetting voltage at the solid-liquid interface formed at the tip of the pillars, an AC function generator is directly connected to the µPAs and the stainless-steel part of the nozzle. Using the horizontally positioned microscope, the dynamics of the electrowetting are characterized by monitoring the apparent contact angle for a range of applied voltage levels. The frequency of the applied voltage was kept at 10 kHz to avoid bubble generation from electrolysis of water (as this was observed when working with DC voltages in the preliminary experiments discussed above).

For these experiments µPAs featuring an SAR of 10:1 were used to control structural hydrophobicity for electrowetting and to achieve high-density TMV1cys

immobilization per device footprint. First, the electrowetting voltage is characterized by monitoring the change in droplet configuration (TMV1cys solution) upon wetting and measuring the steady-state contact angle at different applied voltages. Figure 3-9 compares the steady-state contact angles of TMV1cys droplets on planar Au (Figure 3-9a) and Au-coated µPA substrates (Figure 3-9b). The applied AC voltages are varied from 0 to 1.2 V_{RMS} featuring 0 minimum level with peak-to-peak amplitude varying from 0 to 2 V_{PP} at 10 kHz, and the steady-state contact angles are measured 3 seconds after surface impingement (no noticeable spreading is observed at this time point). As expected, the droplet on a planar Au substrate shows hydrophilic contact angles for all applied voltage levels with slightly lower measures at increased voltages. However, a droplet impinging onto the µPA substrate shows a slower and more gradual decrease in contact angle as the voltage is increased, demonstrating the higher dependancy of its wettability to the electrowetting voltage compared to its planar counter part.

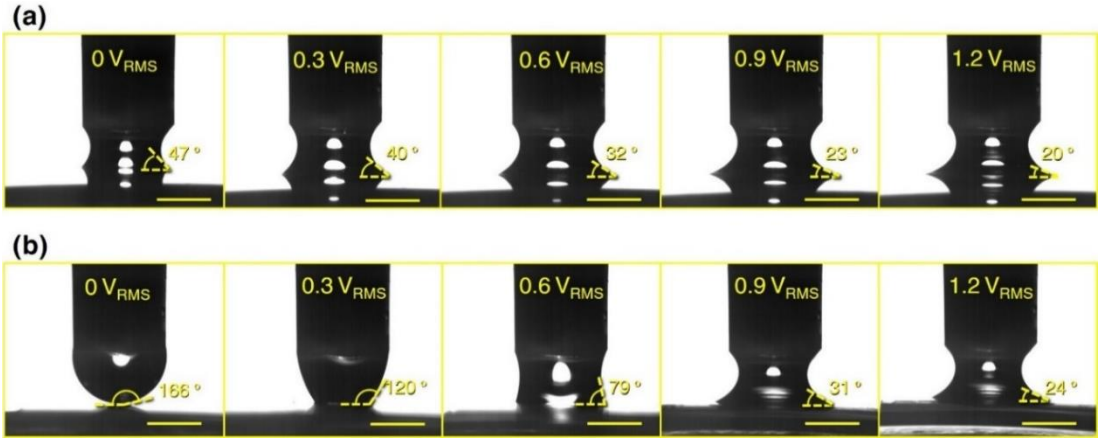

Figure 3-9. Comparisons of steady-state contact angles on Au-coated (a) planar and (b) µPA (SAR=10) electrodes (scale bars: 1 mm). Images were taken 3 seconds after applying the specified electrowetting voltages.

Figure 3-10 shows the change in contact angles monitored over time, until it reached steady-state, to characterize the electrowetting dynamics. As shown, there is

an abrupt change in contact angle of the liquid drops impinged onto a planar surface, reaching the steady-state contact angle within a second (Figure 3-10a). The steady-state angles line up with very small differences corresponding to the level of applied voltage (the 180º is plotted to indicate the abrupt change – it is the tangent angle for the hemispherical droplet right before impingement). Figure 3-10b plots the change in contact angles on the μPAs. The primary observation is that the higher voltage induced a faster change in contact angle due to the increased applied capacitive energy at the solid-liquid interface (Eq. 3-5). In addition, the electrowetting on μPAs shows three distict dynamic regions over time. First, an abrupt change in contact angle is induced upon the application of voltage due to an instant reduction of the surface tension at the solid-liquid interface. However, this is not as abrupt as observed on the planar surface as the radial spreading is hindered by the surface tentions formed at the pillar side wall-liquid interfaces. As a result, a semi-linear region (indicated by the straight dotted lines on the graphs) is followed where the wetting boundary spreads gradually in the radial direactions as the liquid reaches the bottom surface. Ultimately, this transitions into a saturated region as the contact angle approaches a steady state, in which the wetting does not involve a change in contact angle; the spreading of liquid in radial direction continues within the microcavities based on visual observation, attributed to capillary pressure.[203] Overall, this characterization confirms that the wetting within 3-D structures can be controlled by adjusting the voltage amplitude and duration of electrowetting, thereby demonstrating the capability to control the biofunctionalization of 3-D substrates.

The electrowetting voltage 1.2 V_{RMS} at 10 kHz was identified as optimal for TMV1cys solution wetting, as determined from the steady-state contact angle measured from the planar Au and the µPA substrates in Figure 3-10c. Basically, the voltage level that reached a similar contact angle between the two substrates was chosen, as this is considered to be an indicative of complete wetting. Lower electrowetting voltage levels (<1.2 V_{RMS}) would leave exposed pillar surfaces at the bottom of the microcavities (similar to those shown in Figure 2-4). Also, the AC voltage signal significantly helped minimize electrolysis, and therefore bubble generations during electrowetting; when observed with the microscope, there was no observable bubble generation with the AC voltage, while a DC 1.2 V created noticeable bubbles on the electrode surfaces and within the TMV1cys droplet during the electrowetting process, which can hinder successful biofunctionalization.

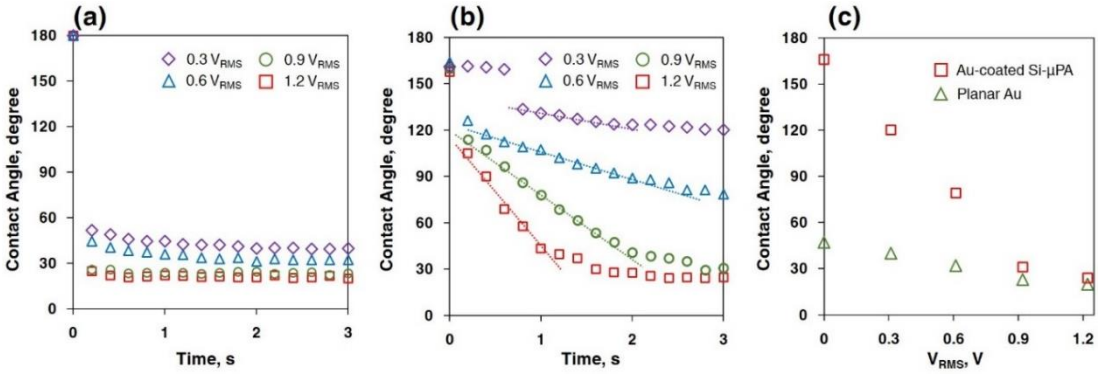

Figure 3-10. Comparisons of change in contact angle over time at different electrowetting voltages on Au-coated (a) planar and (b) µPA (SAR=10) electrodes. (c) The comparison of steady-state contact angles measured from planar and µPA electrodes indicate 1.2 V_{RMS} as the complete wetting voltage.

The morphology of electrowetting-processed TMV1cys on µPAs was characterized using SEM after electroless Ni metalization. The cross-sectional images confirm complete and uniform TMV1cys nanotexturing of the µPAs (Figure 3-11a). Compared to the previous method using complete immersion of the substrates into a 1

ml TMV1cys solution bath (Figure 2-4e), this is a significant improvement considering the excellent uniformity of the TMV1cys coating at the lower portions of the μPA surfaces. Figure 3-11b shows the μPAs that are exposed to a TMV1cys droplet without electrowetting. Isolated TMV1cys macromolecules coated with Ni are only observed at the top surfaces of the pillars while most of the micropillar surfaces remain uncovered. This indicates that the Cassie-Baxter state of the droplet is stable throughout the overnight self-assembly process and raises the significance of the electrowetting-assisted process as an enabling technology. Figure 3-11c shows the μPAs located at the wetting edge. Similar to the results obtained from our initial approach, and corresponding with the optical microscope image shown in Figure 3-12 (taken from the wetting edge), a clear functionalization boundary is formed on the sidewall of micropillars located along the wetting edge. The initial limitation from the structural hydrophobicity plays a critical role in locally confining TMV1cys functionalization on the 3-D substrate by limiting lateral spreading of liquid with reduced radial capillary pressure. This is a result of the increased sum of solid-liquid surface tensions owing to the densely arranged vertical pillar sidewalls. Additional top-down SEM images (Figure 3-11d) showing the tops of TMV1cys assembled micropillars further demonstrates the beneficial utility of electrowetting principles for creating uniformly biofunctionalized hierarchical device components.

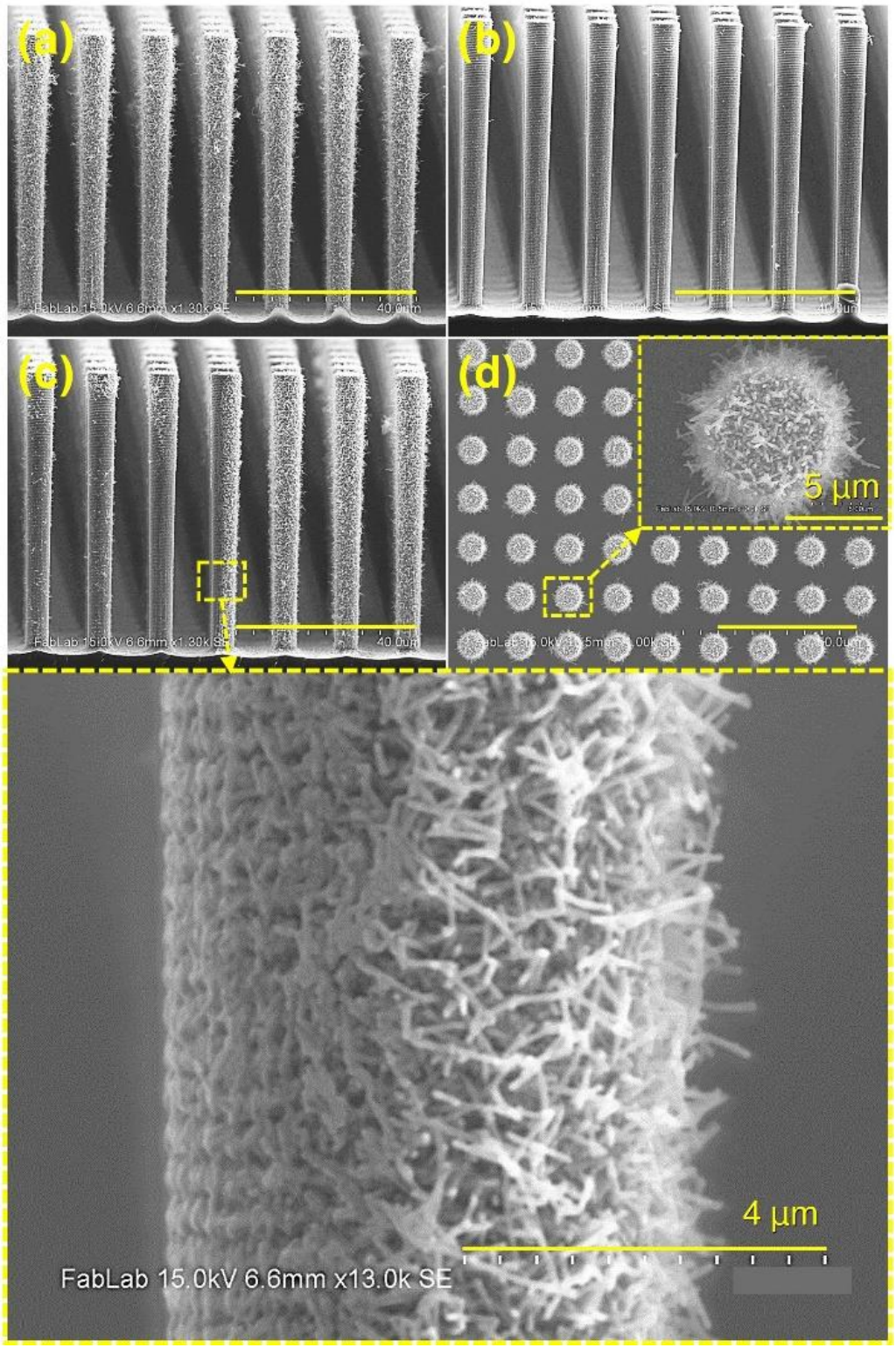

Figure 3-11. SEM images of µPA electrodes (SAR=10) with Ni-coated TMV1cys nanostructures (scale bars: 40 µm unless specified). (a) The electrowetting allowed a complete TMV1cys coverage along the deep micropillar side-walls compared to the (b) non-electrowetted µPAs. (c) A clear functionalization boundary formed along a single pillar surface at the wetting edge. (d) Top-down view of the µPAs showing a uniform TMV1cys coverage across the electrowetting processed µPAs.

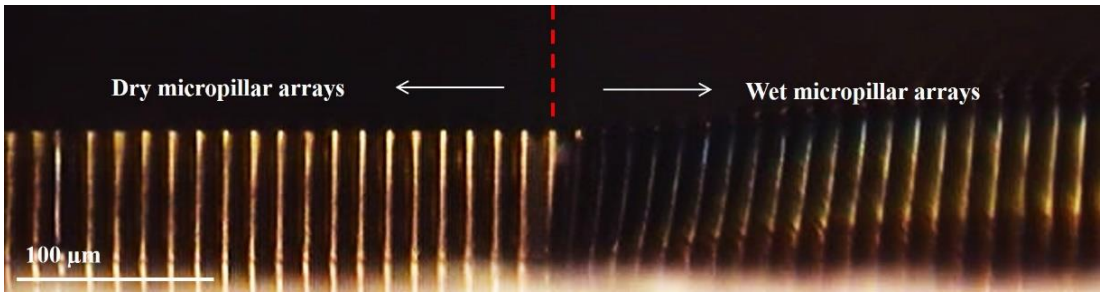

Figure 3-12. A clear wetting boundary observed in a magnified cross-sectional view of the micropillar arras.

As a final characterization, the biochemical activity of TMV1cys assembled by electrowetting was evaluated via the fluorescent labeling as introduced in the earlier section. . Figure 3-13a and 13b compares the fluorescence emitted by labeled TMV1cys macromolecules on planar Au and µPA substrates, respectively. A significant increase in the fluorescence intensity, similar to the case with applying DC voltage discussed above, is achieved with the hierarchically arranged TMV1cys on the µPAs, attributed to the increased nanoreceptor density within the functionalization area. Specifically, the image analysis indicated a ~7-fold increase in intensity (Figure 3-13c), a significant enhancement enabled by successful TMV1cys integration with the high-density microstructures. Similar to the results show in Figure 3-7, the enhancement factor achieved is slightly less than the theoretically expected value of 8.9 (derived based on the µPA geometry, Figure 2-1c) due to the aforementioned potential reasons. Furthermore, in efforts to demonstrate the patterning capability of the developed biofabrication system (Figure 3-8a), 3×3 hierarchical TMV1cys arrays on 7×7 mm^2 µPA substrates were fabricated (Figure 3-13d). As indicated by the error bars in Figure 3-13c, the TMV1cys arrays fabricated through the electrowetting process show excellent uniformity in biochemical activity. Combined results demonstrate the

advantages of the electrowetting-assisted 3-D biofabrication technology for building multiplexed and high-throughput bio/chemical sensing/analysis platforms.

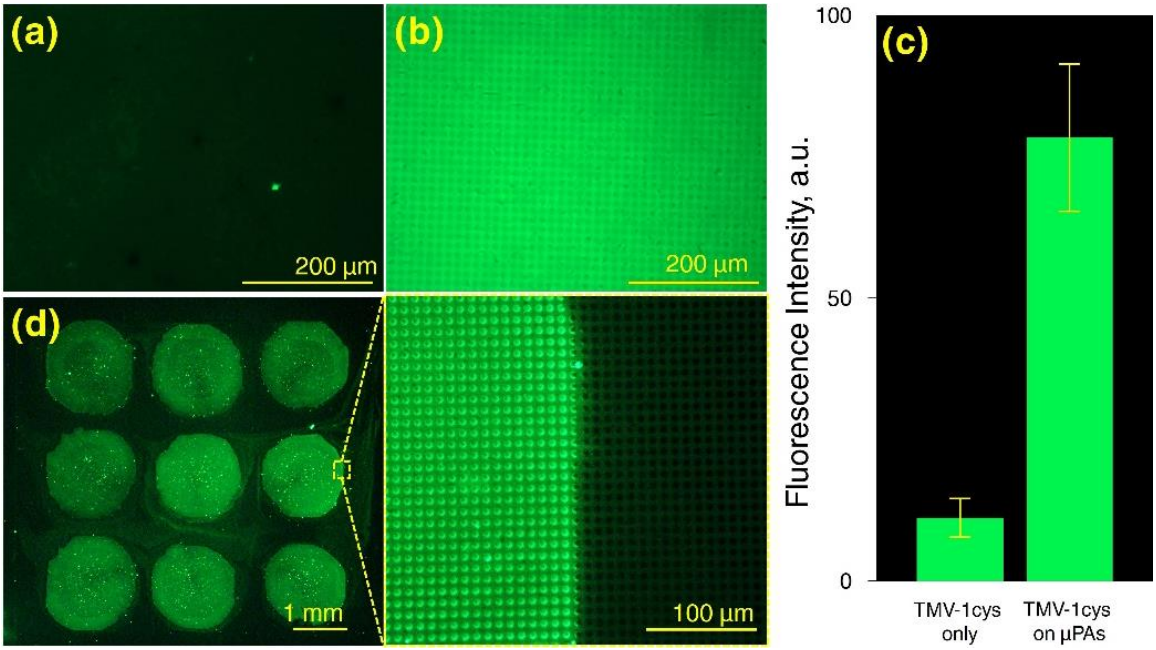

Figure 3-13. Fluorescent microscopy characterization confirming biochemical activity of TMV1cys after electrowetting. Comparing TMV1cys on (a) planar and (b) µPAs, (c) a 7-fold increase in fluorescence intensity is achieved (n=9) with excellent functionalization uniformity and pattern fidelity across the (d) 3×3 arrays of hierarchical bionanoreceptors.

3.5. Development of Automated and Programmable 3D Biofabrication Technology

The 3D-EBP developed in the above section has been integrated with a state-of-the-art commercial 3D bioprinter (3D-Bioplotter, Envision TEC) by simply connecting a function generator (Agilent 33220A) to the printing nozzle and the substrate as described in Figure 3-14. The built-in graphical user interface allowed highly automated and programmable 3D-EBP with precise control over nozzle pressure, printing distance, array size/density, and solution temperature. As the 3D-Bioplotter is mainly designed for printing materials carried in hydrogels (e.g. gelatin, alginate, corn starch, etc.), the controllable pressure and time ranges for ink extrusion at the nozzle

are optimal for higher viscosity fluids compared to the buffer solution used in this work. Through multiple iterations at the lowest extrusion time and pressure ranges, the optimal process parameters have been determined as 0.3 second extrusion at 0.1 bar with a 100 μm distance from the nozzle to the substrate. It should be noted here that these parameters strongly depends on the nozzle size and the viscosity of the ink solution.

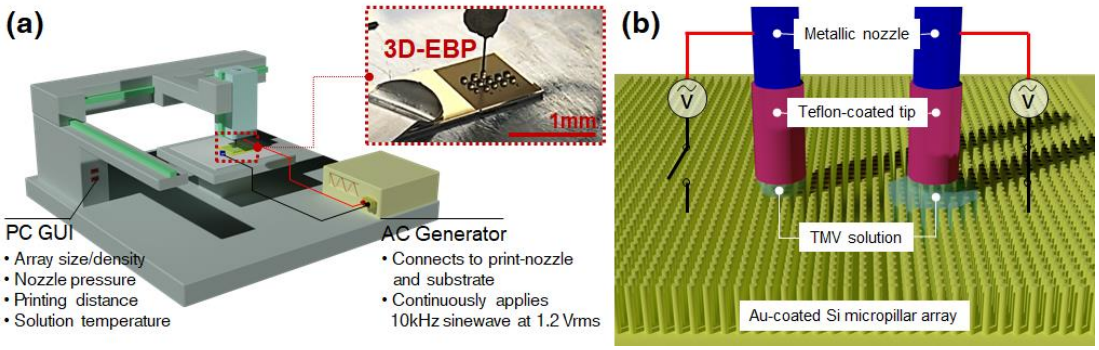

Figure 3-14. (a) Overview of the programmable 3D-bioprinting system integrating 3D-EBP with a commercial bioprinter. (b) Illustration of TMV solution impinging onto the μPA from teflon-modified needles. The solution impinging onto the μPA surface without electrowetting (left) keeps a spherical shape without further access/spreading into the microcavities (Cassie-Baxter state), while the droplet impinging with electrowetting (right) selectively wets the underlying cavities (Wenzel state).

In this initial demonstration, a 32-gauge stainless steel needle (inner diameter: 100 μm, outer diameter: 260 μm) was utilized with a hydrophobic modification at the; the tip was dipped into Teflon solution (Teflon^{TM} AF 400S1) and cured at 180°C for 3mins. A syringe was connected during the curing step to continuously flow air through the tip preventing blockage during the curing process. As aforementioned, the hydrophobic coating at the tip was critical to isolate the droplet forming towards the substrate during extrusion (Figure 3-14b). Compared to the previous modification using polyimide tape, the dip-coating based modification with Teflon solution resulted in a very thin film thickness (~1 μm). This was significantly beneficial for reducing the

droplet size hanging downward at the tip before impinging onto the substrate. The electrowetting voltage was continuously applied during the printing process by seamlessly integrating the function generator to the metallic -nozzle and -printing bed without hindering the printing operation. Based on the characterization results discussed in section 3.4, a sinusoidal voltage signal of 1.2 V_{rms} at 10 kHz was applied to induce uniform and localized wetting of the TMV1cys ink into the µPAs. All processes were conducted at room temperature with ambient humidity. Both the print-bed and the bio-ink cartridges were kept at 10°C to extend the stability of TMV1cys particles throughout multiple printing processes. The bio-printed electrodes were incubated overnight in a humid chamber for self-assembly of TMV1cys particles onto the electrode surface through thiol-Au binding.[114]

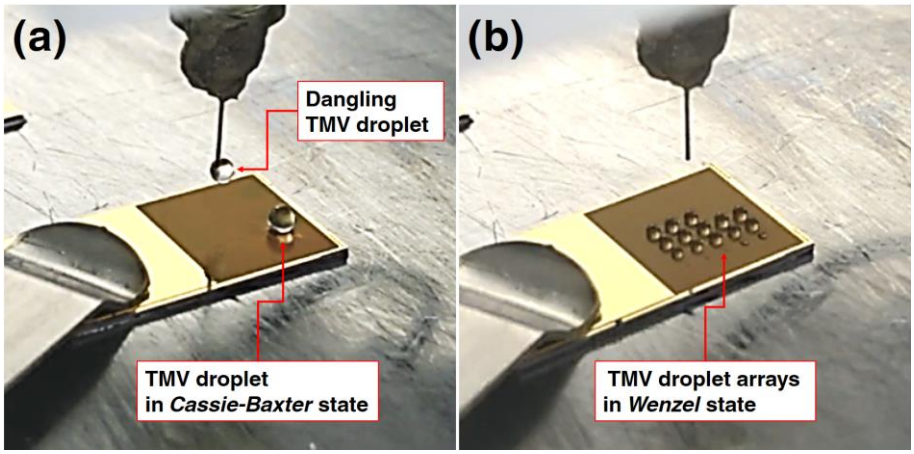

Figure 3-15. Optical images comparing the TMV1cys solution droplets on µPA electrodes (SAR 10:1). (a) No electrowetting: hydrophobic nature of the µPA electrodes limits the droplet printing onto the µPA surface resulting in a failure in printing process. (b) Electrowetting: continuous application of electrowetting voltage during the printing process allows successful patterning of uniform droplet volumes on the µPA electrodes.

Figure 3-15 compares the printing processes on µPA electrodes (SAR: 10) under two different conditions emphasizing electrowetting as an enabling method. When the printing process is conducted without applying the electrowetting voltage

(Figure 3-15a), the extruded droplets at the printing nozzle do not settle onto the μPA surface, and instead accumulate at the nozzle until falling onto the surface due to gravity (the droplets loaded onto the μPA surface do not penetrate into the cavity). However, with the application of the electrowetting technique (Figure 3-15b), the 3D-EBP allowed consistent dispensing of ~1 uL of the bio-ink (0.2 mg/mL TMV1cys solution in 0.1M phosphate buffer solution) onto the μPA electrodes throughout the programmed array patterns by successfully introducing the bio-ink into the designated micro-cavities. The spacing between the droplets has been set to 1 mm to prevent adjacent droplets from merging. Particularly for creating discrete patterns, the liquid merging between neighboring droplets becomes problematic for lower SAR μPA electrodes as they are more susceptible to lateral spreading during the electrowetting process (further discussed in the next section). However, the merging event can be utilized for creating continuous patterns on the 3D substrate.

In order to characterize the TMV1cys printed on the μPA electrodes using SEM, an electroless Ni coating (identical to the process introduced in previous sections) was performed after the overnight incubation step. As shown in Figure 3-16a, all μPAs featuring different SARs/densities were successfully coated with the TMV1cys at the printed spots. The top-down SEM images taken at the droplet boundaries confirm the localized patterning of the TMV1cys within the 3D substrate with more surface functionalized particles identified on the printed side (left from the light-blue line) compared to the non-printed area (right from the light-blue line). However, it should be noted that the TMV1cys density on the μPA electrodes with higher SAR is noticeably less compared to that observed from the lower SAR electrodes. This can be

attributed to limited TMV1cys diffusion from top to bottom of the electrodes for dense microstructures. Also, compared to the previous efforts in the earlier sections, the reduced volume of the droplet-per-print seems to play a critical role for this result. Compared to the μPAs without electrowetting (Figure 3-16b), the nanoparticles assembled on the lower bottom of the pillar surfaces in Figure 3-16a (SAR 10:1) confirm that the ink solution has successfully reached the bottom surface with electrowetting, indicating that the use of higher concentration ink can help increase the biofunctionalization density on high SAR μPA electrodes.

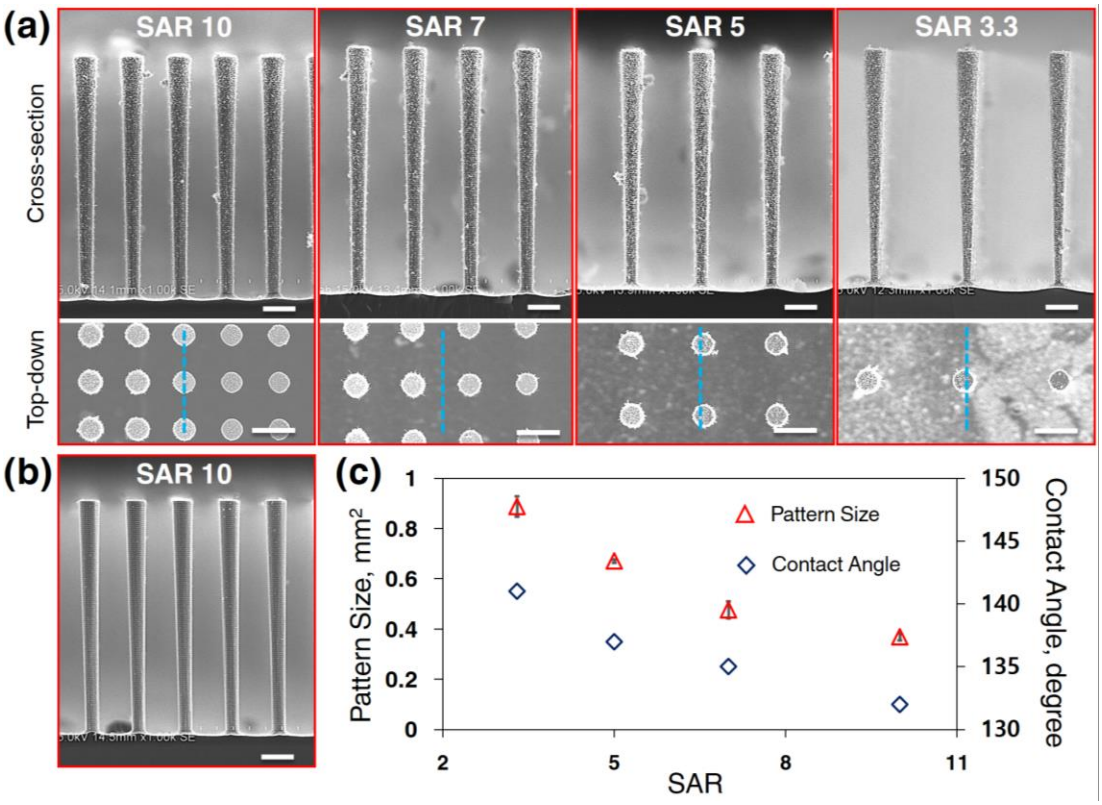

Figure 3-16: Process evaluation using SEM. (a, cross-section view) TMV1cys particle coating on all sidewalls of the μPAs has been achieved (observed as surface textures). (a, top-down view) Also, clear functionalization boundary has been observed at the wetting edges (blue-dotted line) of each of the μPAs highlighting the pattern fidelity enabled by structural hydrophobicity. (b) The clean surface of the μPAs processed without electrowetting further emphasizes electrowetting as an enabling technique for bio-printing. (c) The pattern sizes ranged from 0.89mm^2 to 0.37mm^2 (N=5) following the hydrophobicity levels of the μPAs. (scale bars: 10μm).

The dependence of the pattern/spot sizes on the SARs/pillar densities have been

characterized by estimating semi-circular pattern boundaries observed from top-down SEM images. Figure 3-16c compares the pattern sizes measured from the µPA electrodes with different SARs at the respective contact angles - representative of their hydrophobicity levels. The lower SAR µPA electrodes resulted in a larger pattern size due to the facile spreading of the bio-ink into the microcavities with the electrowetting (under the identical process settings, which is in a good agreement with our previous investigation. The statistical analysis using five different locations of a printed array show a high consistency in pattern size per SARs, emphasizing the excellent uniformity and repeatability of the 3D-EBP process.

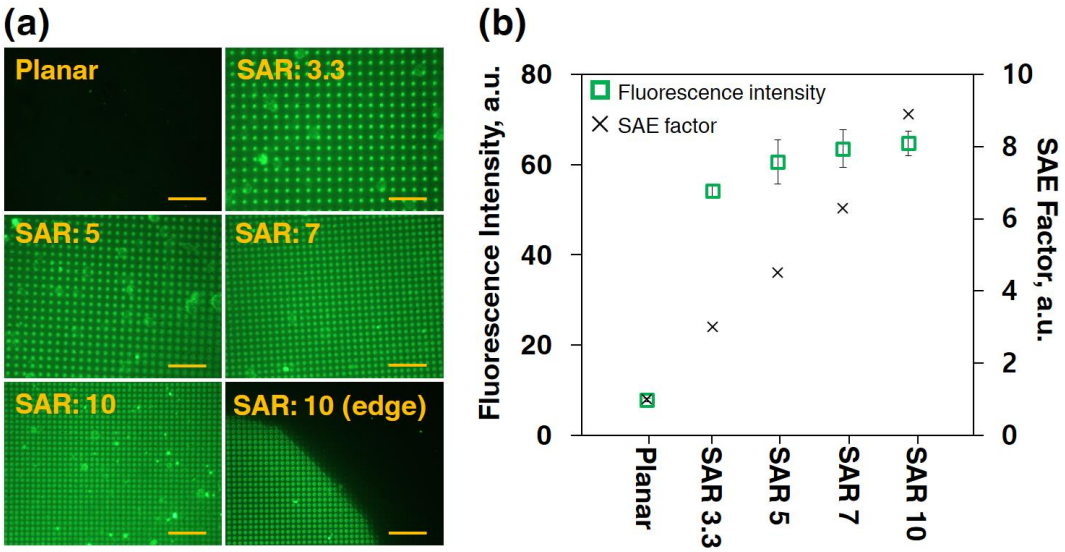

Figure 3-17: Characterization of fluorescence intensity from (a) TMV1cys functionalized on planar Au and µPA electrodes displaying SARs ranging from 3.3 to 10 (scale bars: 100µm). (b) A significant increase in functionalization density is achieve with the µPAs as reflected in the increase in fluorescence intensity (N=5).

As the electrowetted TMV1cys on µPAs enhances bionanoreceptor density by surface area enhancement (SAE) factors anticipated from the 3D electrode geometries, the focus of the fluorescence intensity characterization was on achieving scalable nanoreceptor density per different SARs of the µPAs. Figure 3-17a compares top-down

fluorescent microscopy images taken from the printed spots on different electrode geometries. Under an identical exposure time, TMV1cys printed on µPA electrodes resulted in a significantly higher fluorescence intensity compared to the planar electrodes with an excellent patterning fidelity (Figure 3-17a, bottom-right), due to the underlying microstructure. However, there is a noticeable discrepancy between the change in increment factor of the fluorescence intensity and the SAE factor calculated based on the µPA geometry (Figure 3-17b). This is attributed to the lower density of TMV1cys on the high SAR µPAs as supported by the SEM characterizations in Figure 3-16a, indicating that control over bio-ink concentration may need optimization to obtain highly controllable functional scalability of the resulting nano/micro/bio-integrated components.

3.6. Chapter Summary

In this chapter, the limited wetting property of the µPA to aqueous TMV1cys solution has been characterized in comparison with theoretical expectations. The characterization of TMV1cys assembly on Au-coated Si-µPAs having different micropillar densities has identified structural hydrophobicity as a key limiting factor for 3-D biofunctionalization. A major breakthrough of this study was achieved by adopting electrowetting principles, which circumvented structural hydrophobicity limitations to enable the controlled patterning of 3-D assembled bionanoreceptors on high-surface-area microstructures. Results from this study demonstrate the potential of electrowetting technologies to serve as robust platforms for the biofabrication of micro/nano/bio integrated 3-D devices and systems. These findings offer new possibilities for developing advanced 3-D components beneficial for a range of

microdevice applications including micro energy storage/harvesting, biochemical sensing, micro thermal management, water-repellent surfaces, etc.

The simple principles, readily available system components, and the minimal volumes of biological solutions have allowed further integration with an existing bioprinting system demonstrating a fully automated, scalable, and readily adaptable biomanufacturing technique available for a wide range of applications. While the presented demonstration utilizes a particular biomaterial of interest to our work (TMV1cys), this manufacturing technology is applicable for integrating other micro/nanomaterials (DNA, proteins, cells, carbon nanotubes, graphene, etc.), stored in aqueous media, onto conductive hydrophobic electrodes. Possible applications include developing energy storage/harvesting devices, biochemical sensors, optical metamaterials, heat management devices, superhydrophobic surfaces, and more. Overall, the innovative 3D biomanufacturing process generates excellent opportunities for advancing on-demand bio-integrated devices, opening up unprecedented possibilities in micro/nano/bio integrated fabrication technologies and platforms.

Chapter 4: Conjugation and Catalytic Activity of Enzymes on TMV

Prior to introducing the strategy adapted for immobilizing enzymes via TMV, previous works using TMV as a template for molecular assembly has been reviewed to identify potential bioconjugation routes suitable for this work. Table 4-1 (pp. 93) summarizes some of the major TMV modifications demonstrated over the past 15 years, providing diverse references showing TMV modification processes for a range of applications. Evidently, the genetic engineering and chemical conjugation strategies have interconnected critical roles that can vastly utilize TMV for implementation towards advanced nano- and micro- systems. For example, genetic engineering, which uses mainstream molecular biology techniques (e.g. recombinant DNA, polymer chain reaction, transformation into host cells, etc.), allows direct replacement or insertion of an alien amino acid group (e.g. cysteine) into the primary amino acid sequences (consisting of a chain of 158 amino acids), directing 100% modification of the viral coat-proteins. Also, small peptides specific to a target-of-interest can be expressed on surfaces ideal for developing biorecognition elements, vaccines, or targeted drug molecules. However, the scope of the compatible modifications are limited due to size restrictions and interaction stabilities between the neighboring amino acids, as the TMV coat proteins would not fold and bind correctly when the conditions are compromised.[219] Alternatively, chemical conjugations offer a wide range of tools and mechanisms to broaden the spectrum of potential functionalities and applications. The covalent binding sites available on either wild-type or genetically-engineered TMVs (e.g. Lys (amines), Tyr (aromatic carbons), Cys (thiols) allow direct or indirect conjugation of desired proteins onto TMV surface. However, the necessity for

cumbersome post-processing after purification of TMV particles and the complexity when optimizing conjugation steps are potential drawbacks compared to the genetic modification strategies.

4.1. On-Chip Chemical Conjugation Leveraging Genetically Engineered TMV

Among the range of TMV modification methods (Table 4-1), some of the prominently utilized modification strategies involve a combination of multiple techniques: genetic modification with inserted cysteines followed by chemical conjugation through thiol-maleimide reaction as described in Figure 4-1. The reaction can be induced in a buffered solution (pH6.5 - pH7.5) at room temperature and requires no catalytic reaction.[220] Given the reliability, efficiency, selectivity, and simplicity, the thiol-maleimide reactions have been a primary means of bioconjugation for several decades. However, while the application of cysteine-modified TMV has been widely demonstrated for the synthesis of inorganic materials, the use of thiol-maleimide conjugation for creating TMV-based biorecognition elements has only been demonstrated very recently by Koch and her co-workers by conjugating enzymes with hetero-bifunctional cross-linkers (CL).[52,136] Also, this previous work will be used as a benchmark for an on-chip bioconjugation process developed in this work with respect to the electrochemical performance.

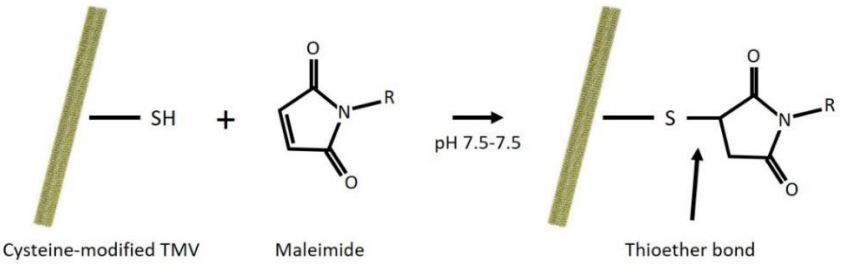

Figure 4-1. Conjugation of cysteine-modified TMV with maleimide through thioether bond.

Table 4-1. Modification strategies for TMV or TMV-VLPs in a wide range of research areas.

References	Areas of Research	Application	TMV Modification	
			Genetic Engineering	Chemical Conjugation
110	Inorganic nanomaterial synthesis	Metal (Co, Ni) nanowire synthesis	- Replaced Gly-155 with Ser-155	- N/A
112		Metal (Au, Ag, Pd) nanocomwire synthesis	- Inserted Cys on positions 2 and 3	- N/A
24,114,115		Metal (Co, Ni) nanostructure fabrication	- Inserted Cys on position 3	- N/A
221,222	Light harvesting nanomaterial	Chemophore-based light harvesting biomolecule	- Replaced Ser-123 with Cys-123	- Thiol-reactive chemophores onto Cys-123 via maleimide-thiol reaction
223		Light harvesting biomolecule with ZnP donor and FbP acceptor	- N/A	- FbP onto Cys-127 via maleimide-thiol reaction
224	Biorecognition elements	Fluorescent labeling	- Inserted Cys on position 3	- Fluorescent molecules onto Cys via maleimide-thiol reaction
130		Explosive chemical sensing	- Inserted TNT binding peptide on C-terminus with terminal TAG amber stop codon	- N/A
129,134		Antibody sensing	- Inserted FLAG-epitope on C-terminus with terminal TAG amber stop codon - Inserted Cys on position 3	- N/A
52,136		Enzymatic sensing	- Replaced Ser-3 with Cys-3	- Glucose oxidase and horse radish peroxide onto Cys using maleimide-biotin crosslinker
225	Vaccine development	TMV nanoparticle carrying tumor-associated antigen (Tn)	- Inserted Cys on position 3	- Tn1-antigen onto Cys-3 via S_N2 displacement reaction - Tn4-antigen onto Cys-3 via alkyne-maleimide crosslinker and CuAAC reaction - Tn-antigen onto Tyr-139 via diazonium coupling and CuAAC reaction
226,227		TMV nanoparticle carrying multiple protective antigens for *F. tularensis*	- Inserted Lys on N-terminus	- Antigenic proteins (OmpA, DnaK, and Tul4) onto Lys via EDC and NHS assisted catalytic reaction
228,229	Drug delivery	Photodynamic therapy for treatment of Melanoma cancer	- Replaced Thr-158 with Lys-158	- Zn-EpPor onto amines via "click" chemistry
230		pH responsive drug-delivery for cancer therapy	- N/A	- Anticancer drug doxorubicin onto Glu-97 and -106 of inner cavity using hydrazone bond - Cyclic Arg-Gly-Asp onto external surface through diazonium coupling and CuAAC on Tyr-139
50		Anticancer drug (phenanthriplatin) delivery	- N/A	- Cyanine5 dye onto Glu-97 and -106 on internal cavity via carbodiimide coupling and CuAAC
231	Bio-imaging	Supramolecular MRI contrast agents using paramagnetic gadolinium ions (Gd) chelated with DOTA	- N/A	- Conjugation of Gd(DOTA) onto Tyr (external surface) and Glu (internal channel) via dizonium coupling and CuAAC reaction
55		Nanocarrier for intravital imaging of brain vasculature	- N/A	- Imaging dye (BF3-NCS) onto exposed amines or hydroxyl groups on Tyr 139

- CuAAC: Copper(I)-catalyzed azide-alkyne cyclo-addition reaction ("click" chemistry) [232].
- The numbers after the amino acids indicate sequence of the primary amino acid chain of TMV CP (LTR reading), comprised of 158 amino acids.

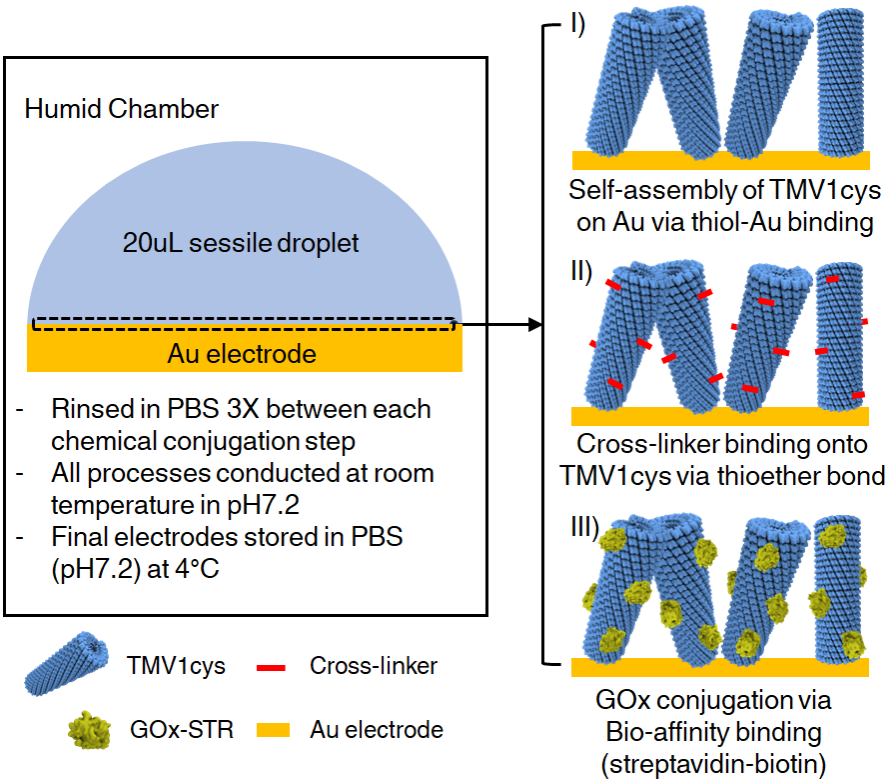

Figure 4-2. Illustrations outlining the on-chip TMV-GOx bioconjugation process.

Figure 4-2 illustrates the on-chip bioconjugation process developed in this work for GOx immobilization via TMV1cys: I) self-assembly of TMV1cys on Au surface by introducing 20 µl TMV1cys solution (0.2 mg/ml in 0.1 M phosphate buffer, pH7) covering surface area of ~7 mm^2. The electrode sample was incubated overnight at room temperature for the self-assembly. This was followed by successive introductions of II) a CL (EZ-Link^{TM} maleimide-PEG_{11}-biotin) and III) streptavidin-conjugated GOx (GOx-STR). Each conjugation step lasted 5 hours at room temperature and the electrode surface was rinsed 3X in PBS after each step to remove any unreacted/excess molecules. It should be highlighted that the GOx immobilization in this work is conducted directly on the device surface to leverage the robust and high density TMV1cys self-assembly on Au surfaces. This differs from the previous work,[52,136]

where the conjugation steps were conducted prior to electrode immobilization. The simple conjugation reactions (thiol-maleimide binding and biotin-streptavidin binding) requiring only proper control over pH levels at room temperature in the absence of any catalytic reagents allowed facile bioconjugation process on-chip where control over reaction conditions (e.g. mixing between solutions, species concentrations) is not easily obtainable.

The GOx immobilization density can be varied depending on the density of self-assembled TMV1cys and conjugation efficiencies between the thiol-maleimide (thioether bond) and biotin-streptavidin (bio-affinity) binding. In the previous work by Backer et al.,[52] maximum conjugation efficiency of 50% was achieved (50% of surface cysteines on TMV being conjugated with GOx) by optimizing the molar concentration ratios between the reaction molecules. The key factor in achieving maximum occupancy of GOx on TMV1cys surface is maintaining the high molar concentrations of the binding molecules (e.g. CL or GOx-STR) compared to that of the binding substrate (TMV1cys or TMV1cys/CL depending on the conjugation steps), in the conjugation solution. However, this was not a viable approach in this case as the molar concentration of the surface functionalized molecules could not be quantified. Alternatively, consistent concentrations of TMV1cys (0.2 mg/ml in 1X PBS, pH7) and CL (2.5 mg/ml in 1:9 DMSO:PBS) has been used while the concentration of GOx were varied. The molar mass of a TMV1cys particle is about ~40 MDa with ~2130 thiols/particle. The 0.2 mg/ml of TMV1cys translates into 5 nM concentration of TMV1cys, and ~10.7 μM for the surface exposed thiols. Considering the molar mass of the CL is 922.09 Da, the molar concentration of the CL used in the conjugation step

is 2.71 mM, which in result exceeds a recommended concentration ratio of 1:20 for maximum binding reaction (note that the amount of self-assembled TMV1cys is less compared to its original solution). The GOx-STR comes in 1 mg/ml concentration (in PBS, pH7.2) when purchased. Considering the 135 kDa of GOx-STR molar mass (80 kDa for GOx + 55 kDa for STR). This translates into 7.4 μM of GOx-STR molar concentration in its original solution. Since this concentration is on the order to that of TMV1cys solution during self-assembly, different concentration ranges has been used for the on-chip bioconjugation process to investigate the need for higher molar concentration GOx-STR.

4.2. Characterization of Enzymatic Activity On Chip via Colorimetric Assay

Prior to electrochemical characterization of the TMV/CL/GOx electrodes, a colorimetric assay was performed to confirm enzymatic activity of GOx immobilized via the on-chip conjugation method. As described in the sequential stoichiometry equations below (Eq. 4-1 and 4-2), H_2O_2 is a byproduct of glucose oxidation catalyzed by GOx and can be measured by introducing a reporter enzyme, horseradish peroxidase (HRP), with a chromogenic substrate. Luminol, which is widely known as a chemiluminescence substrate emitting weak light (λ = 425 nm) upon HRP catalyzed reaction, is used as the chromogenic substrate in this work; the reduced product of the luminol, 3-aminophtalic acid, results in a color change of the reaction solution and the optical absorption can be correlated with the level of enzymatic reaction.

GOx reaction: β-D-Glucose + O_2 → D-gluconolactone + H_2O_2 (4-1)

HRP reaction: Luminol + H_2O_2 → 3-aminophthalic acid + hν + N_2 (4-2)

The enzymatic reactions for the colorimetric assay was carried out in 1 ml polystyrene cuvette: 1) the reaction mixture was prepared by adding 10 µl of HRP (prepared 1X PBS, 100X dilution) and 1 µl of luminol (prepared in DMSO, 1000X dilution) solutions into 980 µl of 1X PBS (pH7.2). 2) After immersing the electrodes, 10 µl of glucose solution prepared in a 100X higher concentration of the targeted level was mixed and left suspended for 15 minutes to allow production of H_2O_2, inducing a color change with the oxidized luminol (3-aminophtalic acid) via HRP. After 15 minutes, the electrodes were removed from the reaction mixture and 700 µl of the reacted solution was transferred to a quartz crystal cuvette to perform optical UV-Vis absorption spectroscopy in the wavelength (λ) range of 250-600nm.

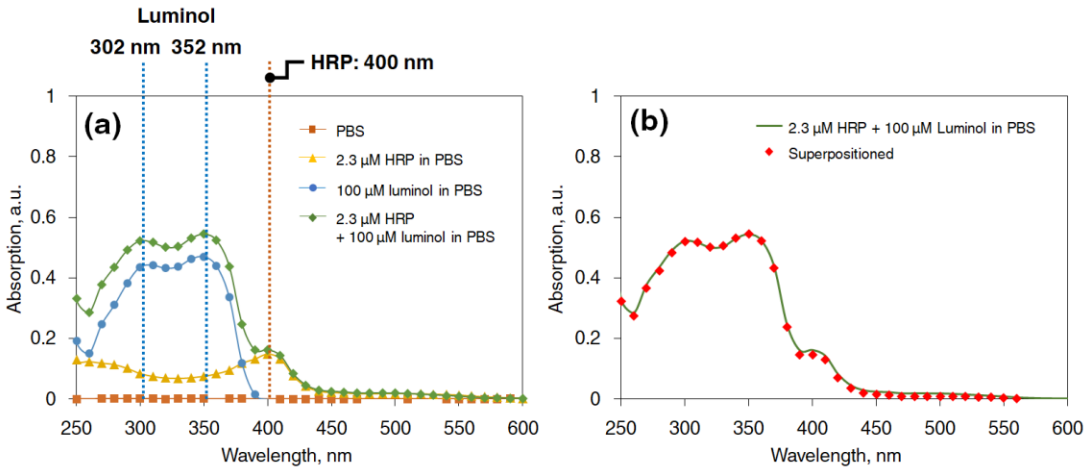

Figure 4-3. Baseline UV-Vis absorption spectra acquired from reaction solution for the colorimetric assay: (a) Signature absorption spectra for luminol, HRP and their mixture. (b) The tight overlapping of the absorption spectrum from HRP/luminol mixture over a superpositioned spectra independently acquired from HRP and luminol solutions.

Luminol and HRP have specific absorption peaks at $\lambda_{luminol}$ = 302 nm and 352 nm and λ_{HRP} = 400 nm, respectively. Figure 4-3a shows a baseline scan (without glucose-GOx reaction) to confirm those peak positions from the reaction solution. The overlap of the two absorption spectrums (Figure 4-3b) from 1) a solution mixed with both luminol and HRP (green line) and 2) a superposition of the spectrums acquired independently (red diamond) is shown to support that further change in the absorption spectra is due to the oxidation of luminol in the presence of H_2O_2.

Figure 4-4a shows the change in absorption spectrum with the enzymatic reaction on electrodes at different glucose concentrations. Compared to the experiments for Figure 4-4, luminol concentration was increased by 1.5X (100 μM to 150 μM) and the HRP concentration was reduced by 30% (2.3 μM to 0.7 μM) to reduce the overlap from HRP peak at λ_{HRP} = 400 nm and to increase the absorption response from 3-aminophtalic acid at $\lambda_{3\text{-aminophtalic acid}}$ = 390 nm, respectively. As clearly shown, the absorption intensity from luminol at both λ = 302 nm and 352 nm is decreasing as it is being oxidized to 3-aminophthalic acid. Also, an increase in absorption intensity above λ = ~370 nm is observed corresponding to the yellowish color change of the reaction solutions as shown in Figure 4-4b. The 10 mM glucose concentration did not fall into the incremental trend (Figure 4-4c), corresponding to the results in the luminol absorption regime, where higher absorption intensities were measured at both λ = 302 nm and 352 nm, this is considered to be due to the deviations in the density or activity of the immobilized enzymes. Based on these results, absorption at $\lambda_{3\text{-aminophtalic acid}}$ = ~390 nm was selected for further analysis.

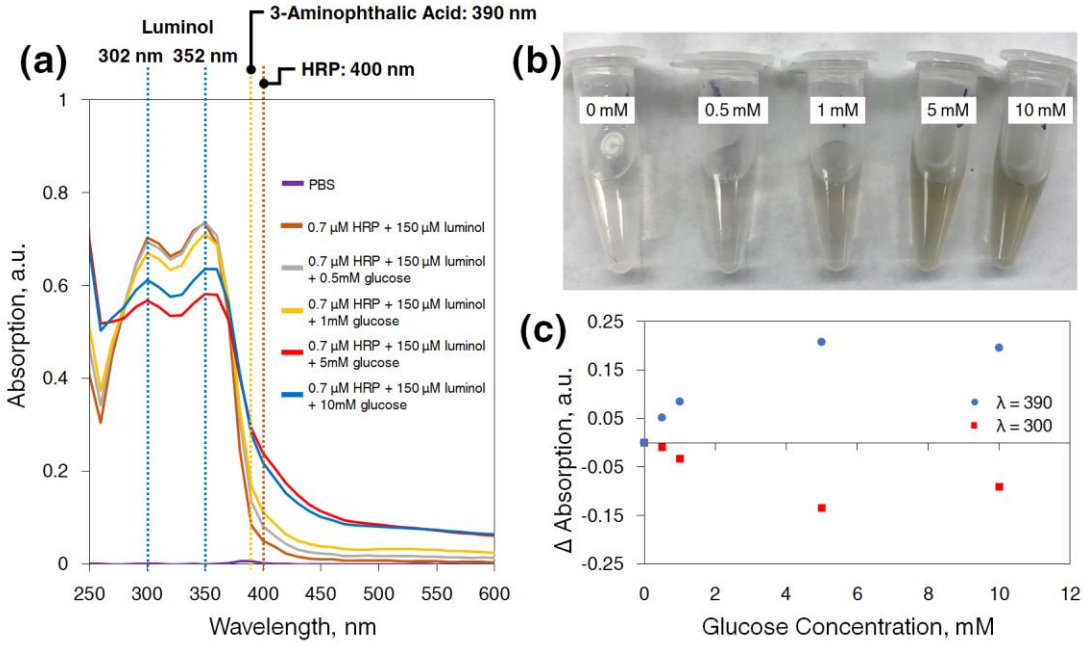

Figure 4-4. Colorimetric assay with Au/TMV1cys/CL/GOx electrode at different glucose concentrations: (a) Oxidation of luminol results in decrease in optical absorption at λ = 302 nm and 352, while there is an increase in absorption at the wavelength range above λ = 370 nm. (b) Optical images of the analyzed reaction mixtures showing yellowish color with different color density corresponding to the glucose concentration. (c) Relative change in absorption with respect to 0 mM glucose concentration sample to show corresponding opposite-trend change between at peak locations associated with maleimide and 3-aminophthalic acid (yellowish color).

In order to confirm effectiveness of the TMV1cys and the chemical conjugation strategy for GOx immobilization, the colorimetric assay was performed with six different electrodes:

E1: Bare Au (Au);

E2: TMV1cys self-assembled on Au (Au/TMV1cys);

E3: TMV1cys conjugated with CL on Au (Au/TMV1cys/CL);

E4: Non-specifically bound GOx on Au (Au/GOx);

E5: Non-specifically bound GOx on Au/TMV1cys (Au/TMV1cys/GOx);

E6: Chemically conjugated GOx on Au/TMV1cys/CL (Au/TMV1cys/CL/GOx);

The absorption intensity acquired is shown in Figure 4-5a. The electrodes samples (E1-E3) as negative controls showed no relative change in optical density compared to a baseline measured without any electrodes immersed. Compared to the positive controls injected with GOx (E4 and E5) the GOx immobilized onto the Au surface via TMV1cys (E6) showed a higher colorimetric response resulting in higher optical density. This confirms that the TMV1cys and the crosslinking chemistry was effective for robust and high-density immobilization compared to the non-specifically bound GOx samples. The luminol concentration in this case was further increased/adjusted compared to the initial response characterizations (Figure 4-3) by a factor of 4 to increase the absorption intensity response range to better observe the differences between the electrode samples.

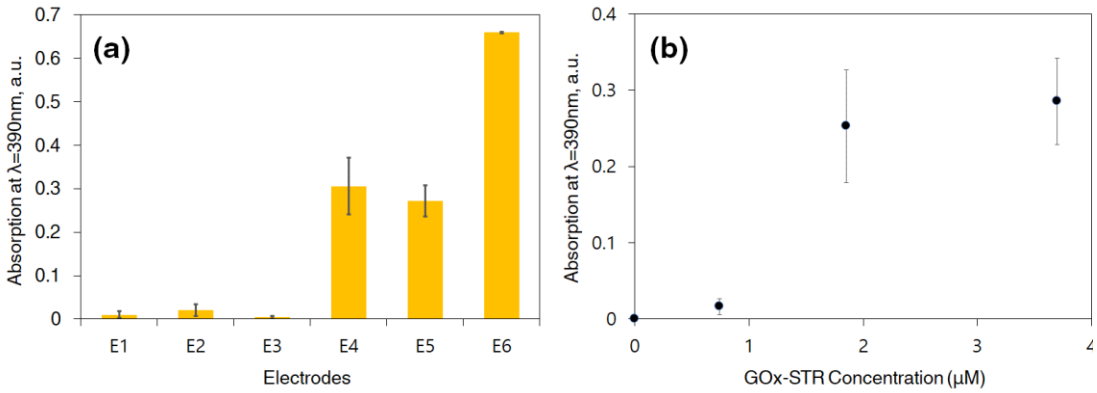

Figure 4-5. Colorimetric assay of electrodes prepared in different conditions to (a) confirm effectiveness of the on-chip bioconjugation method and (b) investigate dependence of GOx-STR concentration used in the bioconjugation step to electrode enzymatic activity.

As mentioned in section 4.1, the relatively low molar concentration of the GOx-STR solution (7.4 μM) brings a consideration for maximizing the GOx immobilization as its concentration is comparable to the surface exposed thiols on TMV1cys solution (~10.7 μM) used in the self-assembly step. In order to understand this potential

limitation, the Au/TMV1cys/CL/GOx samples were prepared with different GOx molar concentrations following the protocol described in section 4.1. Fortunately, the absorption intensity acquired from the different electrodes shown in Figure 4-5b indicated that the enzymatic activity on the electrodes results in a saturation at its increase above GOx-STR concentration of ~2 μM. Based on this result, 3.7 uM of GOx-STR (50% dilution of the original stock) was used as an optimal concentration for the on-chip conjugation step.

4.3. Scalable Enzymatic Activity On-Chip

The on-chip bioconjugation method has been combined with the electrowetting-assisted 3D biofabrication technique (3D-EBP) developed in Chapter 3 towards the demonstration of an enhanced and scalable enzymatic activity on bioelectronic devices. As illustrated in Figure 4.6, 3D-EBP was used for introducing TMV1cys onto the Au-coated Si μPA electrodes, allowing for a uniform coating over the 3-D surface. This also generated a pathway for additional molecules to be introduced in the sequential conjugation steps for GOx immobilization. All process steps are thus identical as introduced above except the use of 3D-EBP at the initial wetting of the TMV1cys solution into the μPA cavities. In order to evaluate the scalable enzymatic activity on the electrodes due to the 3-D microdevice structure, two different μPA electrodes featuring surface area enhancement (SAE) factors of 3 (pillar spacing: 21 μm) and 6.3 (pillar spacing: 10 μm) has been utilized (pillar diameter and height is 7 μm and 70 μm, respectively, and see section 2.1 for the details on SAE calculation) to compare with the results from planar Au electrodes.

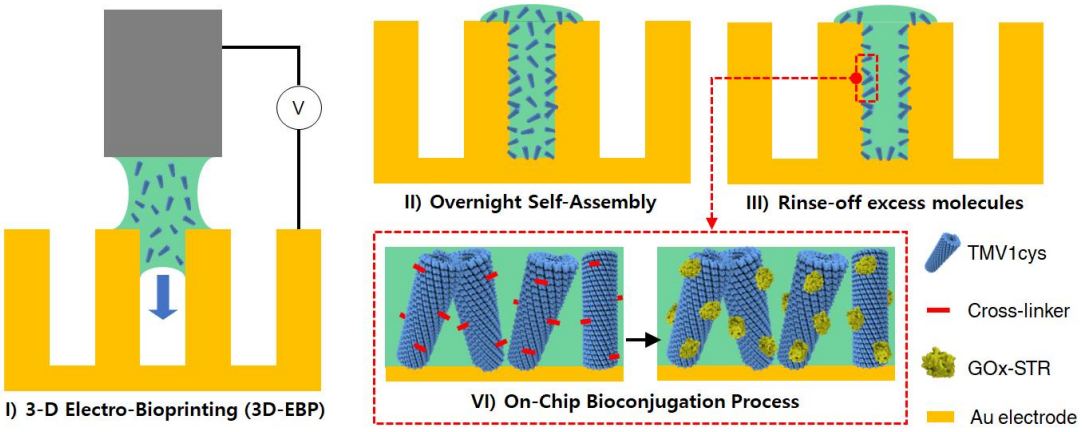

Figure 4-6. Illustration of the 3D-EBP incorporated bioconjugation process on Au-coated Si µPA electrodes.

The colorimetric assay was performed as described above with 2.3 µM HRP, 150 uM luminol, and 10 mM glucose in 1 ml PBS (pH7.2) solution with the electrodes immersed for 15-mins at room temperature. Considering the different droplet spot sizes per substrate wettability when introducing the TMV1cys via 3D-EBP (see Figure 3-16c), specific absorption intensities have been derived for a proper evaluation, which divides the original absorption intensity acquired from the reaction solution by the foot-print area occupied by the droplet after 3D-EBP (the foot-print areas were calculated using an image processing software, ImageJ). It should be noted that this method assumes the absorption intensity (below 1) is linearly proportional to the enzymatic reaction rate occurring at the electrodes, and this can be supported by the corresponding increase in the absorption intensity versus glucose concentration shown in Figure 4-4c.

Figure 4-7 compares the SAE factors of the different electrodes with the corresponding increase in specific absorption intensities achieving scalable enzymatic activity on chip. Compared to the TMV1cys/CL/GOx on planar electrodes, the µPA electrodes amplified the enzymatic reaction rates by factors of 4 and 5.5 with the µPA

electrodes featuring SAE factors of 3 and 6.3, respectively. This is significant, providing a highly scalable process for designing enzymatic reaction rates or the immobilization densities on chip that is easily applicable for a broad range of applications (biomimetic material synthesis, bioenergy harvesting, biosensors, etc.). The deviations between the two factors (SAE and incremental factor of the specific absorption intensity) can be attributed to the 1) variations in TMV1cys self-assembly density per electrode geometry (Figure 3-16a), and 2) the potentially limited diffusion/access of the conjugation molecules (CL, GOx-STR) into the high-aspect-ratio microcavities. Optimizations with respect to solution concentrations per SAE/geometry and droplet mixing on the chip can further help advance the developed technology, provided that the essential process for 3-D bio-device integration is viable for creating functional and scalable bioelectronics components.

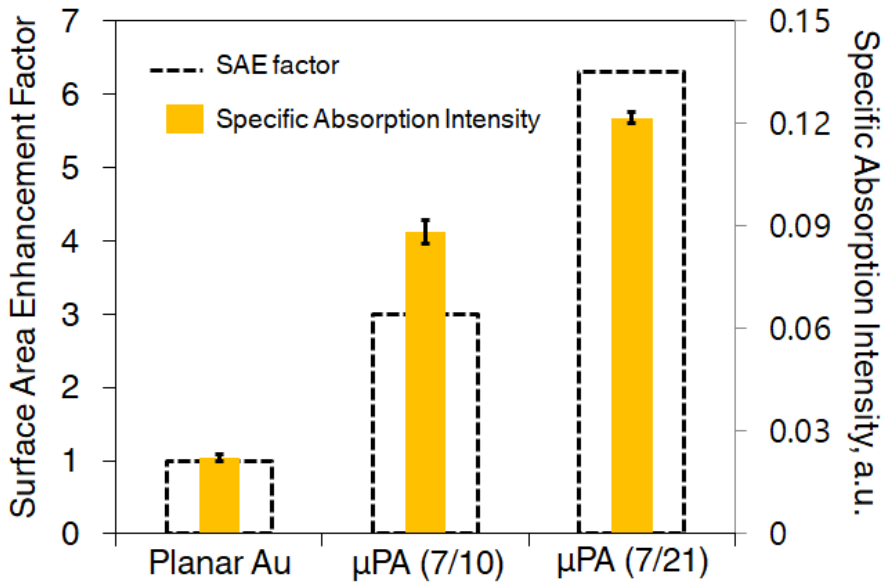

Figure 4-7. Scalable enzymatic activity on-chip enabled by 3D-EBP process on µPA electrodes (the ratios in parenthesis on the x-axis labels indicate pillar diameter/pillar spacing).

4.4. Understanding Electrode Kinetics with TMV/CL/GOx Conjugations

While the TMV provide an excellent template for high-density GOx immobilization, it is important to understand how the electron transfer kinetics are affected by the passivation of non-conducting proteins. As discussed in section 1.3.4, different charge transfer mechanisms (e.g. mediated electron transfer, direct electron transfer) have been investigated for enzyme-electrode systems. An effective charge transfer mechanism is mainly determined by the arrangement of GOx with respect to the electrode surface. Particularly, a close proximity between the GOx and the conductive element is important for efficient charge transfer. High-surface-area conductive nanomaterials such as carbon nanotubes for gold nanoparticles have been widely utilized as electrode materials to increase both the current density and potential that GOx will interface at close proximity (with and without specific chemical conjugation).[163,233] Combining the nanoscale electrode materials with the TMV-assembled GOx is an attractive approach for enhancing the performance of enzyme-based bioelectronics through more regular and high-density arrangement on the enzyme onto the conductive elements. However, considering the scope of this work, the electrochemical characterizations introduced in this chapter will focus on 1) investigating the effect of biomolecules immobilized on the Au surface on the charge transfer kinetics, 2) identifying the primary charge transfer mechanism, and 3) achieving scalability in the electrochemical performance with the incorporation of the microscale electrodes (Au-coated Si-μPAs). All electrochemical characterization was performed at room temperature in 1X PBS, pH7.2.

As a first step, the impact of TMV1cys self-assembly onto planar Au electrodes on charge transfer kinetics has been investigated using cyclic voltammetry (CV, scan range: -0.1 - 0.6 V vs. Ag/AgCl, scan rate: 100mV/s). The characterization was performed in a beaker-level testing set-up with a three-electrode configuration (reference: Ag/AgCl, counter: Pt, working: TMV self-assembled Au electrodes). Potassium ferri/ferrocyanide (1 mM $K_3Fe(CN)_6^{3-/4-}$ in 1X PBS (pH 7.2) was used as an electrolyte. The redox current at the Au electrode is a result of the redox reaction of redox-couples ($[Fe(CN)6]^{3-}$ and $[Fe(CN)_6]^{4-}$).

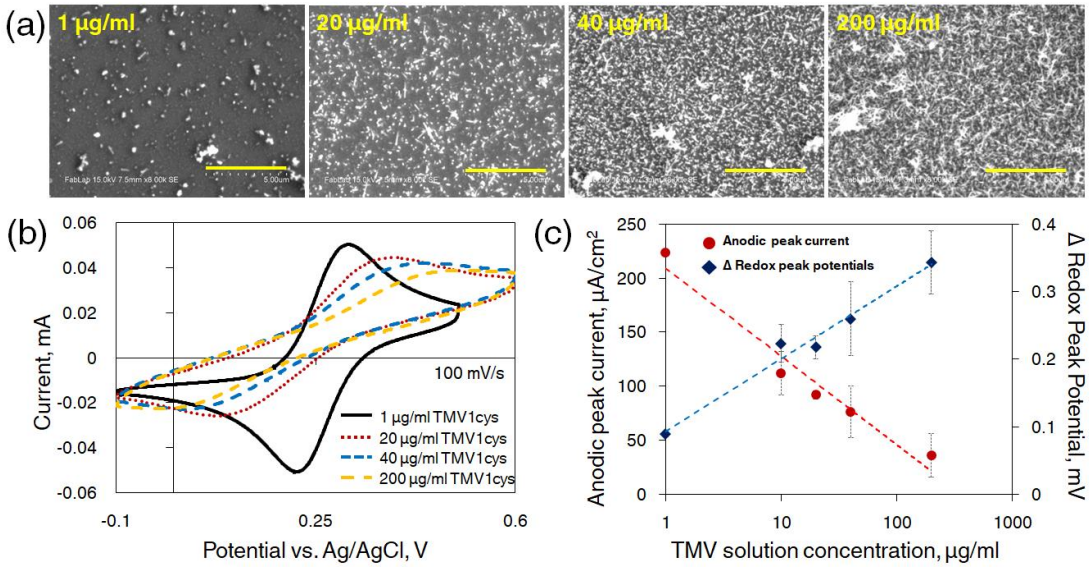

Figure 4-8. Impact of TMV1cys self-assembly to electrode kinetics: (a) Top-down SEM images of Au electrodes with different densities of self-assembled TMV1cys particles (scale bar: 5µm, the images are taken after electroless Ni coating). (b) Cyclic voltammograms acquired from the four different electrodes in 1 mM $Fe(CN)6^{3-/4-}$ solution in 1X PBS (pH7) and (c) analysis of the change in peak potential separation and oxidation peak current density showing shift in electrode kinetics from a diffusion-limited to a rate-determined process (N=3).

Figure 4-8a shows top-down SEM images of the Au electrodes with different densities of TMV1cys particles, achieved by using different solution concentrations in the self-assembly step. Electroless Ni metallization was performed after

electrochemical characterizations for SEM imaging, and this further highlights the robustness of the TMV structure and their binding to the gold electrodes. Figure 4-8b and 4-8c show the cyclic voltammograms at different TMV1cys surface densities and the electrode charge transfer-associated parameters, respectively. The correspondence of both the incremental peak potential separations and the decrease in current peak intensities, at the same scan rate (100 mV/s), to the surface density implies a decrease in electrode kinetics; the rate of electron transfer at the electrodes is likely reduced due to the surface passivation with TMV1cys. The range of the peak separations and the comparable levels between the oxidation and reduction peak intensities imply that the charge transfer reaction is in a quasi-reversible regime, indicating that the resulting currents are predominately governed by the rate of electron transfer rather than a diffusion-limited process (Nernstian).[234] Compared to previous studies, using smaller organo-thiol molecules for formation of self-assembled monolayers (SAM) of respective organic molecules, the result indicates that there are "pin-holes" between the assembled TMV1cys particles or via the central channels of TMV1cys, allowing redox species to access electrode surface for reactions; complete coverage achieved using the smaller thiol molecules results in no electrochemical current response. [63,235]

The electrochemical characterization with GOx conjugation was performed as shown in Figure 4-9a. Notably, the conjugation of GOx onto TMV1cys via CL resulted in a further decrease in charge transfer kinetics with a wider separation in the redox peak potentials (Au: 87 mV, Au/TMV1cys: 604 mV, and Au/TMV1cys/CL/GOx: 830 mV vs. Ag/AgCl) and a decrease in peak current levels. This is attributed to further blocking of the pinholes reducing the rate of electron transfers at the electrode surface

(Figure 4-9b). It should be noted here that the scan range for the CV needed to be broadened to -0.5 - 0.7 V in comparison to the results shown in Figure 4-8b to be able to observe the redox peak configuration beyond the -0.1 - 0.5 V potential window. Also, a lower scan rate of 5 mV/s was needed as the electrode kinetics became more rate-determined; the redox peaks could not be clearly identified at higher scan rates. Based on the change in electrode kinetics with TMV1cys/CL/GOx conjugations, the experiments in the following section, consisting of characterizing the electrochemical conversion of the enzyme-based catalytic reaction, were carried out by focusing at redox potentials around -0.3 V (cathodic reaction) and ~0.5 V (anodic reaction) vs. Ag/AgCl.

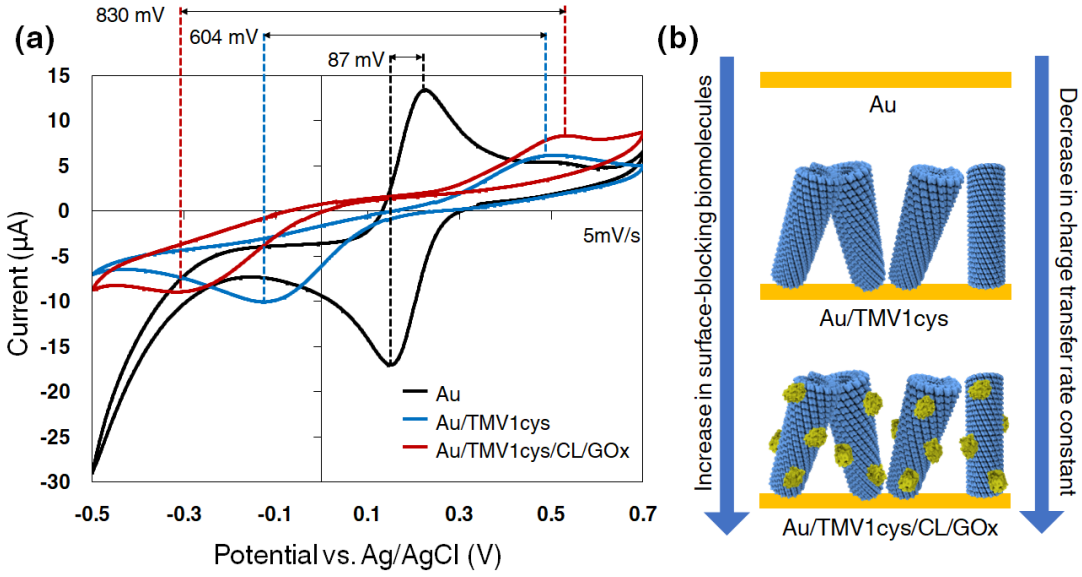

Figure 4-9. Impact of TMV1cys/CL/GOx conjugations on Au electrode to the electrode reaction kinetics: (a) Cyclic voltammograms acquired from Au, Au/TMV1cys, and Au/TMV1cys/CL/GOx electrodes 1 mM $Fe(CN)6^{3-/4-}$ solution in 1X PBS (pH7) showing increase in the redox peak separation and decrease in the redox current levels with respect to the on-chip GOx conjugation steps. (b) Illustrations of the increase in the biomolecules (TMV1cys and GOx) with the sequential bioconjugation steps decreasing the accessibility of reactive species (e.g. $Fe(CN)_6^{3-/4-}$) to the electrode surface causing relatively slower electrode charge transfer.

4.5. Electrochemical Conversion of Enzymatic Reactions for Biosensing and Energy Harvesting

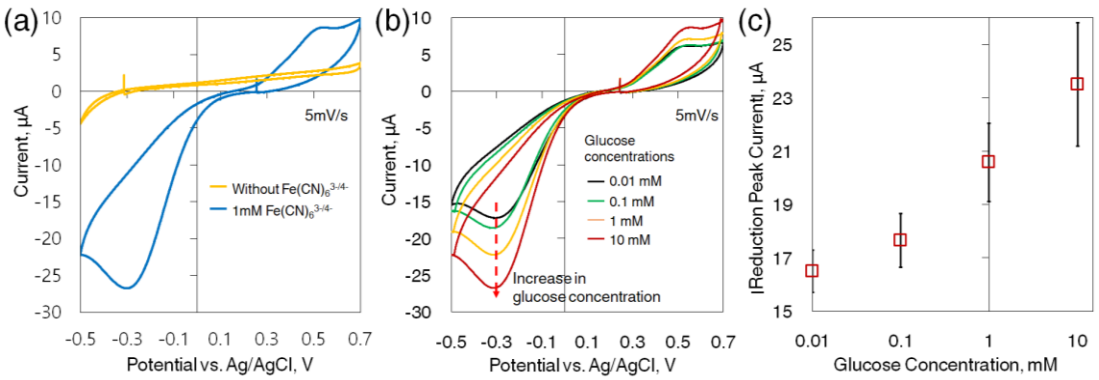

Figure 4-10. (a) Electrochemical characterizations (a) determining MET as an effective charge transfer mechanism and (b) demonstrating the change in redox current response corresponding to the glucose concentrations (10 uM -10 mM). (c) A calibration curve is generated using absolute reduction current peaks to highlight the excellent glucose sensing capability (N=3).

In order to obtain electrochemical conversion of the enzymatic reactions, the $Fe(CN)_6^{3-/4-}$ redox couple was used as an electron mediator to convey enzymatic reaction-generated electrons to the Au electrodes (mediated electron transfer, MET). This was necessary as the direct electron transfer (DET) mechanism was not possible as indicated in Figure 4-10a - without the mediator molecule, no redox current peaks were observed in the CV curve in the presence of glucose. This is attributed to the use of planar Au as an electrode material which does not create a desirable arrangement of GOx on the conductive element – the cofactor/redox center, flavin adenine dinucleotide (FAD), of GOx should be directly accessible by the conductive medium with a stringent theoretical distance requirement (<1.5 nm).[236]

With the MET, an electrochemical response in CV corresponding to the glucose concentration was achieved, as shown in Figure 4-10b, confirming successful electrochemical conversion of the enzymatic reaction. Figure 4-10c plots a calibration curve of the absolute reduction current corresponding to the glucose concentration

levels (10 uM – 10 mM) demonstrating the excellent performance of the Au/TMV1cys/CL/GOx electrodes as glucose sensors. It should be noted that the reduction current was selected for determining the sensing capability as the oxidation currents showed rate-determined behavior with limited current levels compared to the reduction currents. Particularly, the results can be compared with a recent similar work by Backer et al.,[52] where they demonstrated glucose sensing with post-immobilization of TMV1cys/CL/GOx on Pt electrodes (see section 4.1 for more details). In comparing the current density at the same glucose concentration, more than a 20-fold increase in current density (~3.4 $\mu A/mm^2$ vs. ~0.13 uA/mm^2 at 10 mM glucose concentration) is achieved with this on-chip immobilization approach. The significant difference is most likely due to 1) the increased GOx immobilization density with high-density self-assembly of TMV1cys on Au surface and 2) the advanced generation of glucose sensing mechanism (2^{nd} generation of glucose sensors relying on MET) incorporated in this work, whereas the previous work relied on direct reduction of H_2O_2, produced from the enzymatic reaction, on Pt electrodes (1^{st} generation of glucose sensors).

The MET mechanism with the $Fe(CN)6^{3-/4-}$ mediator is outlined in the following equations (Eq. 4-1 through 4-7). Equations 4-1 through 4-4 describe the electrode reactions for the reduction current. The first two (Eq. 4-1 and 4-2) describes the catalytic reaction via the cofactor of GOx, FAD, oxidizing glucose into gluconic acid and generating H_2O_2. The following two equations (Eq. 4-3, and 4-4) describe the mediated cycling reaction where the ferricyanide ($Fe(CN)_6^{3-}$) is reduced at the electrodes, then replenished to ferrocyanide ($Fe(CN)_6^{4-}$ by H_2O_2. Considering that the change in the redox current peaks is observed at the potential positions for the CV

acquired with $Fe(CN)_6^{3-/4-}$ only (shown in Figure 4-10a), it can be implied that the reduction current is mainly governed by the mediated reaction rather than a direct reduction of H_2O_2 on Au.[10] The increase in the oxidation current corresponding to the glucose concentration, observed in potential range above 0.3 V vs. Ag/AgCl, is also associated with the mediated cycling reaction as outlined in Eq. 4-5 through 4-7, which is the standard MET mechanism considered as the 2nd generation glucose sensing.[10]

Reduction reactions:

GOx (FAD) + Glucose → $FADH_2$ + Gluconic acid (Eq. 4-1)

$FADH_2 + O_2$ → $FAD + H_2O_2$ (Eq. 4-2)

$Fe(CN)_6^{4-} + H_2O_2 + 2H+$ → $Fe(CN)_6^{3-} + 2H_2O_2$ (Eq. 4-3)

$Fe(CN)_6^{3-} + 2e^-$ → $Fe(CN)_6^{4-}$ (charge transfer reaction) (Eq. 4-4)

Oxidation reactions:

GOx (FAD) + Glucose → $FADH_2$ + Gluconic acid (Eq. 4-5)

$FADH_2 + 2Fe(CN)_6^{3-}$ → $FAD + 2Fe(CN)_6^{4-} + 2H^+$ (Eq. 4-6)

$2Fe(CN)_6^{4-}$ → $2Fe(CN)_6^{3-} + 2e^-$ (charge transfer reaction) (Eq. 4-7)

The Au/TMV1cys/CL/GOx was assembled with a Pt electrode to investigate bioenergy harvesting performance. In general, the GOx immobilized electrode functions as an anode providing electrons to a connected load, and Pt can be used as a cathode taking electrons in its oxygen reduction reaction (ORR).[237] The anodic reaction can be better understood by the oxidation reaction described in Eq. 4-5 - 4-7. The hydrogen ions generated in this reaction (Eq. 4-6) are provided to the Pt cathode for the ORR reaction generating H_2O (Eq. 4-8) by taking electrons from the load.

Oxygen reduction reaction on Pt:

$O_2 + 4H^+ + 4e^- \rightarrow 2H_2O$ (Eq. 4-8)

The bioenergy harvesting performance of the Au/TMV1cys/CL/GOx (anode) - Pt (cathode) assembled enzymatic-biofuel-cell (EBC) has been characterized in a beaker cell with 1X PBS (pH7.2) in room temperature (Figure 4-11a). Ferri/ferrocyanide (1 mM $Fe(CN)_6^{3-/4-}$) and 10 mM glucose were included to facilitate the anodic electrode reactions, and the ambient dissolved oxygen was used as the fuel for the cathodic ORR reaction on Pt. The biofuel cell was connected to different resistive loads and the corresponding change in voltage across the load was measured using a potentiostat (Biologic VSP-300) to obtain a polarization curve, describing the power performance of the EBC. Considering the electrode reduction potential for O_2 on a Pt electrode (vs. Ag/AgCl) is ~0.61 V (at neutral pH), the open-circuit potential (OCP) of the assembled biofuel cell is anticipated to be within a ~ 0.1 – 0.15 V range considering that the oxidation reaction of the GOx electrode occurring at around 0.5 V vs. Ag/AgCl. This was evident in the results shown in Figure 4-11b: the open-circuit potential (OCP, with no resistive load connected) is measured to be ~ 149 mV and shows a typical response of decreasing OCP/load potential with increasing current due to the limited charge flow kinetics in fuel cell systems.[16] The glitches in Figure 4-11b are due to switching of resistors during the continuous measurement. When converted into the polarization curve shown in Figure 4-11c, the EBC generated a maximum power density of 0.86 $\mu W/cm^2$ at a current density of 10.2 $\mu A/cm^2$. It should be noted that the surface area for the areal density calculation is the Au electrode surface area immobilized with TMV1cys/CL/GOx.

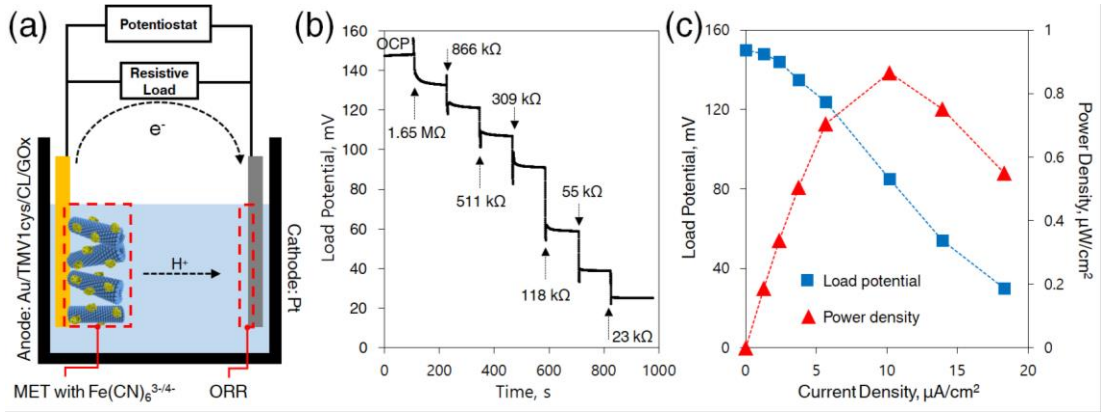

Figure 4-11. Characterization of Au/TMV1cys/CL/GOx electrodes as an anode for bioenergy harvesting applications. (a) Cross-sectional schematic of the assembled EBC illustrating charge flow directions and the characterization method. (b) A plot of OCP over time with successive replacement of the load resistors for characterizing power performance, and the (c) polarization curve plotted based on the OCP measurement.

Compared to the previously reported works using high surface area conductive nanomaterials,[238] both the OCP and the power density - the standard measures for EBC performance evaluation – resulted in a low range. This is attributed to a couple of major reasons: 1) a lack of nanoscale conductive material in the electrode system which can widen the OCP by reducing the oxidation potential of the anodic electrode via facilitated electron charge transfer from the enzymatic reactions and 2) the wide distance between the electrodes, which increases the resistance for hydrogen ion diffusion across the electrodes in the electrolyte. However, knowing that the EBC assembled with Au/TMV1cys/CL/GOx produces this polarization curve, the results achieved are significant in that they allow optimization of the EBC systems components to be pursued, including 1) combination of conductive nanomaterials for enhanced electron transfer, 2) replacement of Pt with oxygen reducing enzyme electrodes for increasing the OCP, and 3) miniaturization of the system with an ion-selective membrane to reduce the internal resistance. More significantly, with the

scalable enzymatic activity on a 3-D electrodes, demonstrated in section 4.3, the EBC performance can be enhanced in a controllable fashion by incorporating the geometry-controlled 3-D electrodes with 3D-EBP technique developed in Chapter 3.

4.6. Chapter Summary

In this chapter, an on-chip bioconjugation method has been developed for GOx immobilization using TMV1cys as a robust high-density molecular assembler. The thiol-Au binding mechanism available with the surface exposed thiols on TMV1cys allowed careful rinsing of unbound molecules after each conjugation step, which was critical for reproducible and reliable performance of the enzyme electrodes, as the control over concentration ratios between the reacting molecules is not feasible in this approach. The colorimetric assay using HRP and luminol confirmed the on-chip process to be effective, showing higher enzymatic activity for the Au/TMV1cys/CL/GOx compared to the positive controls. Particularly, compared to a recent work where a different immobilization method was used with the same bioconjugation chemistry, the developed method provides a more efficient biofabrication strategy by leveraging the optimized sample volumes/concentrations and by relying on the specific binding mechanisms between the biological template and the device surface. The on-chip conjugation strategy is also compatible with the electrowetting-assisted 3D biofabrication technique developed in Chapter 3, allowing for scalable enzymatic activity on a variety of device surfaces. In addition, the electrochemical characterization using the Au/TMV1cys/CL/GOx electrodes provides the fundamental understandings behind the charge transfer mechanisms for electrochemical conversion of the enzymatic reaction towards high performance

enzyme-based bioelectronics. Combined results should provide a powerful scalable approach for manufacturing enzymatic activity-controlled devices for a range of applications, including biochemistry research, sustainable chemical manufacturing, and energy harvesting solutions.

Chapter 5: Concluding Remarks

5.1. Summary

In this thesis research, an innovative biomanufacturing technology, 3D-EBP, has been developed enabling highly selective and scalable biomolecular assembly on 3-D device components. The successful integration of microscale 3-D device structures created via conventional microfabrication techniques with a nanoscale molecular assembler (TMV) enabled hierarchical and modular material assembly approach for creating highly functional and scalable bio-integrated microsystems components. Si-based μPA has been adapted as a model 3-D device structure throughout this work as it allows facile modulation of device functionalities and biomaterial interfacing properties via rational arrangement of highly ordered geometrical features. Cysteine-modified TMV (TMV1cys) has served as the biomolecular assembler based on its excellent functional features including the high surface area structure, densely arranged surface receptors, environmental robustness, and self-assembling property onto metal surfaces.

Initial efforts have focused on investigating the dependence of geometrical characteristics to the self-assembly of TMV1cys on the surface of Au-coated μPAs displaying different structural densities. The comparative studies have revealed that the self-assembly of TMV1cys on μPAs, particularly for high density pillar arrangements on the surfaces located at the deep microcavities, is limited causing failure to provide uniform surface functionality for reproducible device performance. Through a careful analysis of the surface morphology and functionalization profile within the microcavities of different pillar densities, a limited wetting property is present. In such

3-D micro/nano structured surfaces this has been identified as the key limiting factor for biomaterial integration with high surface area micro/nanodevices. In order to, evaluate the material assembly approach for high performance and scalable device performance, hierarchical electrodes assembled via combination of TMV1cys and μPAs of lower pillar densities have been characterized in a NiO-based electrochemical charge storage system, demonstrating a significant enhancement in both power and energy performances, and expanding the versatility of TMV1cys as a high-surface-area nanotemplate for assembling a wide variety of energy storage materials. The combined results indicated that an enabling method to overcome the limiting wetting property will allow biomaterial-based manufacturing methods to create fully scalable micro/nano device components.

Based on the understandings of the fundamental limitation behind the 3-D device-biomaterial integration, the surface wettability of the μPAs has been characterized using droplets of TMV1cys solution. The results combined with the theoretical derivation based on the Cassie-Baxter equation, indicated that the wetting property can be controlled by varying the μPA geometries. The 3D-EBP technology has been developed by leveraging this controllable factor in which the limited wetting property of the μPA allowed selective injection of the TMV1cys droplets into the microcavities, using a capacitive surface wettability-control technique, known as electrowetting. The droplets confined within the cavities then allowed localized self-assembly of the TMV1cys onto the wetted surfaces, enabling patterning of the biomacromolecules on the 3-D device substrate. The electrowetting technique, which modulates the surface wettability by applying electric potential at the solid-liquid

interface, was essential in the development of 3D-EBP. The characterizations of the structural and chemical features of TMV1cys post 3D-EBP strongly confirms that the biofabrication technique is compatible with the biomacromolecule, and no significant disturbances to its functional integrity were observed. The proof-of-concept demonstrations of the automated and programmable 3D-EBP, via a simple system integration with a commercial bioprinter, further emphasize the significance of the technology which has strong potential to generate excellent opportunities for advancing on-demand 3-D bio-integrated devices and systems.

The last part of this research has focused on demonstrating scalable biocatalytic activities on chip by conjugating glucose oxidase (GOx) onto the molecular assembler, TMV1cys. Relying on the robust self-assembly of TMV1cys on metal surfaces (e.g. Au), an on-chip chemical bioconjugation method has been developed for high density immobilization of GOx on TMV1cys via a heterobifunctional crosslinker (CL). The 3D-EBP has been applied to perform the bioconjugation process on μPA electrodes towards demonstration of scalable enzymatic activities on chip. The close correspondence of the enzymatic activities (measured via colorimetric assays) with the surface area enhancement (SAE) factors (derived based on the μPA geometry) strongly supports the successful incorporation of the developed biofabrication technology, enabling high controllability over the biocatalytic activity on chip. This fundamental understanding, derived from the electrochemical characterizations, behind the change in electrode kinetics associated with the TMV1cys/CL/GOx immobilization demonstrated both the biosensing and bioenergy harvesting capabilities. Particularly, a significantly higher redox current density was achieved compared to a recently

published work[52]. This strongly implies that the on-chip bioconjugation strategy was effective for high density enzyme immobilization via TMV1cys. Combining the enhanced and scalable enzymatic activity on chip with incorporation of the 3D-EBP, the developed methods provide a robust and readily employable strategy for advancing a range of enzyme-based bioelectronics and platforms.

5.2. Future Works

Enhancing electrochemical performance

While the TMV1cys provides an excellent template for high density immobilization of enzymes, the electrochemical conversion of the enzymatic activity into electrical currents is limited due to the lack of a proper interface between the catalytic reaction core and the conductive element. Future efforts in hosting conductive nanoparticles such as carbon nanotubes or Au nanoparticles into the TMV/CL/GOx conjugates can directly optimize electrochemical conversion of the enhanced and scalable enzymatic activity on chip, which is ultimately needed for demonstrating advanced enzyme-integrated bioelectronics performance. Alternatively, charge transfer mediating agents can be heterogeneously incorporated with GOx on TMV surface by targeting different functional receptors (e.g. Lys, Tyr) located at the inner channel using a different chemical conjugation route. This may allow channeling of the electrons, generated in the enzymatic reaction, to the electrode surface provided that the electron path/tunneling is available through the coat-protein layer. Lastly, for enhancing the bio-energy harvesting performance, incorporating oxygen reduction enzymes (e.g. laccase, bilirubin oxidase, ascorbate oxidase) instead of the Pt used in this work can increase the load potentials with higher oxygen reduction potentials. Combined with an

optimized fuel cell package providing continuous flow of fuels (glucose, oxygen) and a proton exchange membrane, the enhanced enzymatic activity on chip achieved in this work with 3D-EBP will translate into a biofuel cell generating practical power outputs.

Microfluidic system development incorporating enzymatic cascade

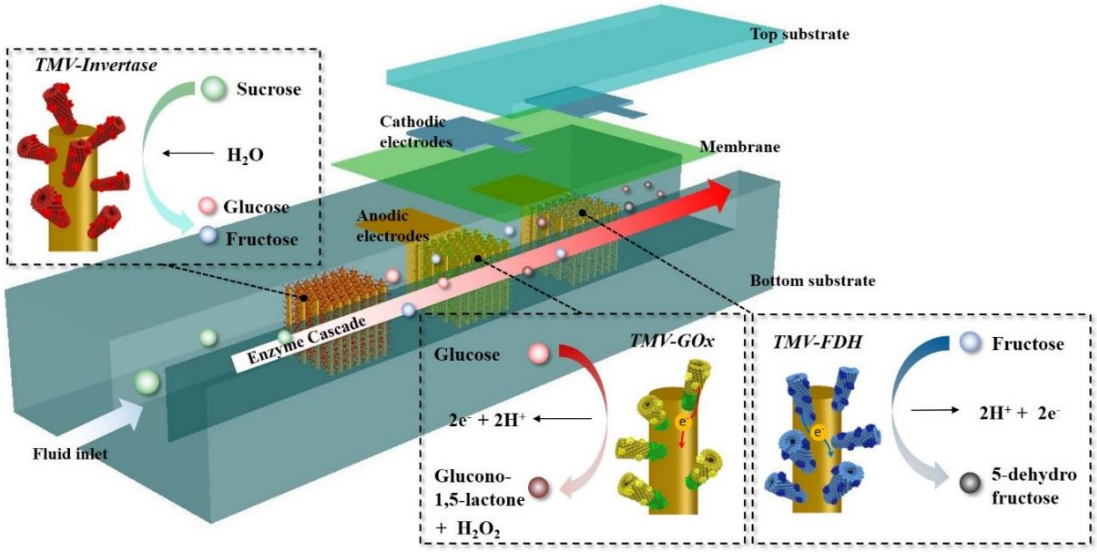

Figure 5-1. Exploded illustration of the potential microsystem integrating multiple 3-D enzymatic cascade forests in microfluidics for energy harvesting.

The ability to immobilize enzymes in a highly controlled fashion can be applied for developing microscale enzymatic cascade system on chip. Enzymatic cascades are essential in nature and are applied in a wide range of engineered applications.[8] Within a cell, the sequential catalytic reactions are critical in the production of numerous compounds and processes needed for producing energy and transferring signals. For research fields and industry, enzymatic cascade can provide an efficient and sustainable system for synthesis of new materials, therapeutics and energy. As the function of these cascades is known to highly depend on patterning of these participating enzymes with nano/micro scale precision, the 3D-EBP combined with the on-chip enzyme

immobilization technique brings an exciting opportunity for scalable patterning of enzymes with both micro and nanoscale precisions. Figure 5-1 illustrates a potential microfluidic energy harvesting system embedded with sequentially arranged enzymatic cascade forests. System packaging and optimization of control over the flows of mediators and fuels may be challenging, but more efficient bioenergy harvesting can be achieved by further inducing the oxidation of the fuels over the cascading reactions.

5.3. Conclusion

The revolutionary advancement in the development of miniaturized devices and systems equipped with novel functions derived from biomaterials made possible numerous applications, including biochemical sensors, gene delivery platforms, and bioenergy production, that ultimately lead to a greater understanding of biomolecular activities through on-chip characterizations. Over the past two decades, these advancements have accompanied a rapid evolution of bio-device integration strategies that permit the controlled deposition and patterning of functional biomaterials onto device surfaces. Particularly, recent efforts have demonstrated the integration of biomaterials with 3-D transducers as those structures at micro- and nano- scales, offering numerous beneficial properties compared to their two-dimensional counterparts providing enhanced performance or advanced modes of operation for bioelectronics at miniaturized scales.

This thesis research presents an innovative biofabrication technology, 3D-EBP, by identifying and addressing a fundamental challenge associated with an inherent wetting property of microdevice structures. The successful demonstration towards the development of next-generation enzyme-based bioelectronics, enabling scalable and

enhanced biocatalytic reactions on a chip, opens up new possibilities not only for the enzyme-based sensors and energy harvesting devices, but also for developing advanced bioanalytical platforms or biomimetic systems incorporating a three-dimensionally arranged bio/nano/micro environment.

References

1. Krogmann F, Mönch W, Zappe H. Electrowetting for tunable microoptics. *J Microelectromechanical Syst*. 2008;17(6):1501-1512. doi:10.1109/JMEMS.2008.2007256.
2. Traub MC, Longsine W, Truskett VN. Advances in Nanoimprint Lithography. *Annu Rev Chem Biomol Eng*. 2016;7:583-604. doi:10.1146/annurev-chembioeng-080615-034635.
3. Lee K-B, Park S-J, Mirkin CA, Smith JC, Mrksich M. Protein Nanoarrays Generated By Dip-Pen Nanolithography. *Science (80-)*. 2002;295(5560).
4. Liu Y, Kim E, Ghodssi R, Rubloff GW, Culver JN, Bentley WE, Payne GF. Biofabrication to build the biology-device interface. *Biofabrication*. 2010;2(2):022002. doi:10.1088/1758-5082/2/2/022002.
5. Wu LQ, Payne GF. Biofabrication: Using biological materials and biocatalysts to construct nanostructured assemblies. *Trends Biotechnol*. 2004;22(11):593-599.
6. Ricca E, Brucher B, Schrittwieser JH. Multi-enzymatic cascade reactions: Overview and perspectives. *Adv Synth Catal*. 2011;353(13):2239-2262. doi:10.1002/adsc.201100256.
7. Leech D, Kavanagh P, Schuhmann W. Enzymatic fuel cells: Recent progress. *Electrochim Acta*. 2012;84:223-234. doi:10.1016/j.electacta.2012.02.087.
8. Idan O, Hess H. Engineering enzymatic cascades on nanoscale scaffolds. *Curr Opin Biotechnol*. 2013;24(4):606-611. doi:10.1016/j.copbio.2013.01.003.
9. Katz E, Privman V. Enzyme-based logic systems for information processing. *Chem Soc Rev*. 2010;39(5):1835. doi:10.1039/b806038j.
10. Ferri S, Kojima K, Sode K. Review of glucose oxidases and glucose dehydrogenases: a bird's eye view of glucose sensing enzymes. *J Diabetes Sci Technol*. 2011;5(5):1068-1076. doi:10.1177/193229681100500507.
11. Renard E. Implantable continuous glucose sensors. *Curr Diabetes Rev*. 2008;4(3):169-174. http://www.ncbi.nlm.nih.gov/pubmed/18690897. Accessed February 1, 2017.
12. Whitehurst TK, Colvin a E, DeHennis a D, Makous JC, Mortellaro M, Rajaraman S, Schaefer J, Smith D, Tankiewicz S, Tymchyshyn O, Walters S, Wang X. Fluorescence-based implantable glucose sensor with smartphone interface. *Diabetologia*. 2012;55:S422-S423. http://ovidsp.ovid.com/ovidweb.cgi?T=JS&CSC=Y&NEWS=N&PAGE=fulltext&D=emed10&AN=70889050.
13. Munje RD, Muthukumar S, Prasad S. Lancet-free and label-free diagnostics of glucose in sweat using Zinc Oxide based flexible bioelectronics. *Sensors Actuators, B Chem*. 2017;238:482-490. doi:10.1016/j.snb.2016.07.088.
14. Garcia SO, Ulyanova Y V, Figueroa-Teran R, Bhatt KH, Singhal S, Atanassov P. Wearable Sensor System Powered by a Biofuel Cell for Detection of Lactate Levels in Sweat. *ECS J solid state Sci Technol JSS*. 2016;5(8):M3075-M3081. doi:10.1149/2.0131608jss.

15. Liu C, Sheng Y, Sun Y, Feng J, Wang S, Zhang J, Xu J, Jiang D. A glucose oxidase-coupled DNAzyme sensor for glucose detection in tears and saliva. *Biosens Bioelectron*. 2015;70:455-461. doi:10.1016/j.bios.2015.03.070.
16. Rasmussen M, Abdellaoui S, Minteer SD. Enzymatic biofuel cells: 30 years of critical advancements. *Biosens Bioelectron*. 2016;76:91-102. doi:10.1016/j.bios.2015.06.029.
17. Halámková L, Halámek J, Bocharova V, Szczupak A, Alfonta L, Katz E. Implanted biofuel cell operating in a living snail. *J Am Chem Soc*. 2012;134(11):5040-5043. doi:10.1021/ja211714w.
18. van Dongen SFM, Nallani M, Cornelissen JJLM, Nolte RJM, van Hest JCM. A Three-Enzyme Cascade Reaction through Positional Assembly of Enzymes in a Polymersome Nanoreactor. *Chem - A Eur J*. 2009;15(5):1107-1114. doi:10.1002/chem.200802114.
19. Shi L, Chu Z, Liu Y, Peng J, Jin W. Three-dimensional porous microarray of gold modified electrode for ultrasensitive and simultaneous assay of various cancer biomarkers. *J Mater Chem B*. 2014;2(18):2658-2665. doi:Doi 10.1039/C4tb00016a.
20. Branch B, Schei JL, Gupta G, Dattelbaum AM, Petsev DN, George JS. Micropillar Electrode Array: From Metal to Dielectric Interface. *IEEE Sens J*. 2015;15(9):4992-5000. doi:10.1109/JSEN.2015.2425305.
21. Liu J, Wang J, Wang T, Li D, Xi F, Wang J, Wang E. Three-dimensional electrochemical immunosensor for sensitive detection of carcinoembryonic antigen based on monolithic and macroporous graphene foam. *Biosens Bioelectron*. 2015;65:281-286. doi:10.1016/j.bios.2014.10.016.
22. Penmatsa V, Ruslinda AR, Beidaghi M, Kawarada H, Wang C. Platelet-derived growth factor oncoprotein detection using three-dimensional carbon microarrays. *Biosens Bioelectron*. 2013;39(1):118-123. doi:10.1016/j.bios.2012.06.055.
23. Inan H, Poyraz M, Inci F, Lifson MA, Baday M, Cunningham BT, Demirci U. Photonic crystals: emerging biosensors and their promise for point-of-care applications. *Chem Soc Rev*. 2017. doi:10.1039/C6CS00206D.
24. Gerasopoulos K, Pomerantseva E, McCarthy M, Brown A, Wang C, Culver J, Ghodssi R. Hierarchical three-dimensional microbattery electrodes combining bottom-up self-assembly and top-down micromachining. *ACS Nano*. 2012;6(7):6422-6432. doi:10.1021/nn301981p.
25. Armand M, Tarascon J-M. Building better batteries. *Nature*. 2008;451(7179):652-657. doi:10.1038/451652a.
26. Zhu Y, Yang B, Liu J, Wang X, Chen X, Yang C. An Integrated Flexible Harvester Coupled Triboelectric and Piezoelectric Mechanisms Using PDMS/MWCNT and PVDF. *J Microelectromechanical Syst*. 2015;24(3):513-515. doi:10.1109/JMEMS.2015.2404037.
27. Kovacs GTA, Maluf NI, Petersen KE. Bulk micromachining of silicon. *Proc IEEE*. 1998;86(8):1536-1551. doi:10.1109/5.704259.
28. Yeh JLA, Jiang H, Tien NC. Integrated polysilicon and DRIE bulk silicon micromachining for an electrostatic torsional actuator. *J Microelectromechanical Syst*. 1999;8(4):456-465. doi:10.1109/84.809061.

29. Adera S, Antao D, Raj R, Wang EN. Design of micropillar wicks for thin-film evaporation. *Int J Heat Mass Transf*. 2016;101:280-294. doi:10.1016/j.ijheatmasstransfer.2016.04.107.
30. Zhu Y, Zhengmao Lu, Antao DS, Hongxia Li, Zhang T, Wang EN. Model optimization of dry-out heat flux from micropillar wick structures. In: *2016 15th IEEE Intersociety Conference on Thermal and Thermomechanical Phenomena in Electronic Systems (ITherm)*. IEEE; 2016:372-377. doi:10.1109/ITHERM.2016.7517573.
31. Kumari N, Garimella S V. Electrowetting-induced dewetting transitions on superhydrophobic surfaces. *Langmuir*. 2011;27(17):10342-10346. doi:10.1021/la2027412.
32. Zhang X, Shi F, Niu J, Jiang Y, Wang Z. Superhydrophobic surfaces: from structural control to functional application. *J Mater Chem*. 2008;18(6):621-633. doi:10.1039/B711226B.
33. Inan H, Poyraz M, Inci F, Lifson MA, Baday M, Cunningham BT, Demirci U. Photonic crystals: emerging biosensors and their promise for point-of-care applications. *Chem Soc Rev*. 2017. doi:10.1039/C6CS00206D.
34. Fenzl C, Hirsch T, Wolfbeis OS. Photonic crystals for chemical sensing and biosensing. *Angew Chemie - Int Ed*. 2014;53(13):3318-3335. doi:10.1002/anie.201307828.
35. Aristov AI, Manousidaki M, Danilov A, Terzaki K, Fotakis C, Farsari M, Kabashin A V. 3D plasmonic crystal metamaterials for ultra-sensitive biosensing. *Sci Rep*. 2016;6:25380. doi:10.1038/srep25380.
36. Reif R, Fan A, Kuan-Neng Chen, Das S. Fabrication technologies for three-dimensional integrated circuits. In: *Proceedings International Symposium on Quality Electronic Design*. IEEE Comput. Soc; :33-37. doi:10.1109/ISQED.2002.996687.
37. Vaezi M, Seitz H, Yang S. A review on 3D micro-additive manufacturing technologies. *Int J Adv Manuf Technol*. 2013;67(5-8):1721-1754. doi:10.1007/s00170-012-4605-2.
38. Tuteja A, Choi W, Ma M, Mabry JM, Mazzella S a, Rutledge GC, McKinley GH, Cohen RE. Designing superoleophobic surfaces. *Science*. 2007;318(5856):1618-1622. doi:10.1126/science.1148326.
39. Bahadur V, Garimella S V. Electrowetting-based control of static droplet states on rough surfaces. *Langmuir*. 2007;23(9):4918-4924.
40. Zhao Y-P, Yuan Q. Statics and dynamics of electrowetting on pillar-arrayed surfaces at the nanoscale. *Nanoscale*. 2015;7(6):2561-2567. doi:10.1039/C4NR06759B.
41. Culver JN, Brown AD, Zang F, Gnerlich M, Gerasopoulos K, Ghodssi R. Plant virus directed fabrication of nanoscale materials and devices. *Virology*. 2015;479-480:200-212. doi:10.1016/j.virol.2015.03.008.
42. Ge P, Zhou ZH. Hydrogen-bonding networks and RNA bases revealed by cryo electron microscopy suggest a triggering mechanism for calcium switches. *Proc Natl Acad Sci*. 2011;108(23):9637-9642. doi:10.1073/pnas.1018104108.
43. Lomonossoff GP, Evans DJ. Applications of plant viruses in bionanotechnology. *Curr Top Microbiol Immunol*. 2014;375:61-87. doi:10.1007/82-2011-184.

44. Liu Z, Qiao J, Niu Z, Wang Q. Natural supramolecular building blocks: from virus coat proteins to viral nanoparticles. *Chem Soc Rev*. 2012;41(18):6178-6194. doi:10.1039/c2cs35108k.
45. Lee KL, Uhde-holzem K, Fischer R, Commandeur U, Steinmetz NF. Virus Hybrids as Nanomaterials. *Virus Hybrids as Nanomater Methods Protoc Methods Mol Biol*. 2014;1108:3-21. doi:10.1007/978-1-62703-751-8.
46. Lee LA, Niu Z, Wang Q. Viruses and virus-like protein assemblies-Chemically programmable nanoscale building blocks. *Nano Res*. 2009;2(5):349-364. doi:10.1007/s12274-009-9033-8.
47. Zdanowicz M, Chroboczek J. Virus-like particles as drug delivery vectors. *Acta Biochim Pol*. 2016;63(3):469-473. doi:10.18388/abp.2016_1275.
48. Frietze KM, Peabody DS, Chackerian B. Engineering virus-like particles as vaccine platforms. *Curr Opin Virol*. 2016;18:44-49. doi:10.1016/j.coviro.2016.03.001.
49. Brown AD, Naves L, Wang X, Ghodssi R, Culver JN. Carboxylate-Directed In Vivo Assembly of Virus-like Nanorods and Tubes for the Display of Functional Peptides and Residues. *Biomacromolecules*. 2013;14(9):3123-3129. doi:10.1021/bm400747k.
50. Czapar AE, Zheng YR, Riddell IA, Shukla S, Awuah SG, Lippard SJ, Steinmetz NF. Tobacco Mosaic Virus Delivery of Phenanthriplatin for Cancer therapy. *ACS Nano*. 2016;10(4):4119-4126. doi:10.1021/acsnano.5b07360.
51. Bruckman MA, Czapar AE, VanMeter A, Randolph LN, Steinmetz NF. Tobacco mosaic virus-based protein nanoparticles and nanorods for chemotherapy delivery targeting breast cancer. *Journal of Controlled Release*. 2015.
52. Bäcker M, Koch C, Eiben S, Geiger F, Eber F, Gliemann H, Poghossian A, Wege C, Schöning MJ. Tobacco mosaic virus as enzyme nanocarrier for electrochemical biosensors. *Sensors Actuators, B Chem*. 2017;238:716-722. doi:10.1016/j.snb.2016.07.096.
53. Leong HS, Steinmetz NF, Ablack A, Destito G, Zijlstra A, Stuhlmann H, Manchester M, Lewis JD. Intravital imaging of embryonic and tumor neovasculature using viral nanoparticles. *Nat Protoc*. 2010;5(8):1406-1417. doi:10.1038/nprot2010-103.
54. Lewis JD, Destito G, Zijlstra A, Gonzalez MJ, Quigley JP, Manchester M, Stuhlmann H. Viral nanoparticles as tools for intravital vascular imaging. *Nat Med*. 2006;12(3):354-360. doi:10.1038/nm1368.
55. Niehl A, Appaix F, Boscá S, van der Sanden B, Nicoud J-F, Bolze F, Heinlein M. Fluorescent Tobacco mosaic virus-Derived Bio-Nanoparticles for Intravital Two-Photon Imaging. *Front Plant Sci*. 2015;6:1244. doi:10.3389/fpls.2015.01244.
56. Alonso JM, Górzny ML, Bittner AM. The physics of tobacco mosaic virus and virus-based devices in biotechnology. *Trends Biotechnol*. 2013;31(9):530-538. doi:10.1016/j.tibtech.2013.05.013.
57. Kendall A, McDonald M, Stubbs G. Precise determination of the helical repeat of tobacco mosaic virus. *Virology*. 2007;369(1):226-227. doi:10.1016/j.virol.2007.08.013.

58. Yamanaka T, Komatani H, Meshi T, Naito S, Ishikawa M, Ohno T. Complete nucleotide sequence of the genomic RNA of tobacco mosaic virus strain Cg. *Virus Genes*. 1998;16(2):173-176. http://www.ncbi.nlm.nih.gov/pubmed/9608662.
59. Tran H, Killops KL, Campos LM. Advancements and challenges of patterning biomolecules with sub-50 nm features. *Soft Matter*. 2013;9:6578. doi:10.1039/c3sm00149k.
60. Blawas AS, Reichert WM. Protein patterning. *Biomaterials*. 1998;19(7-9):595-609. doi:10.1016/S0142-9612(97)00218-4.
61. Hlady V, Buijs J. Protein adsorption on solid surfaces. *Curr Opin Biotechnol*. 1996;7(1):72-77. doi:10.1016/S0958-1669(96)80098-X.
62. Mrksich M, Whitesides GM. USING SELF-ASSEMBLED MONOLAYERS TO UNDERSTAND THE MADE SURFACES WITH PROTEINS AND CELLS INTERACTIONS OF MAN. *Annu Rev Biophys Biomol Struct*. 1996:2555-2578.
63. Love JC, Estroff LA, Kriebel JK, Nuzzo RG, Whitesides GM. Self-assembled monolayers of thiolates on metals as a form of nanotechnology. *Chem Rev*. 2005;105(4):1103-1169. doi:10.1021/cr0300789.
64. Sassolas A, Blum LJ, Leca-Bouvier BD. Immobilization strategies to develop enzymatic biosensors. *Biotechnol Adv*. 2012;30(3):489-511. doi:10.1016/j.biotechadv.2011.09.003.
65. Wong LS, Khan F, Micklefield J. Selective covalent protein immobilization: Strategies and applications. *Chem Rev*. 2009;109(9):4025-4053. doi:10.1021/cr8004668.
66. Putzbach W, Ronkainen NJ. Immobilization techniques in the fabrication of nanomaterial-based electrochemical biosensors: a review. *Sensors (Basel)*. 2013;13(4):4811-4840. doi:10.3390/s130404811.
67. Nicosia C, Huskens J. Reactive self-assembled monolayers: from surface functionalization to gradient formation. *Mater Horiz*. 2014;1(1):32-45. doi:10.1039/C3MH00046J.
68. Mendes PM, Yeung CL, Preece JA. Bio-nanopatterning of Surfaces. *Nanoscale Res Lett*. 2007;2(8):373-384. doi:10.1007/s11671-007-9083-3.
69. Aydin D, Hirschfeld-Warneken VC, Louban I, Spatz JP. Micro- and Nanopatterning of Active Biomolecules and Cells. In: *Intelligent Surfaces in Biotechnology: Scientific and Engineering Concepts, Enabling Technologies, and Translation to Bio-Oriented Applications*. ; 2012:291-319. doi:10.1002/9781118181249.ch8.
70. Murphy S V, Atala A. 3D bioprinting of tissues and organs. *Nat Biotechnol*. 2014;32(8):773-785. doi:10.1038/nbt.2958.
71. Pati F, Gantelius J, Svahn HA. 3D Bioprinting of Tissue/Organ Models. *Angew Chemie - Int Ed*. 2016;55(15):4650-4665. doi:10.1002/anie.201505062.
72. Mooney JF, Hunt AJ, McIntosh JR, Liberko CA, Walba DM, Rogers CT. Patterning of functional antibodies and other proteins by photolithography of silane monolayers. *Proc Natl Acad Sci U S A*. 1996;93(22):12287-12291. doi:10.1073/pnas.93.22.12287.

73. Hahn MS, Taite LJ, Moon JJ, Rowland MC, Ruffino KA, West JL. Photolithographic patterning of polyethylene glycol hydrogels. *Biomaterials*. 2006;27(12):2519-2524. doi:10.1016/j.biomaterials.2005.11.045.
74. Makohliso SA, Giovangrandi L, Léonard D, Mathieu HJ, Ilegems M, Aebischer P. Application of Teflon-AF® thin films for bio-patterning of neural cell adhesion. *Biosens Bioelectron*. 1998;13(11):1227-1235. doi:10.1016/S0956-5663(98)00036-0.
75. Kumagai S, Yoshii S, Yamada K, Fujiwara I, Matsukawa N, Yamashita I. Nanopatterning of Vapor-deposited Aminosilane Film using EB Lithography for Ferritin Protein Adsorption. *J Photopolym Sci Technol*. 2005;18(4):495-500. doi:10.2494/photopolymer.18.495.
76. Pallandre A, De Meersman B, Oise Blondeau F, Nysten B, Jonas AM. Tuning the Orientation of an Antigen by Adsorption onto Nanostriped Templates. doi:10.1021/ja043656r.
77. Bergman AA, Buijs J, Herbig J, Mathes DT, Demarest JJ, Wilson CD, Reimann CT, Baragiola RA, Hu R, Oscarsson SO. Nanometer-scale arrangement of human serum albumin by adsorption on defect arrays created with a finely focused ion beam. *Langmuir*. 1998;14(24):6785-6788.
78. Falconnet D, Pasqui D, Park S, Eckert R, Schift H, Gobrecht J, Barbucci R, Textor M. A Novel Approach to Produce Protein Nanopatterns by Combining Nanoimprint Lithography and Molecular Self-Assembly. doi:10.1021/nl0489438.
79. Hoff JD, Cheng LJ, Meyhöfer E, Guo LJ, Hunt AJ. Nanoscale protein patterning by imprint lithography. *Nano Lett*. 2004;4(5):853-857. doi:10.1021/nl049758x.
80. Bernard a, Renault JP, Michel B, Bosshard HR, Delamarche E. Microcontact printing of proteins. *Adv Mater*. 2000;12(14):1067-1070. doi:Doi 10.1002/1521-4095(200007)12:14<1067::Aid-Adma1067>3.0.Co;2-M.
81. Kane RS, Takayama S, Ostuni E, Ingber DE, Whitesides GM. Patterning proteins and cells using soft lithography. *Biomaterials*. 1999;20(23-24):2363-2376. doi:10.1016/S0142-9612(99)00165-9.
82. Liao W-S, Cheunkar S, Cao HH, Bednar HR, Weiss PS, Andrews AM. Subtractive Patterning via Chemical Lift-Off Lithography. *Science (80-).* 2012;337(6101):1517-1521. doi:10.1126/science.1221774.
83. Li HW, Muir BVO, Fichet G, Huck WTS. Nanocontact printing: A route to sub-50-nm-scale chemical and biological patterning. *Langmuir*. 2003;19(6):1963-1965. doi:10.1021/la0269098.
84. Piner RD. "Dip-Pen" Nanolithography. *Science (80-).* 1999;283(5402):661-663. doi:10.1126/science.283.5402.661.
85. and SX, Liu* G. Nanometer-Scale Fabrication by Simultaneous Nanoshaving and Molecular Self-Assembly. 1997. doi:10.1021/LA962029F.
86. Jinjun Shi, Jixin Chen and, Cremer* PS. Sub-100 nm Patterning of Supported Bilayers by Nanoshaving Lithography. 2008. doi:10.1021/JA077730S.
87. Xu S, Miller S, Laibinis PE, Liu GY. Fabrication of nanometer scale patterns within self-assembled monolayers by nanografting. *Langmuir*. 1999;15(21):7244-7251. doi:10.1021/la9906727.

88. Ying Hu †, Aditi Das †, Michael H. Hecht *,†,‡ and, Giacinto Scoles* †,‡,§. Nanografting De Novo Proteins onto Gold Surfaces. 2005. doi:10.1021/LA046857H.
89. Kumar A, Whitesides GM. Features of gold having micrometer to centimeter dimensions can be formed through a combination of stamping with an elastomeric stamp and an alkanethiol "'ink"' followed by chemical etching. *Appl Phys Lett*. 1993;63(14):2002-2004. doi:10.1063/1.110628.
90. Quist AP, Pavlovic E, Oscarsson S. Recent advances in microcontact printing. *Anal Bioanal Chem*. 2005;381(3):591-600. doi:10.1007/s00216-004-2847-z.
91. Alom Ruiz S, Chen CS. Microcontact printing: A tool to pattern. *Soft Matter*. 2007;3(2):168-177. doi:10.1039/B613349E.
92. Renault JP, Bernard A, Bietsch A, Michel B, Bosshard HR, Delamarche E, Kreiter M, Hecht B, Wild UP. Fabricating arrays of single protein molecules on glass using microcontact printing. *J Phys Chem B*. 2003;107(3):703-711. doi:10.1021/jp0263424.
93. Saravia V, Küpcü S, Nolte M, Huber C, Pum D, Fery A, Sleytr UB, Toca-Herrera JL. Bacterial protein patterning by micro-contact printing of PLL-g-PEG. *J Biotechnol*. 2007;130(3):247-252. doi:10.1016/j.jbiotec.2007.04.017.
94. Takulapalli BR, Morrison ME, Gu J, Zhang P. A nanocontact printing system for sub-100 nm aligned patterning. *Nanotechnology*. 2011;22(28):285302. doi:10.1088/0957-4484/22/28/285302.
95. Salaita K, Lee SW, Wang X, Huang L, Dellinger TM, Liu C, Mirkin CA. Sub-100 nm, Centimeter-Scale, Parallel Dip-Pen Nanolithography. *Small*. 2005;1(10):940-945. doi:10.1002/smll.200500202.
96. Eichelsdoerfer DJ, Liao X, Cabezas MD, Morris W, Radha B, Brown KA, Giam LR, Braunschweig AB, Mirkin CA. Large-area molecular patterning with polymer pen lithography. *Nat Protoc*. 2013;8(12):2548-2560. doi:10.1038/nprot.2013.159.
97. Aricò AS, Bruce P, Scrosati B, Tarascon J-M, van Schalkwijk W. Nanostructured materials for advanced energy conversion and storage devices. *Nat Mater*. 2005;4(5):366-377. doi:10.1038/nmat1368.
98. Chen X, Van P??e KH. Catalytic mechanisms, basic roles, and biotechnological and environmental significance of halogenating enzymes. *Acta Biochim Biophys Sin (Shanghai)*. 2008;40(3):183-193. doi:10.1111/j.1745-7270.2008.00390.x.
99. Li C, Wang Z, Wang P-I, Peles Y, Koratkar N, Peterson GP. Nanostructured Copper Interfaces for Enhanced Boiling. *Small*. 2008;4(8):1084-1088. doi:10.1002/smll.200700991.
100. Kordás K, Pap AE, Vähäkangas J, Uusimäki A, Leppävuori S. Carbon nanotube synthesis on oxidized porous silicon. *Appl Surf Sci*. 2005;252(5):1471-1475. doi:10.1016/j.apsusc.2005.02.120.
101. Sun S, Yang D, Zhang G, Sacher E, Dodelet J-P. Synthesis and Characterization of Platinum Nanowire–Carbon Nanotube Heterostructures. *Chem Mater*. 2007;19(26):6376-6378. doi:10.1021/cm7022949.
102. Bin Xiang †, Pengwei Wang ‡, Xingzheng Zhang ‡, Shadi. A. Dayeh †, David P. R. Aplin †, Cesare Soci †, Dapeng Yu ‡ and, Deli Wang* †. Rational

Synthesis of p-Type Zinc Oxide Nanowire Arrays Using Simple Chemical Vapor Deposition. 2006. doi:10.1021/NL062410C.
103. Wang JH, Su PY, Lu MY, Chen LJ, Chen CH, Chu CJ. Synthesis of Cu Nanotubes with Silicon Oxide Nanowire Templates by MOCVD. *Electrochem Solid-State Lett*. 2005;8(1):C9. doi:10.1149/1.1836112.
104. Feng X, Shankar K, Varghese OK, Paulose M, Latempa TJ, Grimes CA. Vertically aligned single crystal TiO 2 nanowire arrays grown directly on transparent conducting oxide coated glass: Synthesis details and applications. *Nano Lett*. 2008;8(11):3781-3786. doi:10.1021/nl802096a.
105. Ghoshal T, Biswas S, Kar S, Dev A, Chakrabarti S, Chaudhuri S. Direct synthesis of ZnO nanowire arrays on Zn foil by a simple thermal evaporation process. *Nanotechnology*. 2008;19(6):65606. doi:10.1088/0957-4484/19/6/065606.
106. O'Brien S, Brus L, Murray CB. Synthesis of monodisperse nanoparticles of barium titanate: Toward a generalized strategy of oxide nanoparticle synthesis. *J Am Chem Soc*. 2001;123(48):12085-12086. doi:10.1021/ja011414a.
107. Kum MC, Yoo BY, Rheem YW, Bozhilov KN, Chen W, Mulchandani A, Myung N V. Synthesis and characterization of cadmium telluride nanowire. *Nanotechnology*. 2008;19(32):325711. doi:10.1088/0957-4484/19/32/325711.
108. Calò A, Eiben S, Okuda M, Bittner AM. Nanoscale device architectures derived from biological assemblies: The case of tobacco mosaic virus and (apo)ferritin. *Jpn J Appl Phys*. 2016;55(3S2):03DA01. doi:10.7567/JJAP.55.03DA01.
109. Shenton W, Mann S, Douglas T, Young M, Stubbs G. {I}norganic-organic nanotube composites from template mineralization of tobacco mosaic virus. *Adv Mater*. 1999;11(3):253-256. doi:10.1002/(SICI)1521-4095(199903)11.
110. Mato Knez †, Alexander M. Bittner *,†, Fabian Boes ‡, Christina Wege ‡, Holger Jeske ‡, E. Maiβ § and, Kern† K. Biotemplate Synthesis of 3-nm Nickel and Cobalt Nanowires. 2003. doi:10.1021/NL0342545.
111. Dujardin E, Peet C, Stubbs G, Culver JN, Mann S. Organization of metallic nanoparticles using tobacco mosaic virus templates. *Nano Lett*. 2003;3(3):413-417. doi:Doi 10.1021/Nl034004o.
112. Lee S-Y, Royston E, Culver JN, Harris MT. Improved metal cluster deposition on a genetically engineered tobacco mosaic virus template. *Nanotechnology*. 2005;16(7):S435. doi:10.1088/0957-4484/16/7/019.
113. Vericat C, Vela ME, Corthey G, Pensa E, Cortés E, Fonticelli MH, Ibañez F, Benitez GE, Carro P, Salvarezza RC, Cortes E, Fonticelli MH, Ibanez F, Benitez GE, Carro P, Salvarezza RC. Self-assembled monolayers of thiolates on metals: a review article on sulfur-metal chemistry and surface structures. *RSC Adv*. 2014;4(53):27730-27754. doi:10.1039/C4RA04659E.
114. Royston E, Ghosh A, Kofinas P, Harris MT, Culver JN. Self-assembly of virus-structured high surface area nanomaterials and their application as battery electrodes. *Langmuir*. 2008;24(3):906-912. doi:10.1021/la7016424.
115. Gerasopoulos K, McCarthy M, Royston E, N Culver J, Ghodssi R. Nanostructured nickel electrodes using the Tobacco mosaic virus for microbattery applications. *J Micromechanics Microengineering*. 2008;18(10):104003. doi:10.1088/0960-1317/18/10/104003.

116. Gerasopoulos K, McCarthy M, Royston E, Culver JN, Ghodssi R. Microbatteries with tobacco mosaic virus templated electrodes. In: *Proceedings of the IEEE International Conference on Micro Electro Mechanical Systems (MEMS)*. ; 2008:960-963. doi:10.1109/MEMSYS.2008.4443817.
117. Gerasopoulos K, Chen XL, Culver J, Wang CS, Ghodssi R. Self-assembled Ni/TiO2 nanocomposite anodes synthesized via electroless plating and atomic layer deposition on biological scaffolds. *Chem Commun*. 2010;46(39):7349-7351. doi:Doi 10.1039/C0cc01689f.
118. Chen X, Gerasopoulos K, Guo J, Brown A, Ghodssi R, Culver JN, Wang C. High rate performance of virus enabled 3D n-type Si anodes for lithium-ion batteries. *Electrochim Acta*. 2011;56(14):5210-5213. doi:10.1016/j.electacta.2011.03.037.
119. Gnerlich M, Ben-Yoav H, Culver JN, Ketchum DR, Ghodssi R. Selective deposition of nanostructured ruthenium oxide using Tobacco mosaic virus for micro-supercapacitors in solid Nafion electrolyte. *J Power Sources*. 2015;293:649-656. doi:10.1016/j.jpowsour.2015.05.053.
120. Xia X, Tu J, Zhang Y, Wang X, Gu C, Zhao X, Fan HJ. High-Quality Metal Oxide Core/Shell Nanowire Arrays on Conductive Substrates for Electrochemical Energy Storage. *ACS Nano*. 2012;6(6):5531-5538. doi:10.1021/nn301454q.
121. Chen X, Gerasopoulos K, Guo J, Brown A, Wang C, Ghodssi R, Culver JN. Virus-enabled silicon anode for lithium-ion batteries. *ACS Nano*. 2010;4(9):5366-5372. doi:10.1021/nn100963j.
122. Atanasova P, Rothenstein D, Schneider JJ, Hoffmann RC, Dilfer S, Eiben S, Wege C, Jeske H, Bill J. Virus-templated synthesis of ZnO nanostructures and formation of field-effect transistors. *Adv Mater*. 2011;23(42):4918-4922. doi:10.1002/adma.201102900.
123. Tseng RJ, Tsai C, Ma L, Ouyang J, Ozkan CS, Yang Y. Digital memory device based on tobacco mosaic virus conjugated with nanoparticles. *Nat Nanotechnol*. 2006;1(1):72-77. doi:10.1038/nnano.2006.55.
124. Atanasova P, Stitz N, Sanctis S, Maurer JHM, Hoffmann RC, Eiben S, Jeske H, Schneider JJ, Bill J. Genetically improved monolayer-forming tobacco mosaic viruses to generate nanostructured semiconducting bio/inorganic hybrids. *Langmuir*. 2015;31(13):3897-3903. doi:10.1021/acs.langmuir.5b00700.
125. Bruckman MA, Liu J, Koley G, Li Y, Benicewicz B, Niu Z, Wang Q. Tobacco mosaic virus based thin film sensor for detection of volatile organic compounds. *J Mater Chem*. 2010;20(27):5715-5719. doi:10.1039/C0JM00634C.
126. Chiang C-Y, Epstein J, Brown A, Munday JN, Culver JN, Ehrman S. Biological Templates for Antireflective Current Collectors for Photoelectrochemical Cell Applications. *Nano Lett*. 2012;12(11):6005-6011. doi:10.1021/nl303579z.
127. Liu R, Vaishnav RA, Roberts AM, Friedland RP. Humans Have Antibodies against a Plant Virus: Evidence from Tobacco Mosaic Virus. *PLoS One*. 2013;8(4). doi:10.1371/journal.pone.0060621.
128. Bruckman MA, Randolph LN, VanMeter A, Hern S, Shoffstall AJ, Taurog RE, Steinmetz NF. Biodistribution, pharmacokinetics, and blood compatibility of

native and PEGylated tobacco mosaic virus nano-rods and -spheres in mice. *Virology*. 2014;449:163-173. doi:10.1016/j.virol.2013.10.035.
129. Zang F, Gerasopoulos K, Fan XZ, Brown AD, Culver JN, Ghodssi R. Real-time monitoring of macromolecular biosensing probe self-assembly and on-chip ELISA using impedimetric microsensors. *Biosens Bioelectron*. 2016;81:401-407. doi:10.1016/j.bios.2016.03.019.
130. Zang F, Gerasopoulos K, Fan XZ, Brown AD, Culver JN, Ghodssi R. An electrochemical sensor for selective TNT sensing based on Tobacco mosaic virus-like particle binding agents. *Chem Commun*. 2014;50(85):12977-12980. doi:10.1039/C4CC06735E.
131. Zang F, Gerasopoulos K, Brown AD, Culver JN, Ghodssi R. Capillary microfluidics-assembled virus-like particle bio-nano-receptor interfaces for label-free biosensing. *ACS Appl Mater Interfaces*. February 2017:acsami.6b14045. doi:10.1021/acsami.6b14045.
132. Klug A. The tobacco mosaic virus particle: structure and assembly. *Philos Trans R Soc Lond B Biol Sci*. 1999;354(1383):531-535. doi:10.1098/rstb.1999.0404.
133. Mohan K, Weiss GA. Chemically Modifying Viruses for Diverse Applications. *ACS Chem Biol*. 2016;11(5):1167-1179. doi:10.1021/acschembio.6b00060.
134. Fan XZ, Naves L, Siwak NP, Brown A, Culver J, Ghodssi R. Integration of genetically modified virus-like-particles with an optical resonator for selective bio-detection. *Nanotechnology*. 2015;26(20):205501. http://stacks.iop.org/0957-4484/26/i=20/a=205501.
135. Zang F, Gerasopoulos K, Brown AD, Culver JN, Ghodssi R. Capillary Microfluidics-Assembled Virus-like Particle Bionanoreceptor Interfaces for Label-Free Biosensing. *ACS Appl Mater Interfaces*. March 2017:acsami.6b14045. doi:10.1021/acsami.6b14045.
136. Koch C, Wabbel K, Eber FJ, Krolla-Sidenstein P, Azucena C, Gliemann H, Eiben S, Geiger F, Wege C. Modified TMV Particles as Beneficial Scaffolds to Present Sensor Enzymes. *Front Plant Sci*. 2015;6(December):1137. doi:10.3389/fpls.2015.01137.
137. Saile V. Introduction: LIGA and Its Applications. *LIGA Its Appl*. 2009;7:1-10. doi:10.1002/9783527622573.ch1.
138. Laermer F, Franssila S, Sainiemi L, Kolari K. Deep Reactive Ion Etching. In: *Handbook of Silicon Based MEMS Materials and Technologies*. ; 2010:349-374. doi:10.1016/B978-0-8155-1594-4.00023-1.
139. Laza SC, Polo M, Neves AAR, Cingolani R, Camposeo A, Pisignano D. Two-photon continuous flow lithography. *Adv Mater*. 2012;24(10):1304-1308. doi:10.1002/adma.201103357.
140. Campbell TA, Ivanova OS. 3D printing of multifunctional nanocomposites. *Nano Today*. 2013;8(2):119-120. doi:10.1016/j.nantod.2012.12.002.
141. Kazemi SH, Shanehsaz M, Ghaemmaghami M. Non-Faradaic electrochemical impedance spectroscopy as a reliable and facile method: Determination of the potassium ion concentration using a guanine rich aptasensor. *Mater Sci Eng C*. 2015;52:151-154. doi:10.1016/j.msec.2015.03.058.

142. Diculescu VC, Chiorcea-Paquim AM, Oliveira-Brett AM. Applications of a DNA-electrochemical biosensor. *TrAC - Trends Anal Chem*. 2016;79:23-36. doi:10.1016/j.trac.2016.01.019.
143. Gruber K, Horlacher T, Castelli R, Mader A, Seeberger PH, Hermann BA. Cantilever array sensors detect specific carbohydrate-protein interactions with picomolar sensitivity. *ACS Nano*. 2011;5(5):3670-3678. doi:10.1021/nn103626q.
144. Babacan S, Pivarnik P, Letcher S, Rand AG. Evaluation of antibody immobilization methods for piezoelectric biosensor application. *Biosens Bioelectron*. 2000;15(11-12):615-621. doi:10.1016/S0956-5663(00)00115-9.
145. Si P, Huang Y, Wang T, Ma J. Nanomaterials for electrochemical non-enzymatic glucose biosensors. *RSC Adv*. 2013;3(11):3487. doi:10.1039/c2ra22360k.
146. Pletcher D. Electrocatalysis: present and future. *J Appl Electrochem*. 1984;14(4):403-415. doi:10.1007/BF00610805.
147. Burke LD. Premonolayer oxidation and its role in electrocatalysis. *Electrochim Acta*. 1994;39(11-12):1841-1848. doi:10.1016/0013-4686(94)85173-5.
148. Li Z, Chen Y, Xin Y, Zhang Z. Sensitive electrochemical nonenzymatic glucose sensing based on anodized CuO nanowires on three-dimensional porous copper foam. *Sci Rep*. 2015;5(October):16115. doi:10.1038/srep16115.
149. Kannan P, Maiyalagan T, Marsili E, Ghosh S, Niedziolka-Jönsson J, Jönsson-Niedziolka M. Hierarchical 3-dimensional nickel–iron nanosheet arrays on carbon fiber paper as a novel electrode for non-enzymatic glucose sensing. 2016. doi:10.1039/c5nr06802a.
150. Cherevko S, Chung CH. Gold nanowire array electrode for non-enzymatic voltammetric and amperometric glucose detection. *Sensors Actuators, B Chem*. 2009;142(1):216-223. doi:10.1016/j.snb.2009.07.023.
151. Liu F, Piao Y, Choi JS, Seo TS. Three-dimensional graphene micropillar based electrochemical sensor for phenol detection. *Biosens Bioelectron*. 2013;50:387-392. doi:10.1016/j.bios.2013.06.055.
152. Bratov A, Ramón-Azcón J, Abramova N, Merlos A, Adrian J, Sánchez-Baeza F, Marco MP, Domínguez C. Three-dimensional interdigitated electrode array as a transducer for label-free biosensors. *Biosens Bioelectron*. 2008;24(4):729-735. doi:10.1016/j.bios.2008.06.057.
153. Voitechovič E, Bratov A, Abramova N, Razumienė J, Kirsanov D, Legin A, Lakshmi D, Piletsky S, Whitcombe M, Ivanova-Mitseva PK. Development of label-free impedimetric platform based on new conductive polyaniline polymer and three-dimensional interdigitated electrode array for biosensor applications. *Electrochim Acta*. 2015;173:59-66. doi:10.1016/j.electacta.2015.05.011.
154. Guimerà A, Gabriel G, Prats-Alfonso E, Abramova N, Bratov A, Villa R. Effect of surface conductivity on the sensitivity of interdigitated impedimetric sensors and their design considerations. *Sensors Actuators, B Chem*. 2015;207(PB):1010-1018. doi:10.1016/j.snb.2014.10.134.
155. Amato L, Heiskanen A, Hansen R, Gammelgaard L, Rindzevicius T, Tenje M, Emnéus J, Keller SS. Dense high-aspect ratio 3D carbon pillars on interdigitated microelectrode arrays. *Carbon N Y*. 2015;94:792-803. doi:10.1016/j.carbon.2015.06.014.

156. Kilchenmann SC, Rollo E, Bianchi E, Guiducci C. Metal-coated silicon micropillars for freestanding 3D-electrode arrays in microchannels. *Sensors Actuators, B Chem*. 2013;185:713-719. doi:10.1016/j.snb.2013.05.037.
157. Kamath RR, Madou MJ. Three-dimensional carbon interdigitated electrode arrays for redox-amplification. *Anal Chem*. 2014;86(6):2963-2971. doi:10.1021/ac4033356.
158. Kim BY, Sohn IY, Lee D, Han GS, Lee WI, Jung HS, Lee NE. Ultrarapid and ultrasensitive electrical detection of proteins in a three-dimensional biosensor with high capture efficiency. *Nanoscale*. 2015;7(21):9844-9851. doi:10.1039/c5nr00909j.
159. Goldberger J, Hochbaum AI, Fan R, Yang P. Silicon vertically integrated nanowire field effect transistors. *Nano Lett*. 2006;6(5):973-977. doi:10.1021/nl060166j.
160. Zhu S, Li H, Yang M, Pang SW. High sensitivity plasmonic biosensor based on nanoimprinted quasi 3D nanosquares for cell detection. *Nanotechnology*. 2016;27(29):295101. doi:10.1088/0957-4484/27/29/295101.
161. Li M, Cushing SK, Zhang J, Suri S, Evans R, Petros WP, Gibson LF, Ma D, Liu Y, Wu N. Three-dimensional hierarchical plasmonic nano-architecture enhanced surface-enhanced Raman scattering immunosensor for cancer biomarker detection in blood plasma. *ACS Nano*. 2013;7(6):4967-4976. doi:10.1021/nn4018284.
162. Ispas CR, Crivat G, Andreescu S. Review: Recent Developments in Enzyme-Based Biosensors for Biomedical Analysis. *Anal Lett*. 2012;45(2-3):168-186. doi:10.1080/00032719.2011.633188.
163. Falk M, Blum Z, Shleev S. Direct electron transfer based enzymatic fuel cells. In: *Electrochimica Acta*. Vol 82. ; 2012:191-202. doi:10.1016/j.electacta.2011.12.133.
164. Fan XZ, Pomerantseva E, Gnerlich M, Brown A, Gerasopoulos K, McCarthy M, Culver J, Ghodssi R. Tobacco mosaic virus: A biological building block for micro/nano/bio systems. *J Vac Sci Technol A Vacuum, Surfaces, Film*. 2013;31(5):050815. doi:10.1116/1.4816584.
165. Gerasopoulos K, McCarthy M, Banerjee P, Fan X, Culver JN, Ghodssi R. Biofabrication methods for the patterned assembly and synthesis of viral nanotemplates. *Nanotechnology*. 2010;21(5):055304. doi:10.1088/0957-4484/21/5/055304.
166. Chen H, Cong TN, Yang W, Tan C, Li Y, Ding Y. Progress in electrical energy storage system: A critical review. *Prog Nat Sci*. 2009;19(3):291-312. doi:10.1016/j.pnsc.2008.07.014.
167. Chen SM, Ramachandran R, Mani V, Saraswathi R. Recent advancements in electrode materials for the high-performance electrochemical supercapacitors: A review. *Int J Electrochem Sci*. 2014;9(8):4072-4085.
168. Wang G, Zhang L, Zhang J. A review of electrode materials for electrochemical supercapacitors. *Chem Soc Rev*. 2012;41:797. doi:10.1039/c1cs15060j.
169. Caballero A, Hernán L, Morales J, González Z, Sánchez-Herencia AJ, Ferrari B. A high-capacity anode for lithium batteries consisting of mesoporous NiO

nanoplatelets. *Energy and Fuels*. 2013;27(9):5545-5551. doi:10.1021/ef400797r.
170. Luan F, Wang G, Ling Y, Lu X, Wang H, Tong Y, Liu X-X, Li Y. High energy density asymmetric supercapacitors with a nickel oxide nanoflake cathode and a 3D reduced graphene oxide anode. *Nanoscale*. 2013;5:7984-7990. doi:10.1039/c3nr02710d.
171. Yue GH, Zhao YC, Wang CG, Zhang XX, Zhang XQ, Xie QS. Flower-like nickel oxide nanocomposites anode materials for excellent performance lithium-ion batteries. *Electrochim Acta*. 2015;152:315-322. doi:10.1016/j.electacta.2014.11.177.
172. Fan Z, Liang J, Yu W, Ding S, Cheng S, Yang G, Wang Y, Xi Y, Xi K, Kumar RV. Ultrathin NiO nanosheets anchored on a highly ordered nanostructured carbon as an enhanced anode material for lithium ion batteries. *Nano Energy*. 2015;16:152-162. doi:10.1016/j.nanoen.2015.06.009.
173. Brousse T, Belanger D, Long JW. To Be or Not To Be Pseudocapacitive? *J Electrochem Soc*. 2015;162(5):A5185-A5189. doi:10.1149/2.0201505jes.
174. Zou Y, Wang Y. NiO nanosheets grown on graphene nanosheets as superior anode materials for Li-ion batteries. *Nanoscale*. 2011;3:2615-2620. doi:10.1039/c1nr10070j.
175. Hasan M, Jamal M, Razeeb KM. Coaxial NiO/Ni nanowire arrays for high performance pseudocapacitor applications. *Electrochim Acta*. 2012;60:193-200. doi:10.1016/j.electacta.2011.11.039.
176. Kim J-H, Kang SH, Zhu K, Kim JY, Neale NR, Frank AJ. Ni-NiO core-shell inverse opal electrodes for supercapacitors. *Chem Commun (Camb)*. 2011;47(18):5214-5216. doi:10.1039/c0cc05191h.
177. Yang L, Qian L, Tian X, Li J, Dai J, Guo Y, Xiao D. Hierarchically porous nickel oxide nanosheets grown on nickel foam prepared by one-step in situ anodization for high-performance supercapacitors. *Chem - An Asian J*. 2014;9(6):1579-1585. doi:10.1002/asia.201402175.
178. Wang H, Yi H, Chen X, Wang X. Facile synthesis of a nano-structured nickel oxide electrode with outstanding pseudocapacitive properties. *Electrochim Acta*. 2013;105:353-361. doi:10.1016/j.electacta.2013.05.031.
179. Dai X, Chen D, Fan H, Zhong Y, Chang L, Shao H, Wang J, Zhang J, Cao CN. Ni(OH)2/NiO/Ni composite nanotube arrays for high-performance supercapacitors. *Electrochim Acta*. 2015;154:128-135. doi:10.1016/j.electacta.2014.12.066.
180. Yu L, Zhang G, Yuan C, Lou XWD. Hierarchical NiCo2O4@MnO2 core-shell heterostructured nanowire arrays on Ni foam as high-performance supercapacitor electrodes. *Chem Commun*. 2013;49(2):137-139. doi:10.1039/c2cc37117k.
181. Mansour AN. Characterization of NiO by XPS. *Surf Sci Spectra*. 1994;3(3):231. doi:10.1116/1.1247751.
182. Kumari SV, Natarajan M, Vaidyan VK, Koshy P. Surface oxidation of nickel thin films. *J Mater Sci Lett*. 1992;11(11):761-762. doi:10.1007/BF00729484.
183. De Los Santos Valladares L, Ionescu A, Holmes S, Barnes CHW, Bustamante Domínguez A, Avalos Quispe O, González JC, Milana S, Barbone M, Ferrari

AC, Ramos H, Majima Y. Characterization of Ni thin films following thermal oxidation in air. *J Vac Sci Technol B, Nanotechnol Microelectron Mater Process Meas Phenom*. 2014;32(5):051808. doi:10.1116/1.4895846.

184. Lu Z, Chang Z, Liu J, Sun X. Stable ultrahigh specific capacitance of NiO nanorod arrays. *Nano Res*. 2011;4(7):658-665. doi:10.1007/s12274-011-0121-1.
185. Zhao D, Bao S, Zhou W, Li H. Preparation of hexagonal nanoporous nickel hydroxide film and its application for electrochemical capacitor. 2007;9:869-874. doi:10.1016/j.elecom.2006.11.030.
186. Wu C, Deng S, Wang H, Sun Y, Liu J, Yan H. Preparation of novel three-dimensional NiO/ultrathin derived graphene hybrid for supercapacitor applications. *ACS Appl Mater Interfaces*. 2014;6(2):1106-1112. doi:10.1021/am404691w.
187. Lee JW, Ahn T, Kim JH, Ko JM, Kim JD. Nanosheets based mesoporous NiO microspherical structures via facile and template-free method for high performance supercapacitors. *Electrochim Acta*. 2011;56(13):4849-4857. doi:10.1016/j.electacta.2011.02.116.
188. de Gennes PG. Wetting: statics and dynamics. *Rev Mod Phys*. 1985;57(3):827-863. doi:10.1103/RevModPhys.57.827.
189. Lafuma A, Quéré D. Superhydrophobic states. *Nat Mater*. 2003;2(7):457-460. doi:10.1038/nmat924.
190. Nosonovsky M, Bhushan B. Biologically Inspired Surfaces: Broadening the Scope of Roughness**. *Adv Funct Mater*. 2008;18(6):843-855. doi:10.1002/adfm.200701195.
191. Dai W, Zhao Y-P. An Electrowetting Model for Rough Surfaces Under Low Voltage. *J Adhes Sci Technol*. 2008;22(July 2013):217-229. doi:10.1163/156856108X306966.
192. Wenzel RN. Resistance of solid surfaces to wetting by water. *J Ind Eng Chem (Washington, D C)*. 1936;28:988-994. doi:10.1021/ie50320a024.
193. B D Cassie BA, Baxter S. WETTABILITY OF POROUS SURFACES.
194. Marmur* A. Wetting on Hydrophobic Rough Surfaces: To Be Heterogeneous or Not To Be? 2003. doi:10.1021/LA0344682.
195. Bae GY, Min BG, Jeong YG, Lee SC, Jang JH, Koo GH. Superhydrophobicity of cotton fabrics treated with silica nanoparticles and water-repellent agent. *J Colloid Interface Sci*. 2009;337(1):170-175. doi:10.1016/j.jcis.2009.04.066.
196. Fürstner R, Barthlott W, Neinhuis C, Walzel P. Wetting and self-cleaning properties of artificial superhydrophobic surfaces. *Langmuir*. 2005;21(3):956-961. doi:10.1021/la0401011.
197. Liu P, Cao L, Zhao W, Xia Y, Huang W, Li Z. Insights into the superhydrophobicity of metallic surfaces prepared by electrodeposition involving spontaneous adsorption of airborne hydrocarbons. *Appl Surf Sci*. 2015;324:576-583. doi:10.1016/j.apsusc.2014.10.170.
198. Xi W, Qiao Z, Zhu C, Jia A, Li M. The preparation of lotus-like super-hydrophobic copper surfaces by electroplating. *Appl Surf Sci*. 2009;255(9):4836-4839. doi:10.1016/j.apsusc.2008.12.012.

199. Abdelsalam ME, Bartlett PN, Kelf T, Baumberg J. Wetting of regularly structured gold surfaces. *Langmuir*. 2005;21(5):1753-1757. doi:10.1021/la047468q.
200. Zhang W, Yu Z, Chen Z, Li M. Preparation of super-hydrophobic Cu/Ni coating with micro-nano hierarchical structure. *Mater Lett*. 2012;67(1):327-330. doi:10.1016/j.matlet.2011.09.114.
201. Callies M, Chen Y, Marty F, Pépin A, Quéré D. Microfabricated textured surfaces for super-hydrophobicity investigations. 2005. doi:10.1016/j.mee.2004.12.093.
202. Hideo Nakae, Ryuichi Inui, Yosuke Hirata, Hiroyuki Saito. Effects of surface roughness on wettability. *Acta Mater*. 1998;46(7):2313-2318. doi:10.1016/S1359-6454(98)80012-8.
203. Mugele F, Baret J-C. Electrowetting: from basics to applications. *J Phys Condens Matter*. 2005;17(28):R705-R774. doi:10.1088/0953-8984/17/28/R01.
204. Kuiper S, Hendriks BHW. Variable-focus liquid lens for miniature cameras. *Appl Phys Lett*. 2004;85(7):1128-1130. doi:10.1063/1.1779954.
205. Park IS, Yang JW, Oh SH, Chung SK. Multifuctional liquid lens for high-performance miniature cameras. In: *Proceedings of the IEEE International Conference on Micro Electro Mechanical Systems (MEMS)*. Vol 2016-Febru. ; 2016:776-779. doi:10.1109/MEMSYS.2016.7421744.
206. Kim DY, Steckl AJ. Electrowetting on paper for electronic paper display. *ACS Appl Mater Interfaces*. 2010;2(11):3318-3323. doi:10.1021/am100757g.
207. You H, Steckl AJ. Three-color electrowetting display device for electronic paper. *Appl Phys Lett*. 2010;97(2). doi:10.1063/1.3464963.
208. Samiei E, Tabrizian M, Hoorfar M. A review of digital microfluidics as portable platforms for lab-on a-chip applications. *Lab Chip*. 2016;16:2376-2396. doi:10.1039/C6LC00387G.
209. Cho SK, Moon H, Kim CJ. Creating, transporting, cutting, and merging liquid droplets by electrowetting-based actuation for digital microfluidic circuits. *J Microelectromechanical Syst*. 2003;12(1):70-80. doi:10.1109/JMEMS.2002.807467.
210. Nicolas Verplanck †, Elisabeth Galopin †, Jean-Christophe Camart † and, Vincent Thomy* †, and YC, Rabah Boukherroub* ‡. Reversible Electrowetting on Superhydrophobic Silicon Nanowires. 2007. doi:10.1021/NL062606C.
211. Zhu L, Xu J, Xiu Y, Sun Y, Hess DW, Wong C-P. Electrowetting of Aligned Carbon Nanotube Films. doi:10.1021/jp063265u.
212. Krupenkin TN, Taylor JA, Schneider TM, Yang S. From rolling ball to complete wetting: the dynamic tuning of liquids on nanostructured surfaces. *Langmuir*. 2004;20(10):3824-3827.
213. Herbertson DL, Evans CR, Shirtcliffe NJ, McHale G, Newton MI. Electrowetting on superhydrophobic SU-8 patterned surfaces. *Sensors Actuators, A Phys*. 2006;130-131(SPEC. ISS.):189-193. doi:10.1016/j.sna.2005.12.018.
214. Wang Z, Ou Y, Lu TM, Koratkar N. Wetting and electrowetting properties of carbon nanotube templated parylene films. *J Phys Chem B*. 2007;111(17):4296-4299. doi:10.1021/jp071501a.

215. Campbell JL, Breedon M, Latham K, Kalantar-Zadeh K. Electrowetting of superhydrophobic ZnO nanorods. *Langmuir*. 2008;24(9):5091-5098. doi:10.1021/la7030413.
216. Han Z, Tay B, Tan C, Shakerzadeh M, Ostrikov K (Ken). Electrowetting Control of Cassie-to-Wenzel Transitions in Superhydrophobic Carbon Nanotube-Based Nanocomposites. *ACS Nano*. 2009;3(10):3031-3036. doi:10.1021/nn900846p.
217. Song K-Y, Morimoto K, Chen Y-C, Suzuki Y. Electrostatic instability of liquid droplets on MEMS-based pillared surfaces. *Sensors Actuators B Chem*. 2016;225:492-497. doi:10.1016/j.snb.2015.11.031.
218. Xu W, Choi CH. From sticky to slippery droplets: Dynamics of contact line depinning on superhydrophobic surfaces. *Phys Rev Lett*. 2012;109(2). doi:10.1103/PhysRevLett.109.024504.
219. Smith MT, Hawes AK, Bundy BC. Reengineering viruses and virus-like particles through chemical functionalization strategies. *Curr Opin Biotechnol*. 2013;24(4):620-626. doi:10.1016/j.copbio.2013.01.011.
220. Northrop BH, Frayne SH, Choudhary U, Michael A, Mather BD, Viswanathan K, Miller KM, Long TE, Nair DP, Podgórski M, Chatani S, Gong T, Xi W, Fenoli CR, Bowman CN, Miyadera T, Kosower EM, Ghosh SS, Koa PM, McCue AW, Chappelle HL, Brinkley M, Gindy ME, Ji S, Hoye TR, Panagiotopoulos AZ, Prud'homme RK, Yeh H-Y, Yates M V., Mulchandani A, Chen W, Radu LC, Yang J, Kopecek J, Li M, De P, Gondi SR, Sumerlin BS, Pounder RJ, Stanford MJ, Brooks P, Richards SP, Dove AP, Connal LA, Kinnane CR, Zelikin AN, Caruso F, Stanford MJ, Dove AP, Peng K, Tomatsu I, Korobko A V., Kros A, Stanford MJ, Pflughaupt RL, Dove AP, Billiet L, Gok O, Dove AP, Sanyal A, Nguyen L-TT, Prez FE Du, Pauloehrl T, Delaittre G, Bastmeyer M, Barner-Kowollik C, Zhu J, Waengler C, Lennox RB, Schirrmacher R, Phelps EA, Enemchukwu NO, Fiore VF, Sy JC, Murthy N, Sulchek TA, Barker TH, Garcia AJ, Koehler KC, Anseth KS, Bowman CN, Gobbo P, Biesinger MC, Workentin MS, Baldwin AD, Kiick KL, Klob HC, Finn MG, Sharpless KB, Mose J \nE., Moorhouse AD, Barker-Kowollik C, Prez FE Du, Espeel P, Hawker CJ, Junkers T, Schlaad H, Camp W Van, et al. Thiol–maleimide "click" chemistry: evaluating the influence of solvent, initiator, and thiol on the reaction mechanism, kinetics, and selectivity. *Polym Chem*. 2015;6(18):3415-3430. doi:10.1039/C5PY00168D.
221. Miller RA, Presley AD, Francis MB. Self-assembling light-harvesting systems from synthetically modified tobacco mosaic virus coat proteins. *J Am Chem Soc*. 2007;129(11):3104-3109. doi:10.1021/ja063887t.
222. Ma Y-Z, Miller R a, Fleming GR, Francis MB. Energy transfer dynamics in light-harvesting assemblies templated by the tobacco mosaic virus coat protein. *J Phys Chem B*. 2008;112:6887-6892. doi:10.1021/jp8006393.
223. Endo M, Fujitsuka M, Majima T. Porphyrin light-harvesting arrays constructed in the recombinant tobacco mosaic virus scaffold. *Chem - A Eur J*. 2007;13(31):8660-8666. doi:10.1002/chem.200700895.
224. Yi H, Nisar S, Lee SY, Powers MA, Bentley WE, Payne GF, Ghodssi R, Rubloff GW, Harris MT, Culver JN. Patterned assembly of genetically modified viral

nanotemplates via nucleic acid hybridization. *Nano Lett*. 2005;5(10):1931-1936. doi:10.1021/nl051254r.

225. Yin Z, Nguyen HG, Chowdhury S, Bentley P, Bruckman MA, Miermont A, Gildersleeve JC, Wang Q, Huang X. Tobacco mosaic virus as a new carrier for tumor associated carbohydrate antigens. *Bioconjug Chem*. 2012;23(8):1694-1703. doi:10.1021/bc300244a.
226. Banik S, Mansour AA, Suresh RV, Wykoff-Clary S, Malik M, McCormick AA, Bakshi CS. Development of a Multivalent Subunit Vaccine against Tularemia Using Tobacco Mosaic Virus (TMV) Based Delivery System. *PLoS One*. 2015;10(6):1-22. doi:10.1371/journal.pone.0130858.
227. Smith ML, Lindbo JA, Dillard-Telm S, Brosio PM, Lasnik AB, McCormick AA, Nguyen L V., Palmer KE. Modified Tobacco mosaic virus particles as scaffolds for display of protein antigens for vaccine applications. *Virology*. 2006;348(2):475-488. doi:10.1016/j.virol.2005.12.039.
228. Lee KL, Carpenter BL, Wen AM, Ghiladi RA, Steinmetz NF. High Aspect Ratio Nanotubes Formed by Tobacco Mosaic Virus for Delivery of Photodynamic Agents Targeting Melanoma. *ACS Biomater Sci Eng*. 2016;2(5):838-844. doi:10.1021/acsbiomaterials.6b00061.
229. Bruckman MA, Kaur G, Lee LA, Xie F, Sepulveda J, Breitenkamp R, Zhang X, Joralemon M, Russell TP, Emrick T, Wang Q. Surface Modification of Tobacco Mosaic Virus with "Click" Chemistry. *ChemBioChem*. 2008;9(4):519-523. doi:10.1002/cbic.200700559.
230. Tian Y, Gao S, Wu M, Liu X, Qiao J, Zhou Q, Jiang S, Niu Z. Tobacco Mosaic Virus-Based 1D Nanorod-Drug Carrier via the Integrin-Mediated Endocytosis Pathway. *ACS Appl Mater Interfaces*. 2016;8(17):10800-10807. doi:10.1021/acsami.6b02801.
231. Bruckman MA, Hern S, Jiang K, Flask CA, Yu X, Steinmetz NF. Tobacco mosaic virus rods and spheres as supramolecular high-relaxivity MRI contrast agents. *J Mater Chem B Mater Biol Med*. 2013;1(10):1482-1490. doi:10.1039/C3TB00461A.
232. Sayam Sen Gupta †, Jane Kuzelka †, Pratik Singh ‡, Warren G. Lewis †, Marianne Manchester ‡ and, M. G. Finn* †. Accelerated Bioorthogonal Conjugation: A Practical Method for the Ligation of Diverse Functional Molecules to a Polyvalent Virus Scaffold. 2005. doi:10.1021/BC050147L.
233. Guiseppi-Elie A, Lei C, Baughman RH. Direct electron transfer of glucose oxidase on carbon nanotubes. *Nanotechnology*. 2002;13(5):559-564. doi:10.1088/0957-4484/13/5/303.
234. Elgrishi N, Rountree KJ, McCarthy BD, Rountree ES, Eisenhart TT, Dempsey JL. A Practical Beginner's Guide to Cyclic Voltammetry. *J Chem Educ*. 2018;95(2):197-206. doi:10.1021/acs.jchemed.7b00361.
235. Tlili A, Abdelghani A, Hleli S, Maaref M. Electrical Characterization of a Thiol SAM on Gold as a First Step for the Fabrication of Immunosensors based on a Quartz Crystal Microbalance. *Sensors*. 2004;4(6):105-114. doi:10.3390/s40670105.

236. Page CC, Moser CC, Chen X, Dutton PL. Natural engineering principles of electron tunnelling in biological oxidation–reduction. *Nature*. 1999;402(6757):47-52. doi:10.1038/46972.
237. Wu J, Yang H. Platinum-Based Oxygen Reduction Electrocatalysts. *Acc Chem Res*. 2013;46(8):1848-1857. doi:10.1021/ar300359w.
238. Yan Y, Zheng W, Su L, Mao L. Carbon-Nanotube-Based Glucose/O2 Biofuel Cells. *Adv Mater*. 2006;18(19):2639-2643. doi:10.1002/adma.200600028.